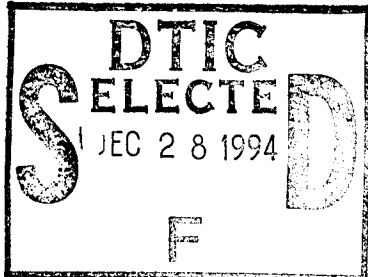


**DEFORMATION BEHAVIOR OF THIN LUBRICANT FILMS  
AT ELEVATED PRESSURE**



**December 1994**

**A Report to the**

**Office of Naval Research  
800 North Quincy Street  
Arlington, VA 22217-5000**

**by**

**Scott Bair  
Principal Research Engineer**

**F. Qureshi  
Graduate Research Assistant**

**Y. K. Lee  
Assistant Professor**

**W. O. Winer  
Regent's Professor and Direct**

**George W. Woodruff School of Mechanical Engineering  
Georgia Institute of Technology**

**19941223 002**

This document has been approved  
for public release and sale; its  
distribution is unlimited.



# CONTENTS

	<u>Page</u>
SUMMARY .....	3
1. BACKGROUND .....	6
2. VISCOSITY .....	10
3. ELASTIC SHEAR MODULUS .....	16
4. COMPRESSIBILITY .....	18
5. NON-NEWTONIAN RESPONSE .....	25
5.1 Viscous Heating in Couette Viscometry .....	26
5.2 Some Results for Pressures to 300 MPa .....	30
5.3 A New High-Stress Couette Viscometer for 600 MPa Pressure .....	33
5.4 Results for Pressures to 600 MPa .....	36
6. EHD TRACTION CALCULATION .....	42
7. NEW OBSERVATIONS OF MECHANICAL SHEAR BANDS IN SIMPLE PLANE SHEAR .....	44
7.1 Birefringence .....	47
7.2 Persistence of Shear Bands .....	49
7.3 Dilatation .....	51
7.4 Surface Roughness Effect .....	52
8. SLIP CRITERION .....	52
8.1 Analogy to Glassy Polymers .....	52
8.2 Mohr-Coulomb Criterion .....	53
9. RHEOLOGICAL MODELS .....	57
10. MECHANICAL SHEAR BANDS IN NON-VISCOMETRIC FLOW .....	59
10.1 Shear Band Observations in Wedge Flow .....	59
10.2 Extra High-Pressure Flow Visualization Cell .....	61
10.3 Shear Band Observations in Squeeze Film .....	61
11. ADIABATIC SHEAR BANDS .....	63
11.1 Background .....	63
11.2 Experiment .....	66
11.3 Thermal Analysis .....	71
11.4 Optical Ray Tracing .....	72
11.5 Discussion .....	
12. OBSERVATIONS IN AN OPERATING EHD CONTACT .....	75

## SUMMARY

### Research Goals

The elastohydrodynamic (EHD) regime of lubrication is responsible for the generation of a protective film and the transfer of shear across concentrated contacts in many machine elements including bearings, cams and gears. It is now understood that small scale EHD plays a major role in the boundary lubrication of rough surfaces. Many high-pressure metal working operations share the pressure and kinematics of elastohydrodynamics. A complete solution of the EHD problem, however, requires a thorough knowledge of the lubricant constitutive behavior and the attending properties as functions of temperature and pressure. The Newtonian assumption alone is inadequate.

It has been observed in boundary lubrication and in some aspects of elastohydrodynamic lubrication that friction is nearly Coulombic in nature - the friction coefficient is only weakly dependent upon load and sliding velocity. In some instances the friction coefficient may be so similar in the boundary and EHD regimes that friction alone does not clearly discriminate the transition from one to the other. These attributes of liquid lubrication would seem enigmatic.

It has been the goal of this program to elucidate the deformation mechanisms responsible for the unexpected behavior of liquid lubricants under the uniquely severe conditions of EHD and provide numerical analysts and designers with a rheological model for prediction.

### Significant Results

Work supported by ONR and performed in this laboratory has resulted in major advances in understanding the deformation mechanisms of lubricants at high pressure. Among these are:

- 1) Rate independent and perhaps even non-linear shear rheological response for liquids at high-pressure and high-stress is the result of intermittent slip along inclined planes which

are consistent with the Mohr-Coulomb theory if a first normal stress difference is assumed.

- 2) Slip within the lubricant film is associated with dilatation which results in the pressure dependence of the shear strength of these films.
- 3) Deformation within a lubricant film may localize by a thermal mechanism as well, if the Brinkman number is sufficiently large and the flow is stress-controlled.
- 4) The pressure capability of high-pressure high-stress rheometers has been improved so that accurate calculations of concentrated contact traction can be obtained from primary material property measurements.

#### **Plans for Next Year**

We have introduced the Mohr-Coulomb failure criterion as a method for predicting slip. Mohr-Coulomb defines two possible orientations for stress induced shear bands. Both are experimentally observed in our high-pressure flow visualization cell and the measure of the included angle between the types of bands is consistent with theory. A first normal stress difference must be introduced to account for the orientation of the shear bands with respect to the principal shear directions.

The first normal stress difference in uniaxial shear was the subject of conjecture and controversy early in the study of high-pressure rheology of lubricants; however there has been no attempt to measure this effect under high-pressure. An existing high-pressure rheometer will be modified so that the normal stress may be measured. Shear stress and the normal stress difference will be reported as functions of the shear rate (i.e., the viscometric functions).

The pressure capability of our flow-visualization system has been increased to 1 GPa in a squeeze film configuration. We will extend this new pressure capability to the unaxial shear configuration for which the interpretation of results is unambiguous. We can then seek a correlation between the nucleation of shear bands and the viscometric functions.

The viscometric functions for shear and normal stress differences will be incorporated into a model for shear band prediction. The consequences of a successful program are far-reaching. The friction coefficient in concentrated contact has been treated as a disposable parameter in numerical and analytical studies. We will show that the friction coefficient is instead related to material properties of the lubricant.

## 1. BACKGROUND

The elastohydrodynamic (EHD) regime of lubrication is responsible for the generation of a protective film and the transfer of shear across concentrated contacts in many machine elements. It is now understood that small scale EHD plays a major role in the boundary lubrication of rough surfaces. Many high-pressure metal working operations share the pressure and kinematics of elastohydrodynamics. A complete solution of the EHD problem, however, requires a thorough knowledge of the lubricant constitutive behavior and the attending properties as functions of temperature and pressure. The Newtonian assumption alone is inadequate.

Early investigations of high-pressure lubricant rheology addressed the small strain response. For small strains, viscous heating which plagues large strain measurements may be ignored. These measurements were both optical and acoustical, e.g. references [1] and [2] respectively, and provided linear viscoelastic properties. These techniques are experimentally convenient in requiring only optical or electrical paths through the high-pressure chamber. The linear viscoelastic response is, however, unable to account for any but the small slip traction in EHD.

Attention then turned to large strain investigations which could reveal non-linear behavior and successfully predict EHD traction [3]. The progress in this area has recently been significant in that the mechanism of non-linearity (at least for low molecular weight liquids) has been shown to be a mechanically induced shear localization or shear bands [4]. The constitutive behavior which in a rheological measurement by definition excludes the shear bands is apparently linear viscoelastic. Attention must then eventually return to the small strain linear viscoelastic behavior. For it is the constitutive response which provides the stress field which initiates the localization.

That is to say, one must understand the constitutive response of the homogeneously deforming matrix to predict the onset and orientation of shear bands.

Fundamental to the generation of a film in concentrated contact is the piezoviscous property of liquid lubricants - whereby even simple low molecular weight liquids at ambient temperature attain very great viscosities under pressure. Shear rheological investigations of non-Newtonian response of lubricants [5,6] have resorted to low temperatures to achieve the same level of viscosity. It is clear now, that high-pressure is essential to an accurate simulation. Liquids become considerably "stronger" under pressure. Peculiar to these atmospheric pressure studies was the observation of fracture. Eastwood and Harrison [5] could observe the liquid in shear and reported cracking.

Early investigations of non-Newtonian lubricant flow often studied polymer solutions. The blend of mineral base oil and polymeric viscosity index improver is representative of multi-grade motor oils. The capillary rheometer was useful for this purpose as it is very simply pressurized and although the shear stress cannot be large for this instrument, non-Newtonian flow occurs at relatively low stress for polymer solutions. The high-pressure capillary viscometer was developed to a high level by Jakobsen and Winer [7] who reported measurements to shear rates of  $10^7 \text{s}^{-1}$ , pressures to 600 MPa and time of shear as short as 4  $\mu\text{s}$ . They reported Newtonian flow for liquid lubricant base stocks to a shear stress of 5 MPa.

A flow chart for a mineral oil / PAMA blend is reproduced from [8] in Figure 1 for pressures and temperatures indicated. The logarithm of effective viscosity,  $\mu_e = \tau / \dot{\gamma}$ , is plotted against the logarithm of shear stress,  $\tau$ . The diagonal lines represent rate of shear,  $\dot{\gamma}$ . The typical transition from the first to the second Newtonian regimes are evident. The liquid flows with constant effective viscosity provided that the stress is below or above the transition region. The

presentation in Figure 1 is particularly effective in that the non-Newtonian transition is shown to be defined by a more-or-less constant critical stress rather than a critical rate. That is, individual flow curves may be superimposed by shifting along a linear path which to an approximation is a constant shear stress path. This observation (which has not always been well recognized in the Tribology community) is a statement of time-temperature (-pressure) superposition. Following reference [9], to obtain the effective viscosity at a temperature,  $T$ , from the flow curve measured at a reference temperature,  $T_R$ , set

$$\mu_e(T, \dot{\gamma}) = \frac{\mu(T)}{\mu(T_R)} \mu_e(T_R, a_T \dot{\gamma}) \quad (1)$$

where  $\mu$  is the limiting low shear viscosity and  $a_T$  is the shift factor. A good approximation for  $a_T$  is [9,10]

$$a_T = \frac{\mu(T)}{\mu(T_R)} \quad (2)$$

The superposition technique was extended to include pressure by Phillippoff [11].

Equations (1) and (2) yield the result

$$\beta_e = m \beta \quad (3)$$

where  $\beta$  is the temperature-viscosity coefficient,  $\partial \ln \mu / \partial T$ , and  $m$  is the rate sensitivity coefficient,  $\partial \ln \tau / \partial \ln \dot{\gamma}$ , and  $\beta_e$  is the effective temperature-viscosity coefficient for a rate-controlled process with non-Newtonian response. Equation (3) was also found experimentally by Winter [12] and is very useful in assessing viscous heating effects for high dissipation rheometry. It should be clear

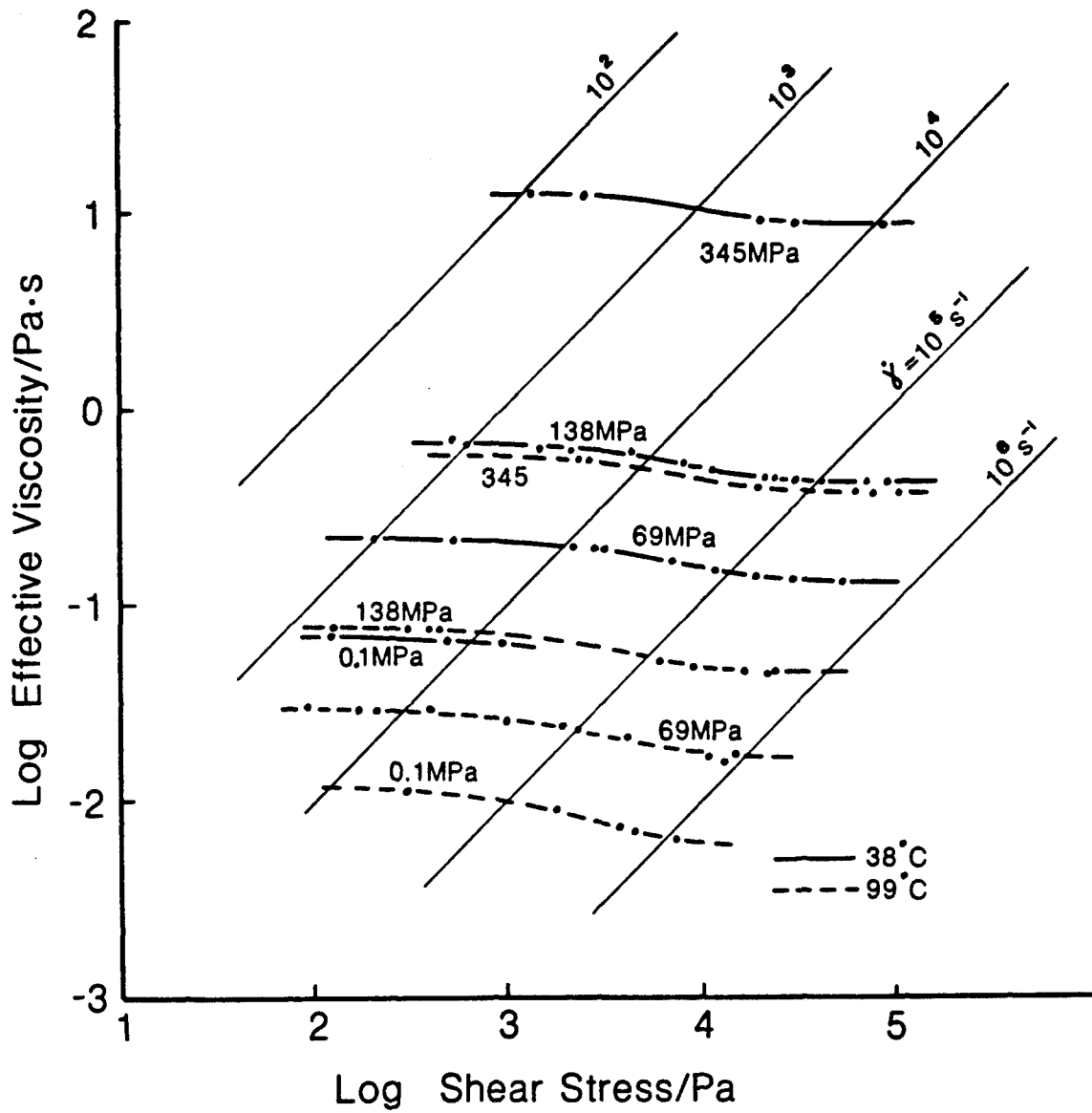


Figure 1. Flow Chart for Blend of Paraffinic Mineral Oil + 4% Polyalkylmethacrylate from [8].

from Figure 1 and the above that a rheological experiment to obtain constitutive information for lubricants must simulate the shear stress of the lubrication problem rather than the rate when the dissipation is limited by experimental technique. In addition, an accurate correlation of the limiting low shear viscosity,  $\mu$ , with temperature and pressure is indispensable to an investigation of constitutive behavior of liquids under pressure.

## 2. VISCOSITY

The measurement of limiting low shear viscosity (hereafter, simply viscosity) under pressure has become relatively routine. Some commercial viscometers can reach 300 MPa. Laboratory high-pressure viscometers can operate to 1 GPa and above and are most often of the falling body type which is described in [13]. Falling body viscometers apply a shear stress typically less than 100 Pa so that the liquid response should be Newtonian; although the rate of shear may exceed  $10^4 \text{s}^{-1}$  for low viscosity. Because of the low applied shear stress, the sinker fall times become inconveniently large for viscosity greater than  $10^4 \text{ Pa}\cdot\text{s}$ .

A new variation of the falling body viscometer was developed in this laboratory and was utilized to generate some of the results for viscosity greater than  $10^3 \text{ Pa}\cdot\text{s}$  in Figure 2. The sinker would conventionally be made to fall under the force of gravity toward the bottom of a pressure chamber. The time of fall yields viscosity. If one places a spring between the sinker and the closed bottom end of the pressure chamber, any increase in pressure which reduces the specific volume of the liquid, will push the sinker toward the closed end of the chamber, thereby compressing the spring. The spring will eventually return the sinker to its equilibrium rest position while displacing liquid through the clearance (typically 100  $\mu\text{m}$ ) between the sinker and the chamber. The system relaxes to equilibrium with exponentially decaying motion as a spring-

the chamber. The system relaxes to equilibrium with exponentially decaying motion as a spring-dashpot. The time constant for this motion will yield a measure of viscosity if the initial sinker position is defined at a sufficiently late time so that the heat of compression has been conducted from the liquid into the chamber walls.

The maximum viscosity which can be measured by the falling body technique is limited by the stability of position sensing instruments over long fall times. The spring-dashpot technique increases the maximum obtainable viscosity for a given observation time by increasing the applied shear stress to about 600 Pa. An additional benefit of the increased stress is that weak wax structures (which sometimes form in mineral oil at high pressures and arrest the fall of a sinker) are broken.

The viscosity under pressure for two perfluorinated polyethers is shown graphically in Figure 2. The 143AD and 143AC differ only in molecular weight - the former being higher in molecular weight. The slope of an isotherm is related to the local pressure viscosity coefficient,  $\alpha = \partial \ln \mu / \partial p$ . Clearly the slope and  $\alpha$  decrease with pressure initially. Then at some inflection they begin to increase with pressure. Bridgman [14] suggested that for pressure greater than 1.2 GPa,  $\alpha$  increases with pressure for all liquids. This was supported by measurements to 6 GPa on some organic liquids by Barnett and Basco [15], and more recently at lower pressures [16].

Several useful pressure-viscosity correlations are available for low pressures characteristic of the EHD inlet zone. These generally treat the pressure-viscosity coefficient as monotonically decreasing with pressure and for most liquid lubricants are suitable to 0.3 GPa provided the viscosity does not exceed about  $10^2$  Pa·s. The use of these correlations for extrapolation to EHD Hertzian zone pressures can, however, yield misleading trends. For example, Hsiao, et al [17] fitted the parameters of the isothermal Roelands equation to the viscosity of 143AC up to 0.3

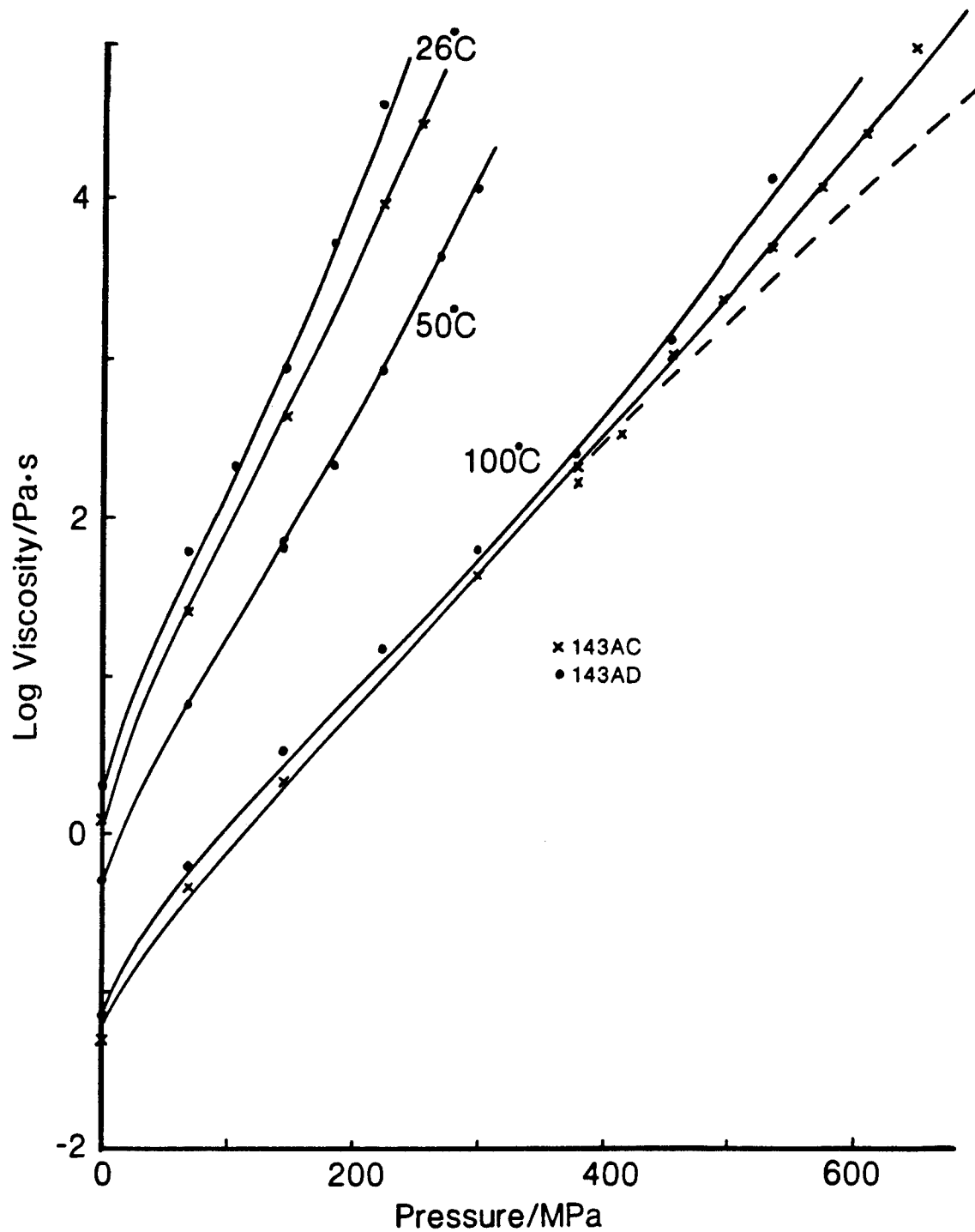


**Figure 2.** Pressure-Viscosity plot for two perfluorinated polyalkylethers. Solid curves are Free Volume Model [18]. Broken curve is extrapolation from [17]. Points are Measured Viscosities.

GPa and used this correlation to extrapolate to 1.0 GPa pressure. The broken curve in Figure 2 is their result. Clearly, at only 0.6 GPa the measured viscosity diverges from the extrapolation. Although this deficiency has been known for some time and was acknowledged by Roelands [3], the Roelands equation continues in use for numerical simulation of the lubricant in the Hertzian zone.

The viscosity of the mineral oil, HVI 650, was obtained using a falling body viscometer and a Couette viscometer which will be described later. The curves in Figure 3 and the solid curves in Figure 2 represent the Free Volume Model of Yasutomi [18]. The glass transition is taken to be an isoviscous state with viscosity of  $\mu_g$  and with the glass transition temperature related to pressure as

$$T_g = T_{g0} + A_1 \ln(1 + A_2 p) \quad (4)$$

The relative free volume expansivity is also taken to be pressure dependent as

$$F = 1 - B_1 \ln(1 + B_2 p) \quad (5)$$

The viscosity can be calculated from the WLF equation.

$$\mu = \mu_g \exp \left[ \frac{-2.3 C_1 (T - T_g) F}{C_2 + (T - T_g) F} \right] \quad (6)$$

The parameters for equations (4-6) were regressed from viscosity data and are tabulated for some of the lubricants used in this paper in Table 1 where a value of  $\mu_g$  was assumed. Use of this model provides some contact between the piezoviscous effect and state properties.

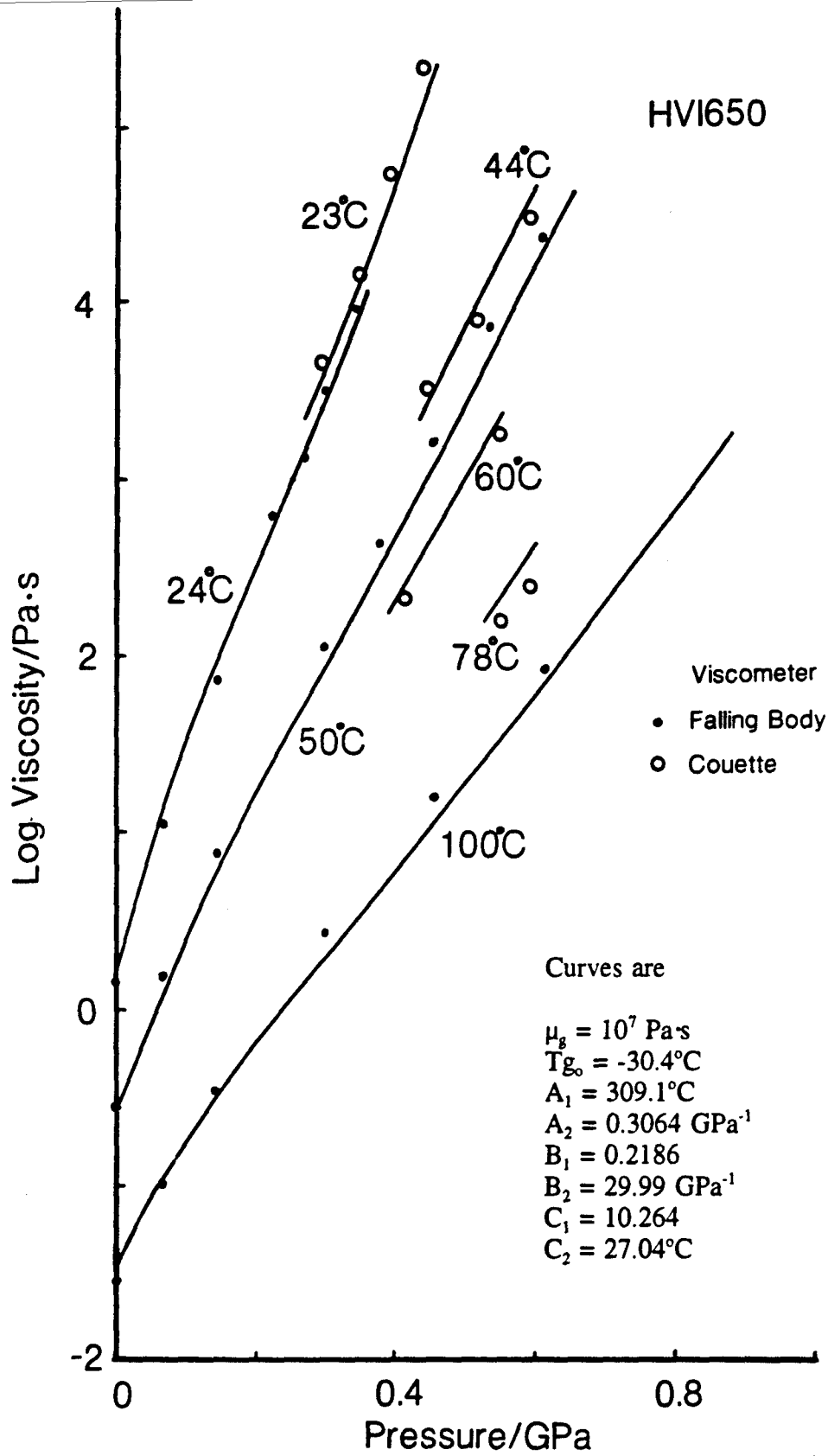


Figure 3. Pressure-Viscosity plot for HVI 650. Curves are for Free Volume Model.

**Table 1.**  
**Free Volume Parameters**

<u>Liquid</u>	<u><math>\mu_p</math>/Pa·s</u>	<u><math>T_g</math>/°C</u>	<u><math>A_1</math>/°C</u>	<u><math>A_2</math>/GPa<sup>-1</sup></u>	<u><math>B_1</math></u>	<u><math>B_2</math>/GPa<sup>-1</sup></u>	<u><math>C_1</math></u>	<u><math>C_2</math>/°C</u>
143AC	10 <sup>7</sup>	-64.93	185.8	1.628	0.1806	37.55	10.802	50.69
143AD	10 <sup>7</sup>	-60.91	183.8	1.805	0.1277	75.42	10.592	49.44
HVI650	10 <sup>7</sup>	-30.4	309.1	0.3064	0.2186	29.99	10.264	27.04
Santotrac 40	10 <sup>7</sup>	-79.62	91.86	3.805	0.3865	5.138	12.381	52.14
SHF1001	10 <sup>7</sup>	-58.2	325.6	0.2948	0.1536	30.79	11.120	57.88

**Table 2.**  
**Comparison of Relative Thermal Expansivity,**  
 **$\epsilon(p)/\epsilon(o)$ , with that Calculated from**  
**Free Volume Model for 143AC**

<u>Pressure/MPa</u>	<u>from [19]</u> <u><math>\epsilon(p)</math>/°C<sup>-1</sup></u>	<u><math>\epsilon(p)/\epsilon(o)</math></u>	<u><math>F/(2-F)^*</math></u>
0	9.7 x 10 <sup>-4</sup>	1.00	1.00
34.5	6.9	0.72	0.74
69	5.7	0.59	0.62
103.5	5.0	0.52	0.55
138	4.5	0.46	0.50
172	4.14	0.43	0.47

\*F from eqn (5)

Recent numerical simulations of thermal compressible EHD have incorporated state equations which treat the thermal expansivity,  $\epsilon$ , as a constant with a value equal to the atmospheric pressure value. This must be suspect as it can be seen that the thermal expansivity decreases to about one-third of the atmospheric value at 1 GPa for most liquid lubricants. Yasutomi [18] showed that the relationship

$$\frac{\epsilon(p)}{\epsilon(0)} = \frac{F(p)}{2 - F(p)} \quad (7)$$

holds for liquids of various chemical composition to a pressure of at least 0.6 GPa. Wilson [19] measured the density as a function of temperature and pressure for 143AC using a bellows type of piezometer. The thermal expansivities were calculated from both [19] and equation (7) and are compared in Table 2. The agreement should be considered good in light of the difference in experimental technique.

### 3. ELASTIC SHEAR MODULUS

A description of the transient small strain response of liquid lubricants at high-pressure requires as a material property the limiting high-frequency elastic shear modulus (hereafter simply shear modulus). It was shown (Ref [3]) that a Maxwell element adequately represented the transient uniaxial shear stress-strain response in a rheometer for a mineral oil at a pressure of 780 MPa. For small strains, only the viscosity and shear modulus,  $G$ , are required.

There have been few recent experimental measurements of the shear modulus of liquid lubricants under pressure. There does exist, however, a body of literature which shows consistent results for the variation of  $G$  with pressure near room temperature. These data are collected in Figure 4 where the results of three different techniques - light scattering, acoustic, and direct

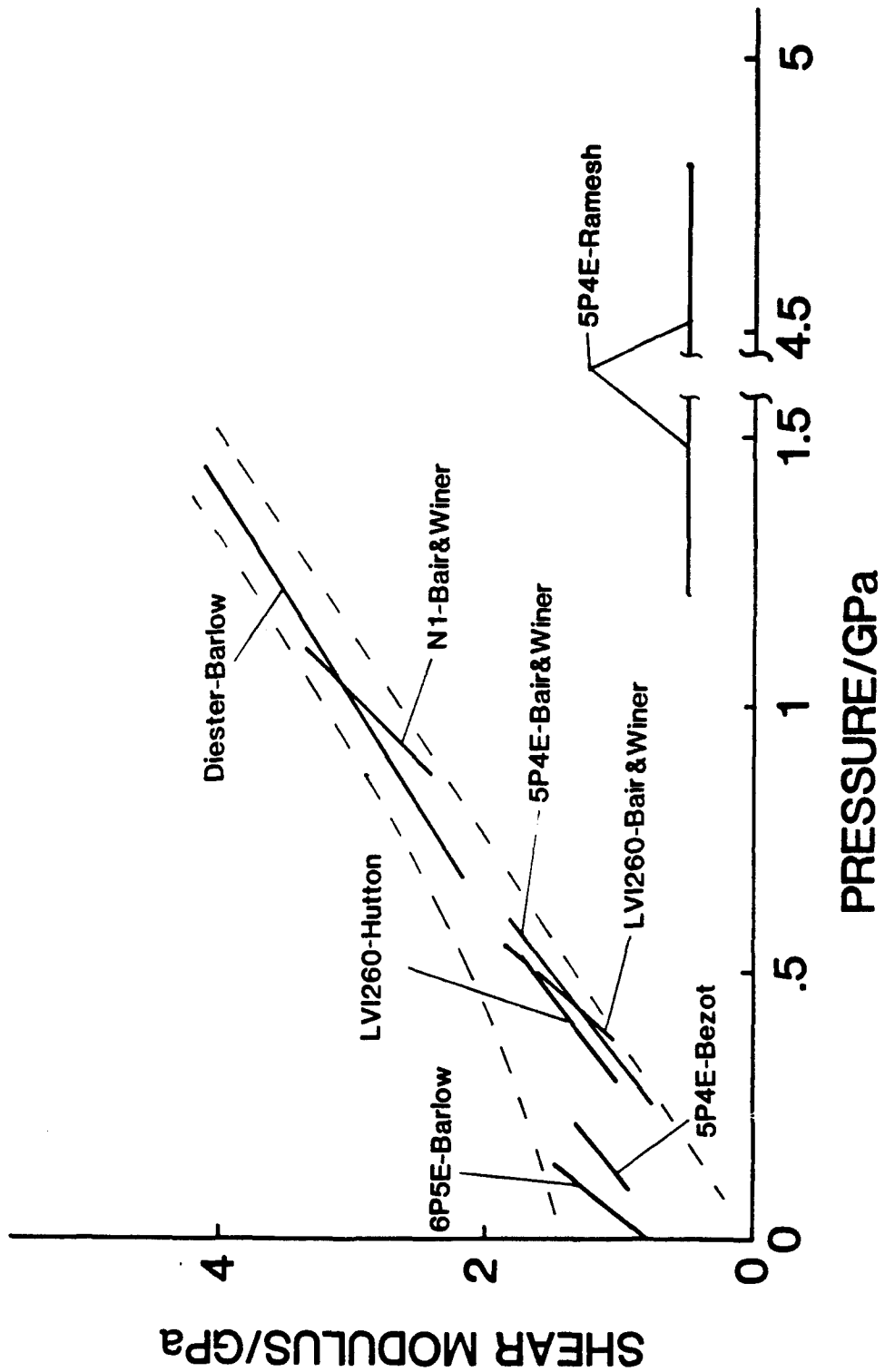


Figure 4. The Elastic Shear Modulus of Liquid Lubricants at Room Temperature by: light scattering by Bezot [20], acoustics by Barlow [2] and Hutton [21], mechanical by Bair and Winer [3], impact by Ramesh [22].

mechanical measurement - fit nicely within the envelope shown by the broken curves. References are given in the figure. For high pressures it would appear that we can approximate  $G \approx 3p$ . Only the pressure-shear plate impact measurements are inconsistent. In the impact work, thermal softening was neglected and the observed non-linear shear response was attributed to constitutive behavior in the form of the Eyring model. However, the authors estimate the temperature rise due to shear heating to be as high as 78°C [22]. In as much as the liquid (5P4E) studied is one of the most temperature-sensitive known, it is more likely that the non-linearity can be attributed to shear heating.

#### 4. COMPRESSIBILITY

Lubricant compressibility is a second order effect for the film thickness in concentrated contact. However, dilatation apparently plays a key role in the initiation of mechanical shear bands [23] which limit the shear strength of liquid films as evidenced by the pressure dependence of the shear strength [24]. Numerical simulations of EHD usually incorporate a liquid equation of state which assumes a maximum limiting density. This concept is not supported by experimental results.

The compressibility of liquids is usually determined by one of two techniques. The displacement of a piston under a known force yields a volume change if the deformation of a piston/cylinder device can be accurately accounted for. Alternatively, a piezometer may be immersed in a fluid medium for which the pressure is controlled. Here, the piezometer signal must be passed through the vessel which confines the fluid medium.

A unique instrument was designed and constructed in this laboratory and is pictured in cut-away view in Figure 5. The Differential Scanning Dilatometer (DSD) is essentially two

piston/cylinder devices placed in series so that the piston forces are identical. If the cylinder bores and seals are identical, the pressures in the cylinders are equal. Each cylinder communicates with a separate compression chamber in a temperature controlled block through small bore tubing and fittings. Temperature of the block is measured by a thermocouple centered between the chambers and the temperature is controlled by passing either liquid N<sub>2</sub> boil off or heated air through a series of holes (not shown in Figure 5) in the block. The intensifier vessel, tubing and compression chamber are filled with a liquid high pressure medium. The high pressure medium is the diester, bis (2-ethyl hexyl) sebecate, which is widely used for high pressure work. Each chamber accepts a thin plastic capsule - one capsule containing a tungsten slug (in the reference chamber) and one capsule containing an equal volume of the liquid sample (in the sample chamber).

Two potentiometers are utilized as piston displacement transducers. (They cannot be seen in the Figure.) The transducer outputs are electrically subtracted so that the signal represents  $x_R - x_S$ . Now, as the system pressure is varied, the relative piston displacement  $x_S - x_R$  is a measure of the dilatation of the sample relative to that of tungsten. The deformation of the vessel and structure is removed from the measurement to the extent that these deformations affect both piston displacements equally. Tungsten was chosen as a reference material for its very large bulk modulus and low thermal expansivity.

Here we are concerned with the isothermal compressibility. Indeed, it would probably not be possible to make measurements with sufficient speed to approach the adiabatic idealization. To ensure that the compression of the sample can be regarded as isothermal, a transient heat

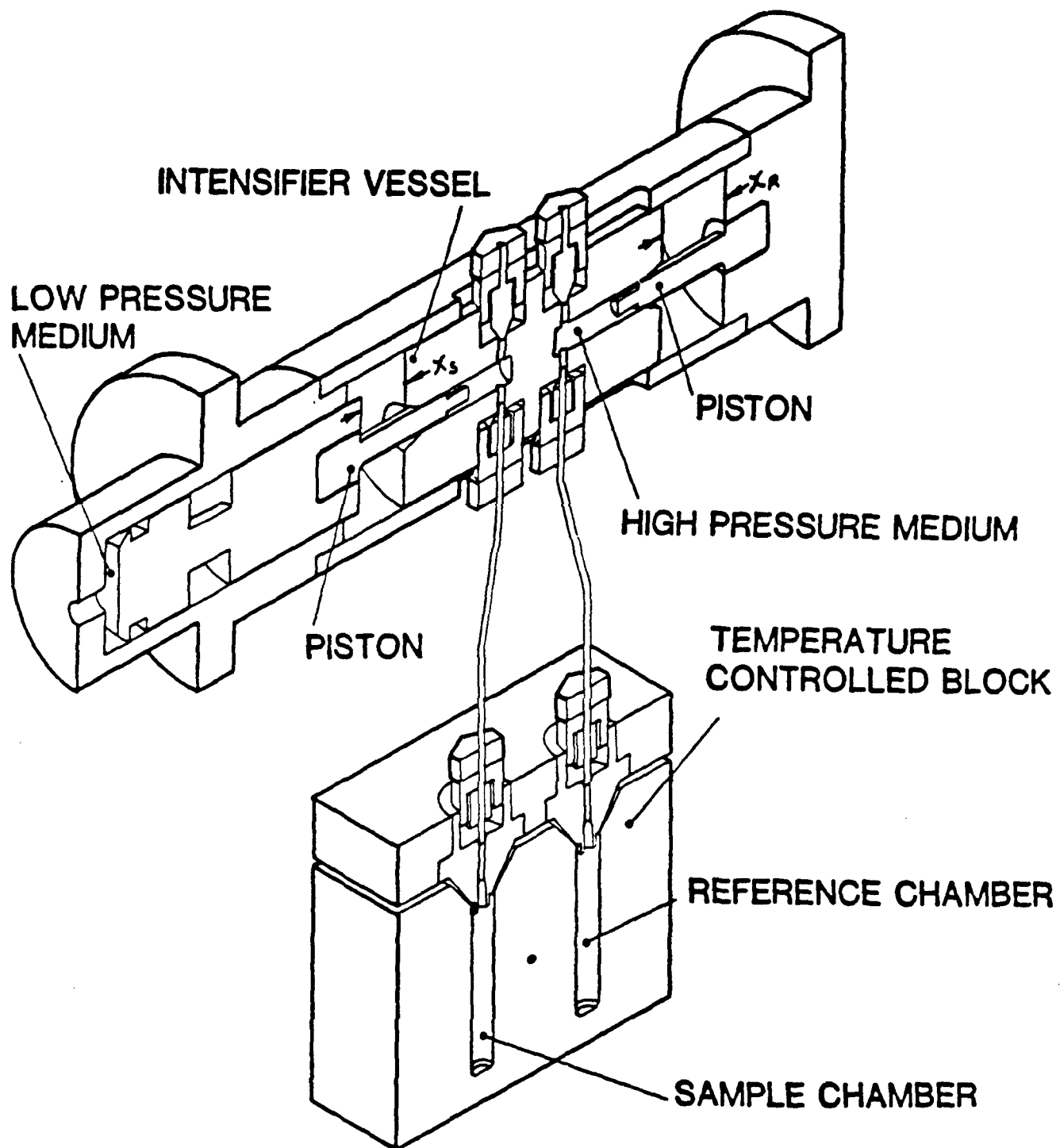


Figure 5. Differential Scanning Dilatometer in Cross-Section.

transfer numerical analysis was performed to identify the maximum pressurizing rate (which is 140 MPa/minute) for which the heat of compression can be effectively removed by conduction. Experimentally, one could simply remain at elevated pressure for a very long time; however to do so increases the risk of leaks becoming significant.

The instrument described above provides a refined technique for observing liquid compressibility in a pressure range which brackets the glass transition pressure,  $p_g$ , while maintaining a nearly hydrostatic state of stress. For example, with a piston/cylinder type of dilatometer, in addition to reducing the volume of the sample, one is also performing a uniaxial compression of the cylindrical sample and therefore introducing deviatoric stress. Also, shear stresses are introduced in the interface between the liquid and the cylinder bore. Given sufficient time, the liquid will relax to a purely hydrostatic condition; however, if the pressure is sufficiently greater than  $p_g$  the relaxation time will be inconveniently long. The material response using previous techniques should be overly stiff for pressure greater than  $p_g$ . The present device compresses the liquid sample within an easily deformed capsule which is in turn surrounded by a low-viscosity liquid.

The accuracy of the present device was tested by measuring the relative density,  $\rho(p,T)/\rho(o,T)$ , of water and the results are compared with others from the literature in Table 3. The agreement is excellent. New results for the traction fluid, Santotrac 40, are presented in Table 4. The relative density of 5P4E (long the subject of high-pressure studies) versus pressure is graphically depicted in Figure 6. The glass-transition is evident as the "knee" in the curve and agrees quite well with the empirical formula for  $T_g(p)$  given by Yasutomi [18]. However, the bulk modulus of the glass is here considerably lower than that measured in a piston cylinder

device. The bulk modulus of glassy 5P4E is in Figure 6 about 7 to 8 GPa versus more than 20 GPa for piston/cylinder techniques.

Hamrock, et al [27] utilized a piston/cylinder type of dilatometer to report the change of density and glass transition pressure of liquid lubricants to 2.2 GPa. Ramesh [28] utilized a compression Kolsky bar and plate impact device to find the compressibility of 5P4E at compression times of 1 to 100  $\mu$ s. Although not clear from the latter paper, the significance of a short compression time is that the process approaches the adiabatic idealization. Therefore, the short-time compressibility must be less than that obtained from long-time, isothermal measurements even neglecting structural relaxation.

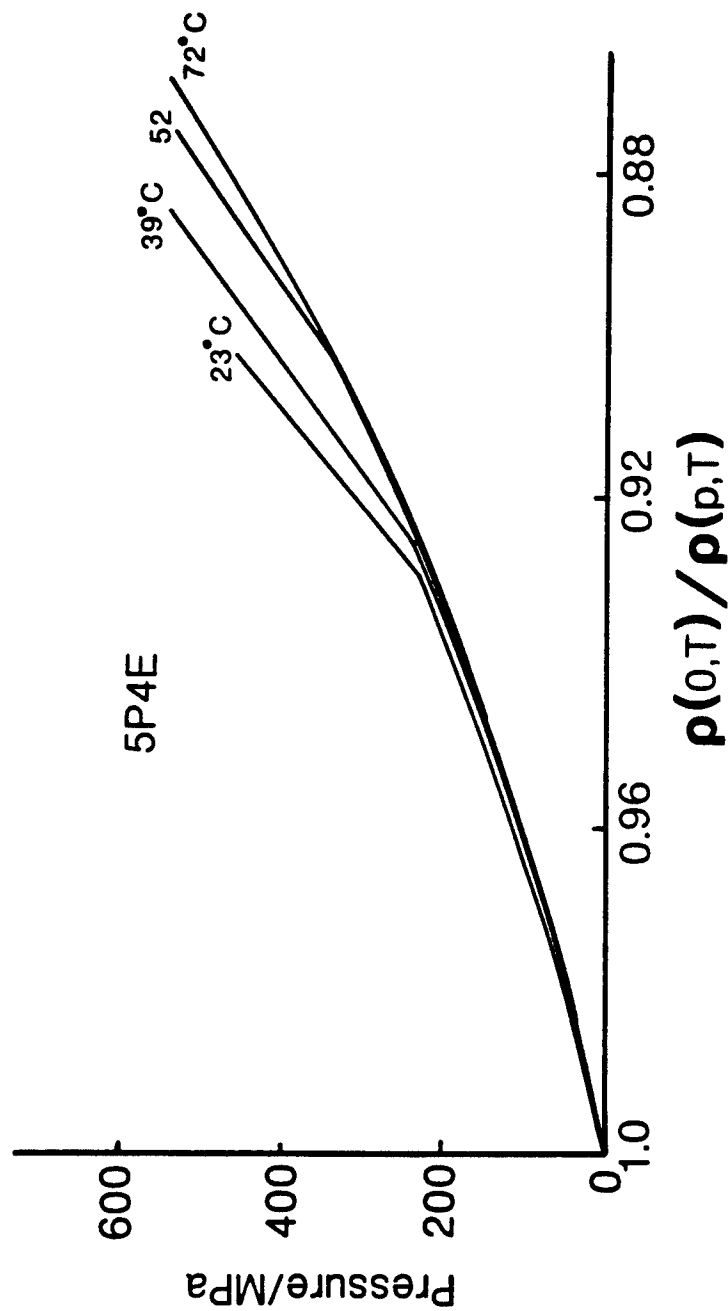


Figure 6. Relative Density of a Polyphenyl Ether versus Pressure Showing Glass Transition.

**Table 3.**  
**Relative Density of Water by Dilatometry**

$$\frac{\rho(p, T)}{\rho(o, T)}$$

Pressure MPa	0°C		50°C			95°C		
	DSD	[25]	DSD	[26]	[25]	DSD	[26]	[25]
0	1.000	1.000	1.000	1.000	1.000	1.000	1.000	1.000
98	1.046	1.045	1.040	1.038	1.039	1.040		1.041
196	1.080	1.081	1.072		1.072	1.076		1.076
294	1.111	1.112	1.099		1.100	1.104		1.105
392	1.136	1.137	1.121		1.125	1.126		1.131
490	1.156	1.159	1.142	1.143	1.147	1.153	1.152	1.154

**Table 4.**  
**Relative Density of Santotrac 40**

$$\frac{\rho(p, T)}{\rho(o, T)}$$

<u>Pressure</u> MPa	<u>-15°C</u>	<u>25°C</u>	<u>65°C</u>
0	1.000	1.000	1.000
100	1.035	1.043	1.042
200	1.060	1.074	1.075
300	1.079	1.097	1.100
400	1.095	1.113	1.120
500	1.108	1.132	1.137
600	1.121	1.151	1.157

## 5. NON-NEWTONIAN RESPONSE

The search for the relevant constitutive equations which relate the lubricant stress to the flow kinematics in concentrated contact has occupied the interest of tribologists working in EHD for at least thirty years. The goal has been to construct experiments to verify the rheological models and to provide the necessary property relations so that the complete elastohydrodynamic solution may be obtained. Various non-Newtonian models (see [3] for a review) have been advanced which provide accurate solutions for the traction over some operating range when the required rheological properties are obtained from the same traction data. In 1972, Dyson [29] warned that EHD traction research was "enclosed within a tight circle" of fitting parameters to observations without consideration for measurements made outside of EHD. Hopefully, we have broken from the circle.

We may now generate rheological flow curves under conditions of pressure, temperature, and rate of shear which, although still rather restricted, are sufficiently within the realm of EHD to make accurate traction predictions. We have previously interpreted these flow curves as lubricant constitutive behavior. However, in light of the recent observation [4] of mechanical shear bands operating within the lubricant film concurrent with non-linear shear response, this interpretation must be accompanied by a caveat: Rheological flow curves which are generated in plane shear yield an empirical rate equation which is useful in modeling Couette dominated lubrication problems. A rigorous analysis of the EHD problem would require a constitutive equation and a slip criterion such as Mohr-Coulomb [23].

## 5.1 Viscous Heating in Couette Viscometry

Presently, the most useful rheometer configuration for investigation of high-pressure, high-stress response of the liquid state is that of rotating concentric cylinders. When a liquid is sheared, the viscous work done raises the temperature of the liquid. While the study of this phenomenon is of itself interesting to lubrication, it is to be avoided in a rheological measurement because constitutive behavior excludes processes which result from temperature variation. In previous work [30] concerning Couette devices the authors have emphasized the importance of a low Brinkman No. (through primarily a small shearing gap) to mitigate the effect of the temperature difference within the liquid film and fast instrument response to control the temperature of the surfaces of the solid boundaries to the film. An alternate experimental approach is to perform a measurement in so short a time that the temperature profile in the film has not had time to develop but at a late enough time that the velocity profile is fully formed. Winter [31] showed that this latter approach requires that the Prandtl No. be large.

An earlier analysis of the combined effect of instrument response time and cylinder heating [30] modeled the cylinders as a lumped heat capacity. It was found that to minimize errors due to this combination the measured stress history should show no thermal softening over a period of time equal to the instrument response time. Later, the evolution of the radial temperature profile within the cylinders was considered [32]. A detailed example of a numerical thermal simulation of one of the high-pressure Couette viscometers used in this laboratory follows.

Only conduction in the radial direction is considered. An appropriate form of the energy equation for the metal cylinders is

$$\frac{\partial^2 T}{\partial r^2} + \frac{1}{r} \frac{\partial T}{\partial r} = \frac{\rho_m C_m}{k_m} \frac{\partial T}{\partial t} \quad (8)$$

where  $r$  is the radial coordinate,  $t$  is time and  $\rho$ ,  $C$ , and  $k$  are the density, specific heat capacity and thermal conductivity, respectively. The subscript,  $m$ , refers to the metal from which the cylinders are fabricated. Within a pressure vessel the outer surface of the outer cylinder (or cup) is in contact with low conductivity liquid. Therefore at the outermost surface the boundary condition is set at  $\partial T/\partial r = 0$ . Symmetry dictates that at  $r = 0$ ,  $\partial T/\partial r = 0$ .

The shearing gap is very thin compared with the working radius so that curvature of the liquid film can be ignored. A preliminary numerical solution for the liquid film with isothermal boundaries and dissipation showed that for a  $1 \mu\text{m}$  film, steady state temperature distribution was achieved after  $10 \mu\text{s}$  of shearing. Therefore, the storage term in the energy equation for the liquid film is dropped. Including the dissipation term,  $\tau\dot{\gamma}$ , we have for the liquid

$$k \frac{\partial^2 T}{\partial r^2} + \tau\dot{\gamma} = 0 \quad (9)$$

The geometry considered is shown in Figure 7. The liquid being sheared is in the circular gap between the outer and inner cylinders. Only the outer cylinder rotates with a velocity which yields a specified average of the rate of shear,  $\dot{\gamma}$ . The temperature and also the radial heat flux are made continuous at the two metal/liquid interfaces. Equations (8) and (9) in their respective regions are solved numerically with the above boundary conditions and with initial uniform temperature (arbitrarily set to zero for Figure 7) to obtain temperature distribution and shear stress versus time.

The result of a sample computation is shown in Figure 7 for two velocity histories. The velocity of the outer cylinder was increased linearly with time until an apparent or average rate of

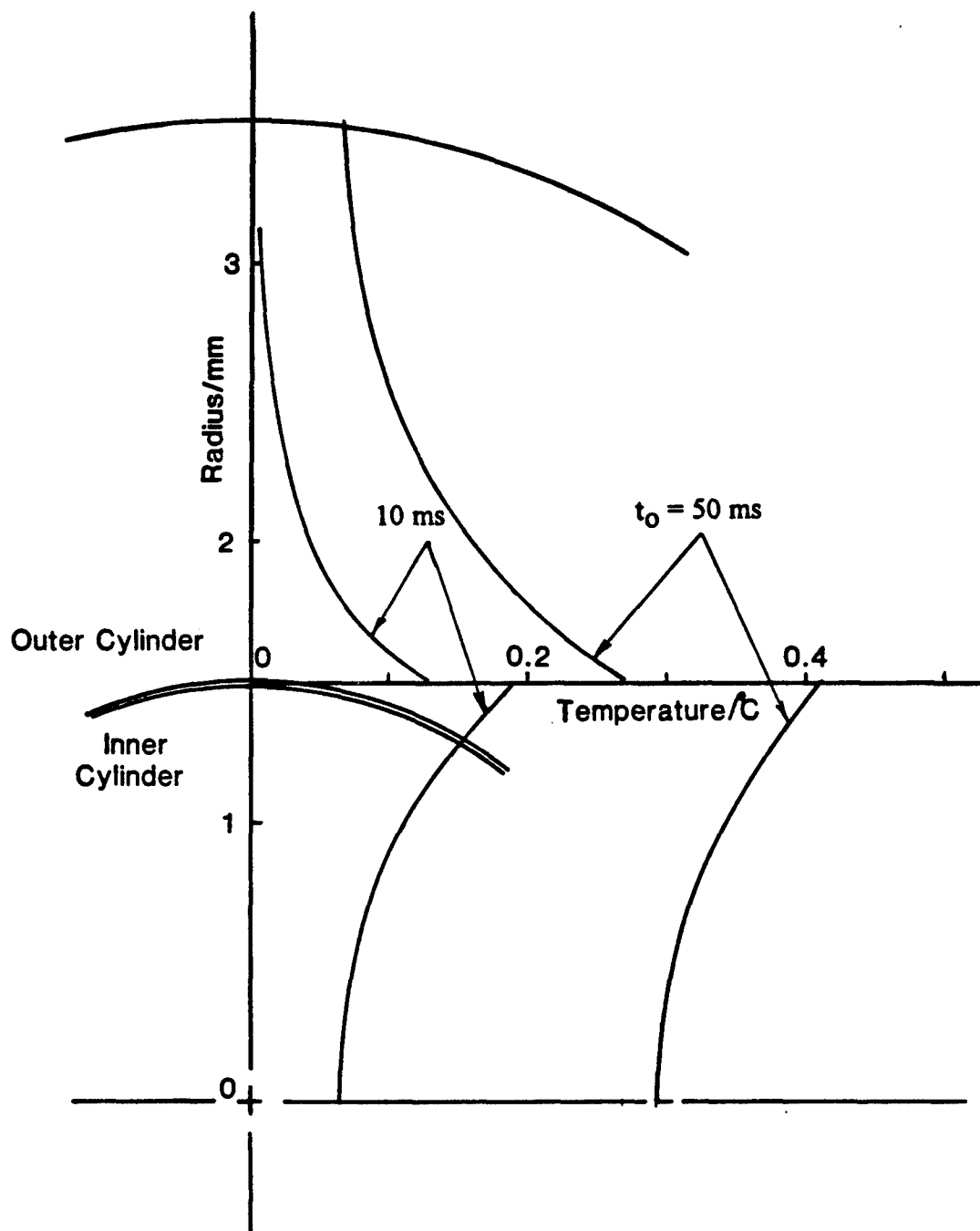


Figure 7. Radial Temperature Distribution in Concentric Cylinders after Velocity Ramp Lasting for Time,  $t_0$ . Result for  $t = t_0$ .

shear of  $10^4 \text{s}^{-1}$  was reached at  $t_0$  equal to 10 and 50 ms. The liquid rheology was Newtonian with  $\mu = 10^3 \text{ Pa}\cdot\text{s}$  and  $\beta = 0.1^\circ\text{C}^{-1}$ . The gap was  $1.0 \mu\text{m}$ . The liquid and metal thermal conductivities were  $k = 0.15$  and  $k_m = 225 \text{ W/m}^\circ\text{C}$  and for the metal  $\rho_m C_m = 3 \times 10^6 \text{ J/m}^3\text{C}$ . The temperature profiles within the metal cylinders are shown in Figure 7 for  $t = t_0$ . The liquid film temperature reached a maximum very near the surface of the inner cylinder. The reduction in shear stress from isothermal was less than 2% for  $t_0 = 10 \text{ ms}$  and less than 4% for  $t_0 = 50 \text{ ms}$ . The rotational velocity in this example is only about 1 revolution per second and can easily be achieved in 10 ms by a stepper motor. Very large driving torque may require a 50 ms linear velocity ramp.

In early high-pressure Couette devices the critical response time was often that of the torque transducer which provides the stress measurement. This transducer is immersed in a high-pressure liquid and for high viscosity the transducer responds as a first order instrument with a time constant,  $t_c$ , which is proportional to damping liquid viscosity. Very fast measurements may be obtained by accelerating both cylinders and then arresting the rotation of one cylinder with the torque transducer which can be filled with a low viscosity liquid. Now, the velocity response is intimately connected with the transducer response. The undamped natural frequency for the transducer is 2.5 kHz. Theoretically, a 5 percent settling time [33] of 0.2 ms can be achieved for transducer response by optimizing the damping liquid viscosity. This is difficult to achieve in practice as the viscosity of the damping liquid changes with the test temperature and pressure. In any event, we have not observed an improvement in measurements typical of those reported here when done faster than 50 ms. The temperature increases shown in Figure 7 present no problem in interpretation of results.

Also, by not considering axial conduction in the cylinders the analysis overestimates the metal temperature rise. Comparing measured stress histories for a Newtonian liquid with the computed stress history at  $t = 1s$  we found the actual loss of shear stress compared to isothermal shear was only 64% of the predicted loss.

The temperature distribution of Figure 7 was incorporated into a thermal-elastic numerical analysis of each cylinder using both plane-strain and plane-stress idealizations. Thermal expansion results in no substantial change in the operating film thickness at the time of the measurement.

## 5.2 Some Results for Pressures to 300 MPa

A high-pressure, high shear stress Couette viscometer was developed [32] in this laboratory to operate at pressures to 300 MPa. The steady shear response of various liquid lubricants [32] and a grease [34] have been investigated. For the grease, an empirical stress equation was found of the form

$$\tau^q = \tau_y^q + (g\mu\dot{\gamma})^q, \tau \geq \tau_y \quad (10)$$

where  $g$  is a dimensionless viscosity enhancement factor approximately equal to 2,  $q$  is a dimensionless exponent and  $\mu$  is the base oil viscosity given by equation (6). For  $q = 0.5$ , equation (10) becomes Casson's equation for oil/particulate mixtures.

Flow curves are presented for a high-traction fluid, Santotrac 50 and a mineral oil, LVI 260 in Figures 8 and 9, respectively. Although the pressures and temperatures are comparable the shear response is quite different. The traction fluid remains Newtonian to a shear stress of at least 10 MPa whereas the mineral oil responds non-linearly above 3 MPa. Note also that for the

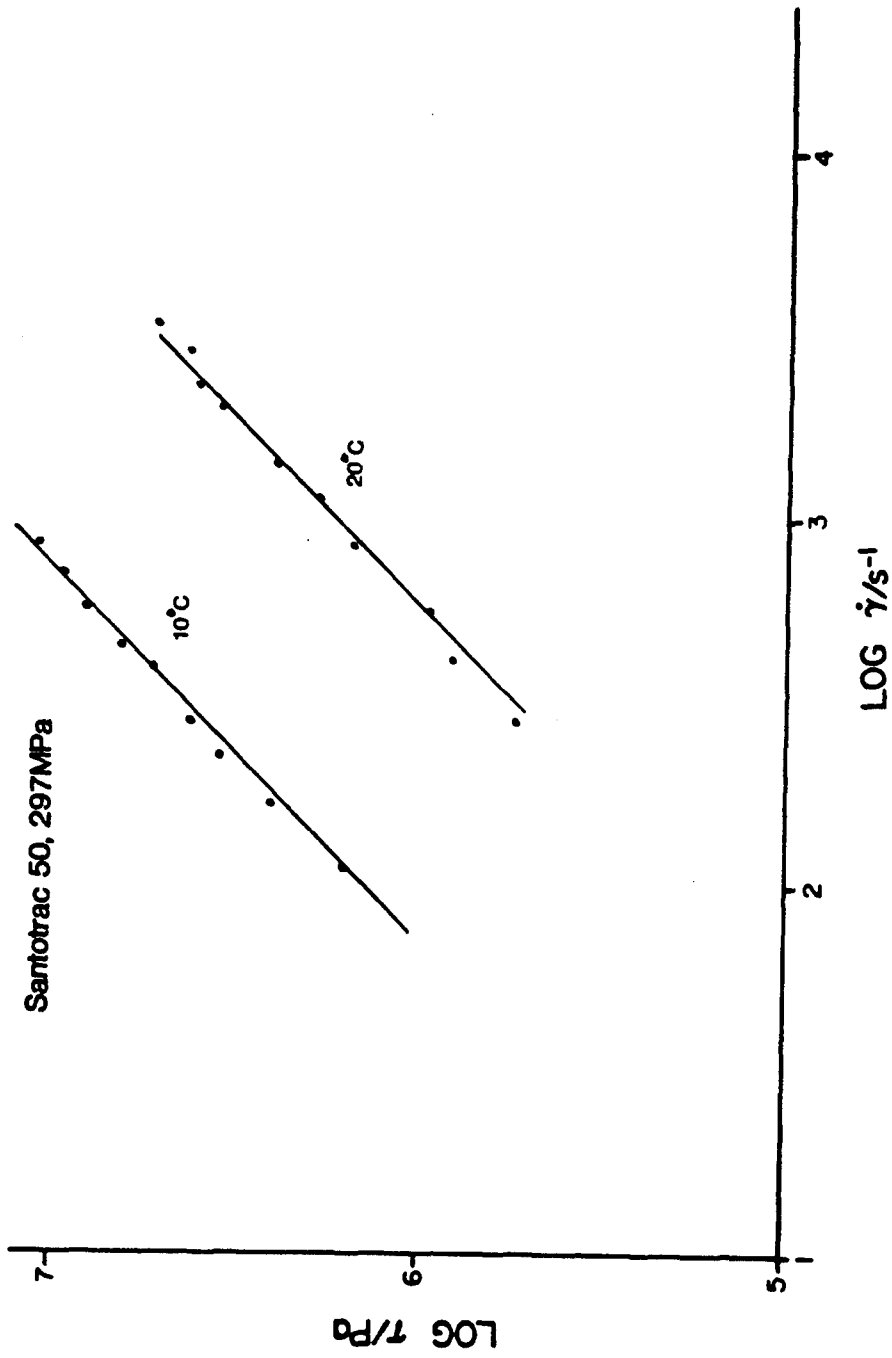


Figure 8. Flow Chart for Santotrac 50,  $p = 297 \text{ MPa}$ .

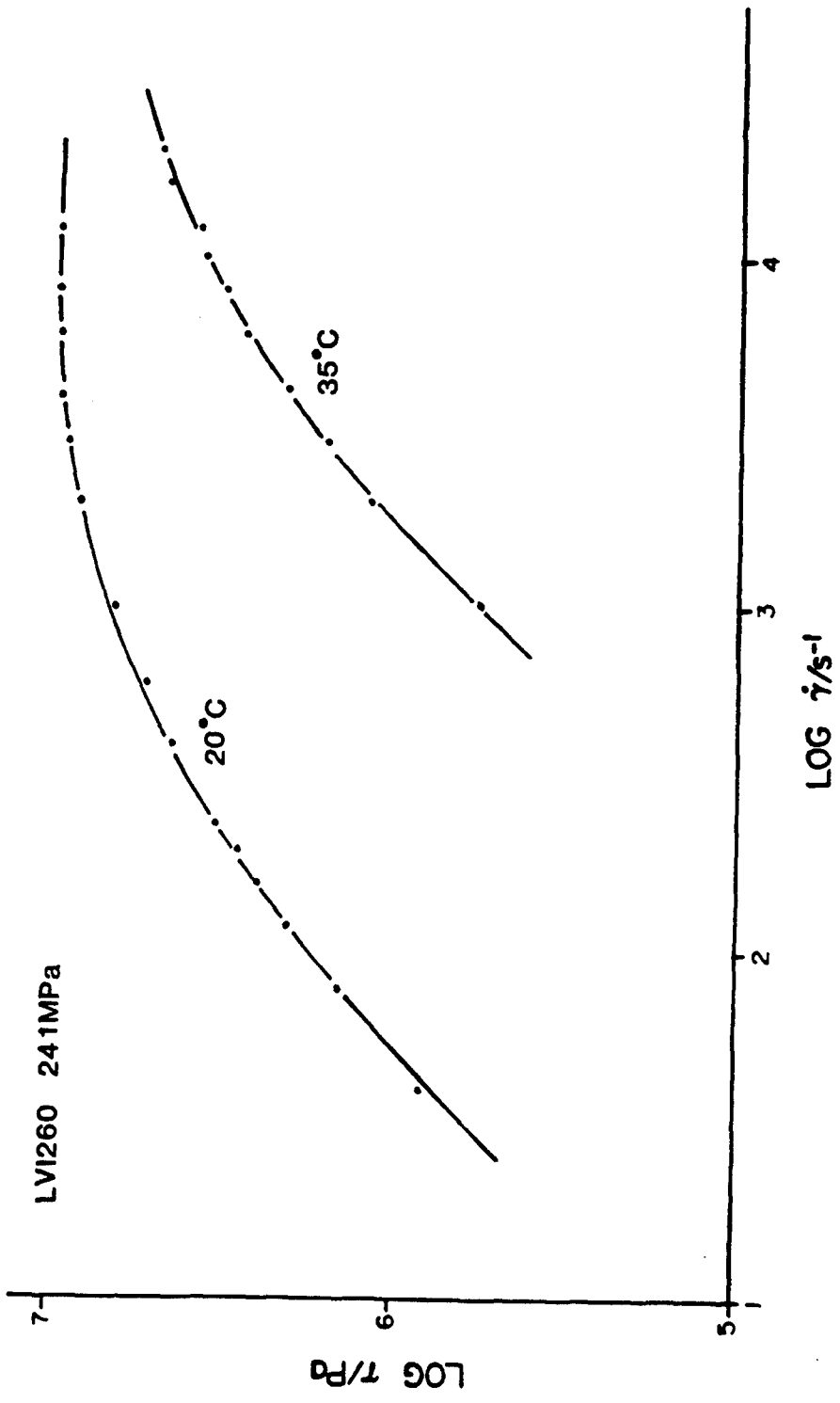


Figure 9. Flow Chart for Mineral Oil, LVI 260, p = 241 MPa.

mineral oil, the stress becomes essentially independent of rate at about  $\tau = 10$  MPa and that the temperature dependence diminishes as the rate dependence diminishes as predicted by eqn. (3). Because of their extended Newtonian response we have begun to use the cycloaliphatic traction fluids as viscosity standards for shear stress greater than 1 MPa in calibrating cylinder gaps.

### 5.3 A New High-Stress Couette Viscometer for 600 MPa Pressure

An increase in the pressure capability of previous rotating concentric cylinder viscometers is necessary to investigate the shear response of typical lubricants well above the glass transition temperature. Translating concentric cylinder rheometers are capable of pressures above 1 GPa; however the rate of shear is so low that the viscosity must be made very large (by operation near  $T_g$ ) in order to achieve an interesting magnitude of shear stress.

We recently reported [32] the development of a Couette viscometer for pressure to 300 MPa and the results of the previous section were obtained with that device. The pressure capability of the Couette technique is doubled with the device shown in section view in Figure 10. The outer cylinder (cup) is driven by an external stepper motor by means of a drive shaft. The thrust bearing which prevents expulsion of the shaft from the vessel has been moved to outside of the vessel so that the bearing does not run in pressurized liquid. The high-pressure seal is now a simple spring-loaded packing. There is no need for high-pressure electrical feed-throughs since the torque measurement is transmitted out of the vessel optically. The inner cylinder (bob) is restrained from rotation by a torsion bar with a mirrored surface within a glass tube. See Figure 10.

The principle of the torque measurement is depicted in Figure 11. The twist of the torsion bar results in a deflection of a laser beam which is detected by an optical position sensor. A glass

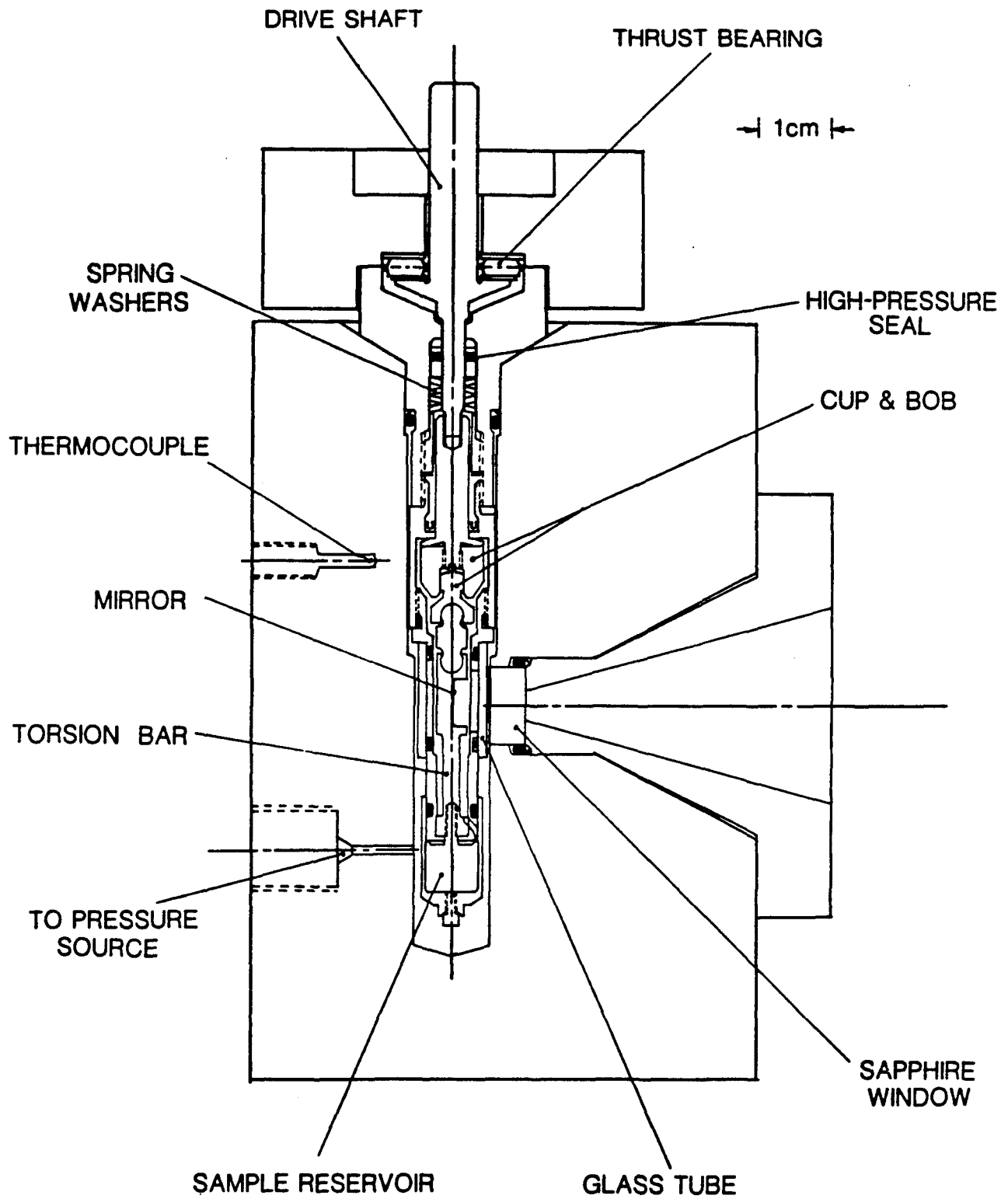


**Figure 10. High-Pressure High Shear Stress Viscometer for 600 MPa Pressure.**

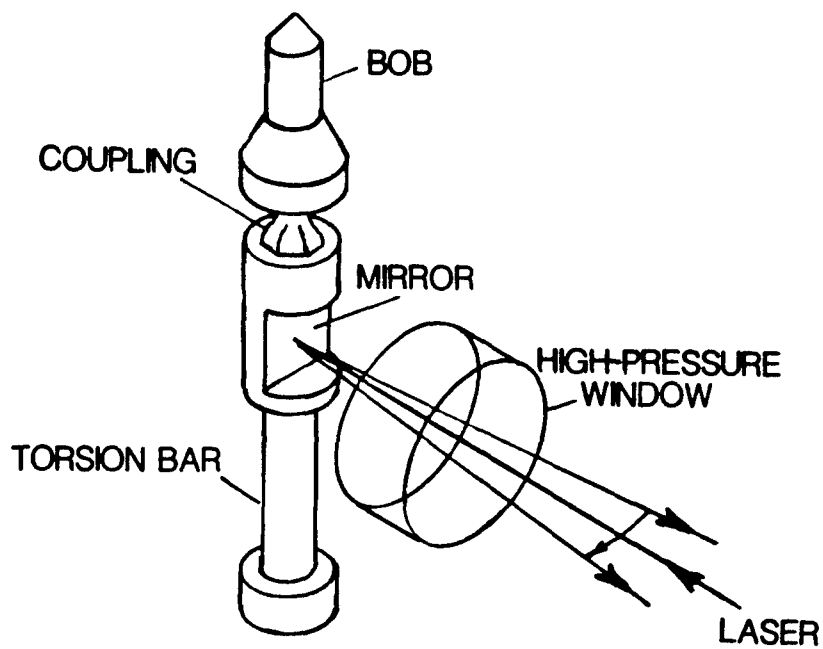


**Figure 11. Torque Transducer Operating Principle for Rheometer Shown in Figure 10.**

tube (Figure 10) provides a circular interface between the liquid which surrounds the mirror and the pressurizing fluid so that changes in refractive index of individual samples need not be accounted for. For highly viscous or opaque samples, the transducer is filled with a low viscosity fluorinated oil which is immiscible with the sample.

#### 5.4 Results for Pressures to 600 MPa

A flow chart is presented for the polyalphaolefin, SHF1001, in Figure 12. The response is apparently Newtonian to about 2 MPa shear stress, although the effective viscosity below 2 MPa is slightly reduced compared to falling body measurements.

The mineral oil, HVI 650, has been the subject of numerous traction experiments. The shear response of HVI 650 is depicted in Figures 13 a and b. The curves drawn through the data points for 23°C and 44°C represent the empirical Carreau-Yasuda equation

$$\tau = \mu\dot{\gamma} \left[ 1 + \left( \frac{\mu\dot{\gamma}}{\tau_L} \right)^a \right]^{(m-1)/a} \quad (11)$$

Here,  $a$  is a dimensionless parameter which controls the breadth of the transition from Newtonian to a non-Newtonian flow regime with rate sensitivity coefficient of  $m$ . For  $m = 0$ ,  $\tau_L$  is a limiting shear stress. In Figures 13 a and b, we used  $a = 1.5$  at 23°C and  $a = 2$  at 44°C. For the limiting stress, the form proposed by Bezot, et al. [35] was adopted

$$\tau_L = c_0 + c_1 p + c_2 p^2 \quad (12)$$

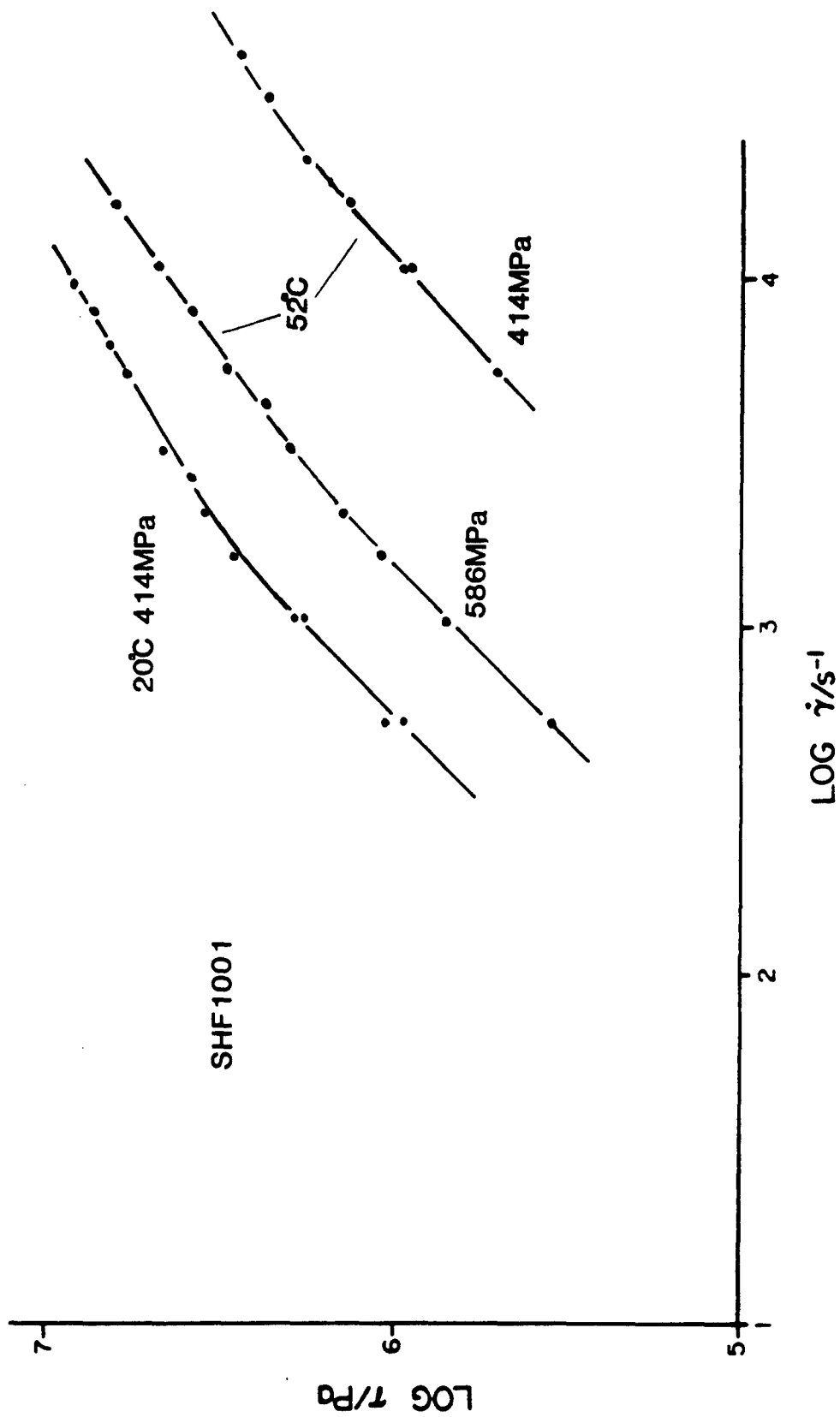


Figure 12. Flow Chart for a Polyalphaolefin.

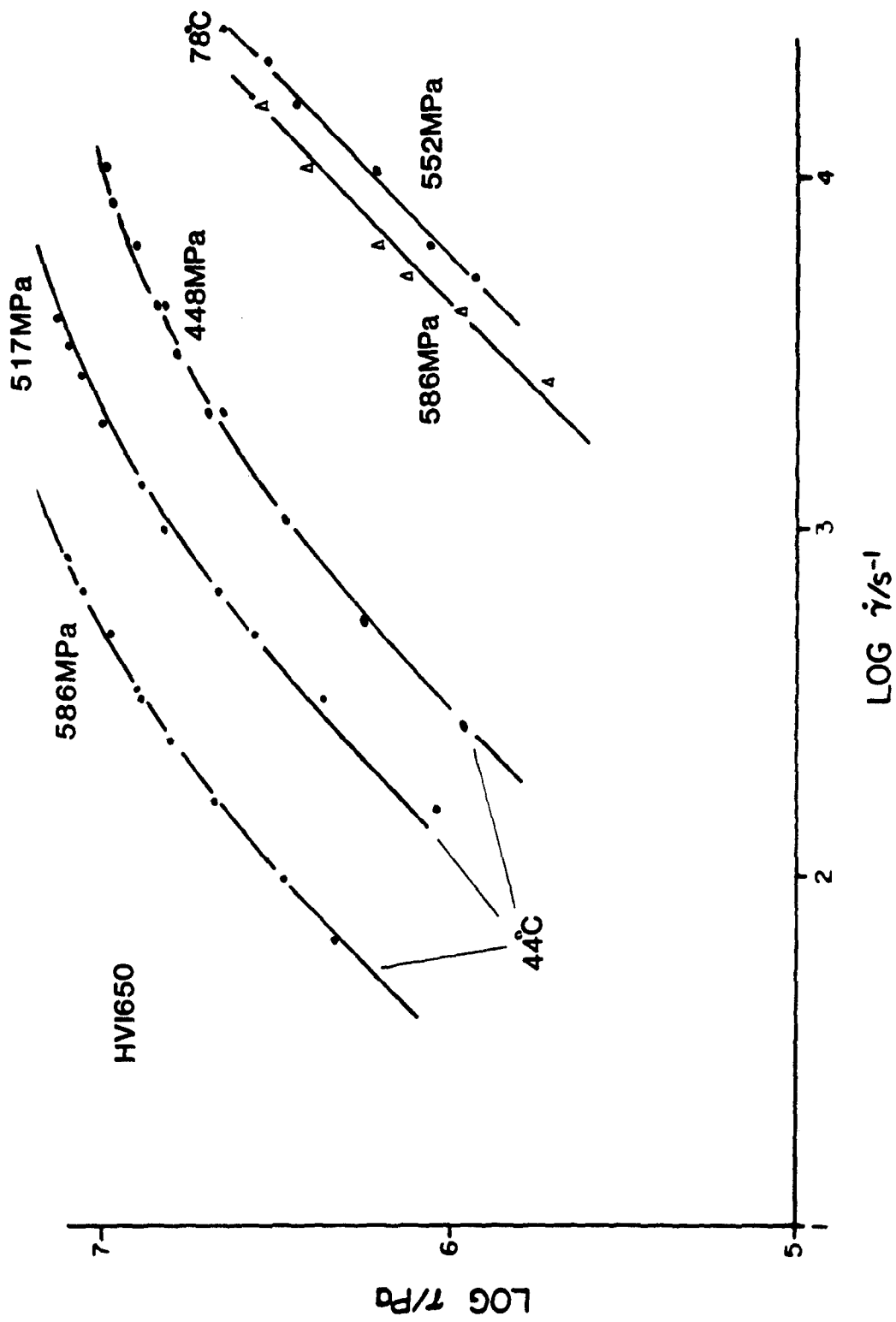


Figure 13a. Flow Chart for HVI 650.

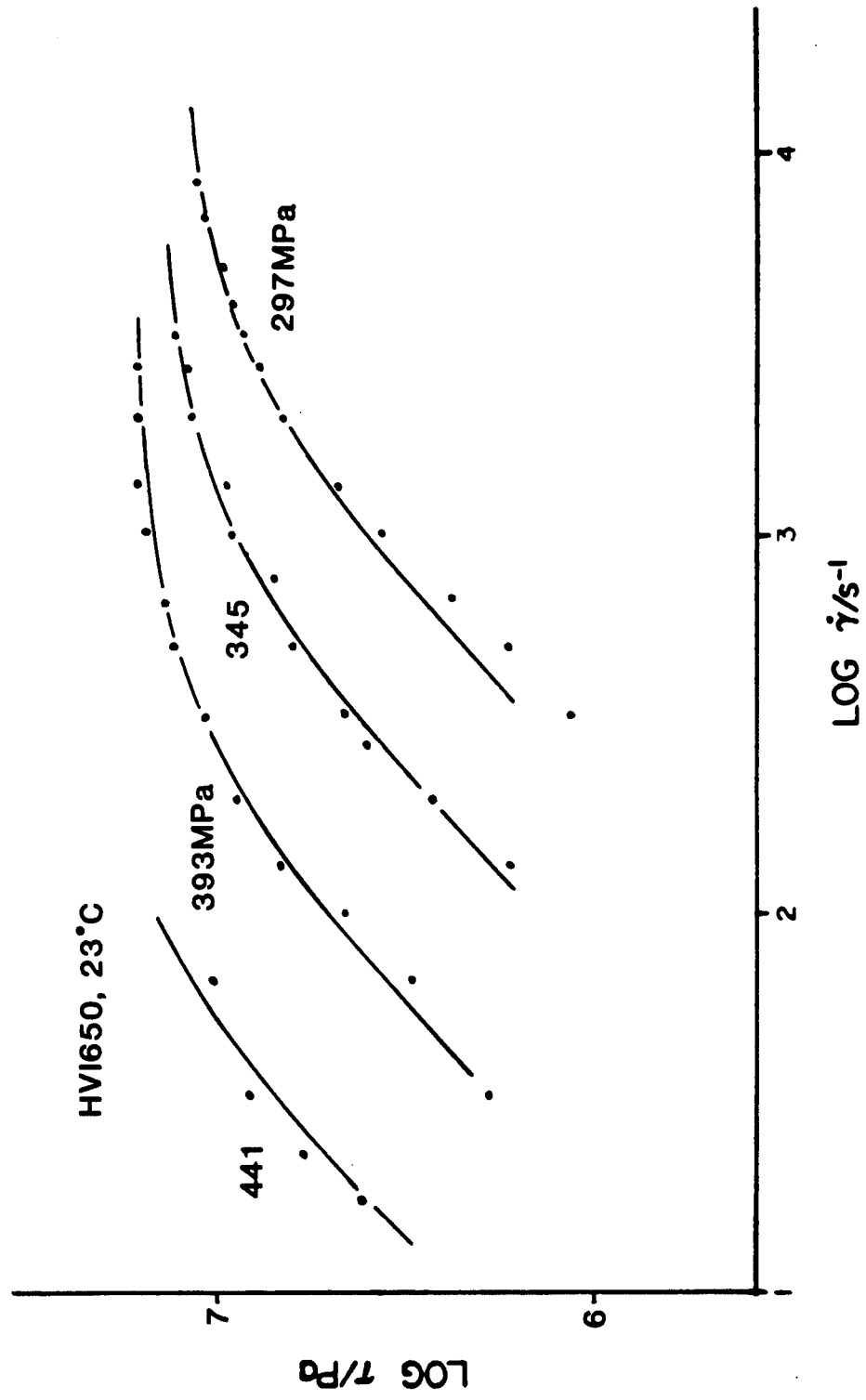


Figure 13b. Flow Chart for HVI 650.

Using the results of Figure 13b and Ref [36] and [37], we obtained  $c_1 = 0.034$  and  $c_2 = 2.1 \times 10^{-5}$  MPa with  $c_0$  arbitrarily set to zero. Note that for HVI 650 at 44°C (Figure 13a) the curves are also a good approximation of the Sinh Law,

$$\tau = \tau_0 \sinh^{-1}(\mu\dot{\gamma} / \tau_0) \quad (13)$$

Where  $\tau_0$  is a stress which represents the limit of Newtonian response and is 3.3, 5.2 and 6.5 MPa for pressures of 448, 517 and 586 MPa respectively. That is,  $\tau_0 \approx \tau_L / 4$  at 44°C.

The shear response of the traction fluid, Santotrac 40, is shown in Figure 14. For the pressure of 414 MPa, the solid curve is equation (11) and the two broken curves are equation (13) for  $\tau_0$  of 6 and 25 MPa respectively. When elastohydrodynamic traction curves are interpreted in terms of equation (13) together with exponential pressure-viscosity the traction gradient can be set equal to  $\tau_0$  [36]

$$\frac{\partial \bar{\tau}}{\partial \ln \dot{\gamma}} = \tau_0 \quad (14)$$

Values of  $\tau_0$  obtained from traction tests using (14) are typically less than 6 MPa [36, 38] for cycloaliphatic traction fluids under conditions of Figure 14. Clearly, from Figure 14, the Newtonian limit exceeds 6 MPa and is close to 25 MPa. Therefore, any interpretation of the traction gradient as a Newtonian limit through a Sinh Law model with  $\tau_0$  independent of pressure must be suspect. However, if the pressure of a rheological measurement is chosen carefully it should be possible to obtain agreement between the Newtonian limit for that particular pressure and the traction gradient since the Newtonian limit is pressure dependent (eg., HVI 650 at 448 MPa and 44°C).

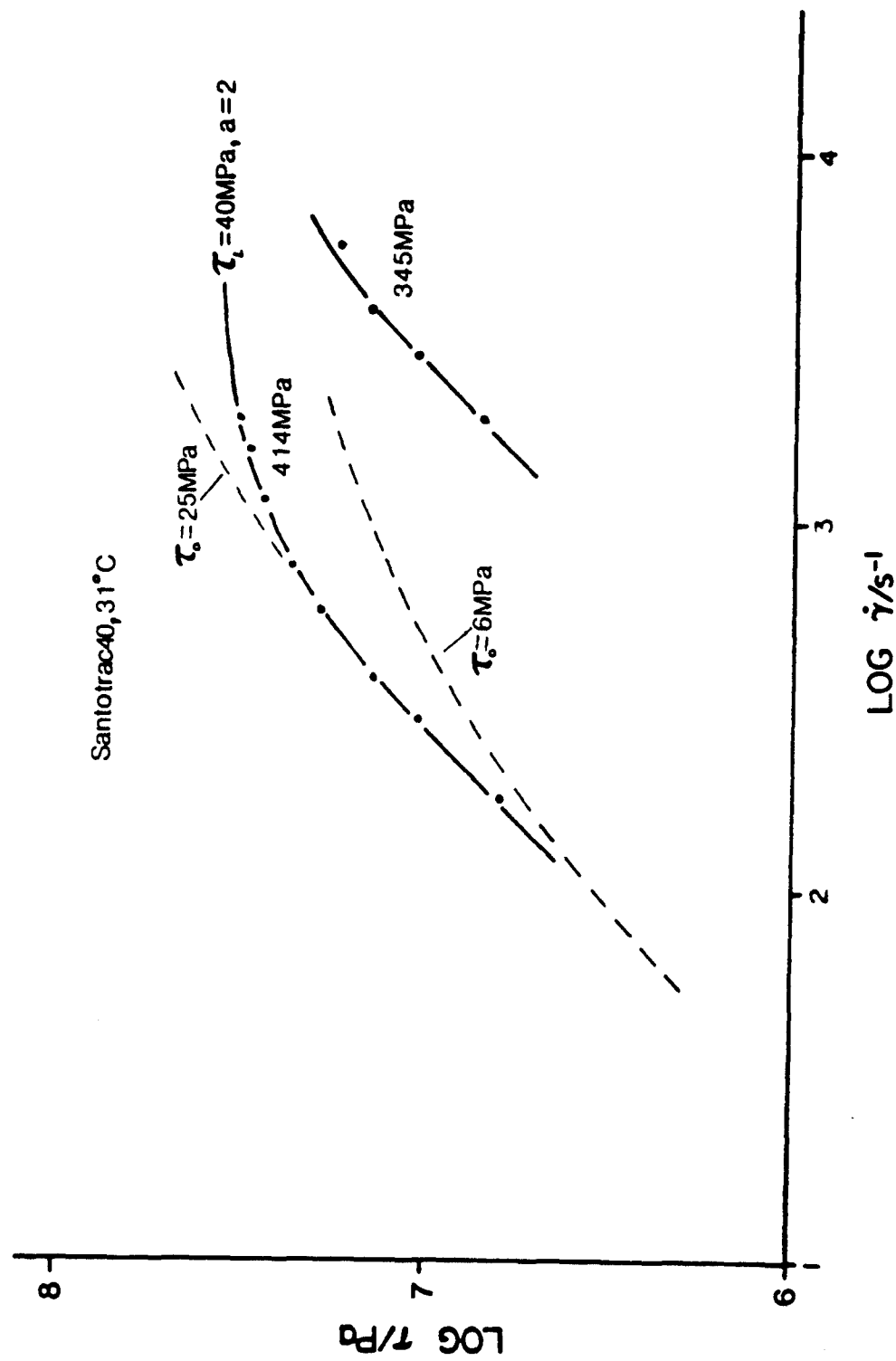


Figure 14. Flow Chart for Santotrac 40

We have investigated the grease from Ref [34] and its base oil in the current rheometer to explore departures from Newtonian behavior at high shear stress. In Figure 15, for room temperature, the mineral base oil, 600P, is non-Newtonian above  $\tau = 2$  MPa at 310 MPa pressure. When the pressure is increased to 517 MPa this oil is Newtonian to  $\tau = 3$  MPa. The CA7000, which is a soap-thickened grease of 600P, is also shown in Figure 15. It would appear from these limited data that the shear stress for the grease (at high stress) may be obtained by multiplying the base oil result by the previously [34] obtained viscosity enhancement factor,  $g$ , which is about 2. Clearly, equation (10) is not applicable here since it reverts to Newtonian at high shear stress.

The High-Pressure Impact Viscometer of Wong, et. al. [39] entraps a quantity of liquid between a ball and a plate. Interferometry is used to determine the local flow rate of liquid leaking from the entrapment and local surface distortion which yield local pressure from elasticity theory. A Rabinowitsch Correction for slit flow gives the true shear rate at the surface. The authors concluded that the effective viscosity was found in earlier works to be a function of time because the shear rate varied with time while the shear stress remained at the limiting value. Limiting stress type behavior was observed over 4 decades of shear rate with  $m \approx 0.01$  for LVI 260.

## 6. EHD TRACTION CALCULATION

We should expect our property measurements to yield reasonable predictions of concentrated contact traction. Evans [40] generated isothermal, line-contact traction curves for three of the most widely investigated liquid lubricants: 5P4E, Santotrac 50 and HVI650. These data were described as isothermal since the disc temperature was adjusted to provide a constant

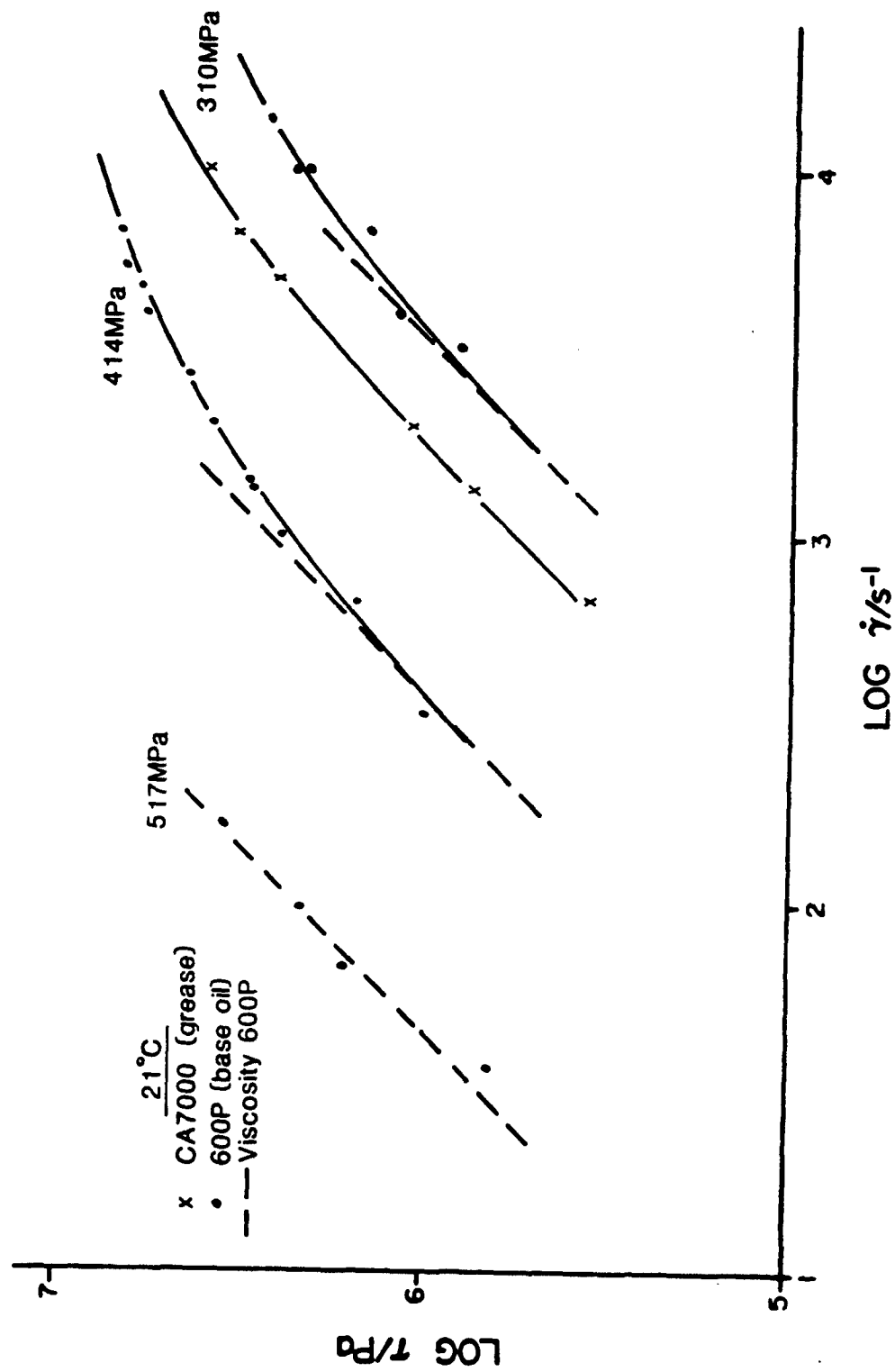


Figure 15. Flow Chart for Grease and Base Oil.

estimated average film temperature. These traction data are presented for HVI650 in Figure 16 for inlet temperatures of 40 and 60°C and average pressures,  $\bar{p}$ , of 0.47 and 0.63 GPa. The sliding velocity is  $\Delta U$  and inlet temperature rise is 3°C.

For the traction calculations which are the curves in Figure 16, we assumed the Hertzian pressure distribution and integrated the Carreau-Yasuda equation (11) across the contact area to obtain the average shear stress,  $\bar{\tau}$ . The dimensionless parameter,  $a$ , was specified by  $a = 63/(T+19^\circ\text{C})$  which yields the values obtained in the previous section without approaching the meaningless condition of  $a = 0$  at ordinary temperatures. Viscosity and limiting stress were obtained from equations (6) and (12). Results were insensitive to the selection of the rate sensitivity,  $m$ , from 0 to 0.03. Although the predicted curve at 40°C rolls over more quickly than the measured traction, the general agreement is good. Considering the great differences between the two techniques and the assumptions involved (eg., Hertzian pressure) it might be unreasonable to expect to do better.

## **7. NEW OBSERVATIONS OF MECHANICAL SHEAR BANDS IN SIMPLE PLANE SHEAR**

The High-Pressure Flow Visualization Cell which we use to optically observe shear bands has been described in detail in Ref. [4] as well as the experimental procedures and preliminary results. It was shown that at a critical shear stress which marked the limit of linear response, an intermittent slip occurred across visible bands. The existence of two types of bands with differing orientation is now recognized [41]. Figure 17 illustrates the orientations of the two types. New observations which give insight into the slip mechanism are presented in the next sections.

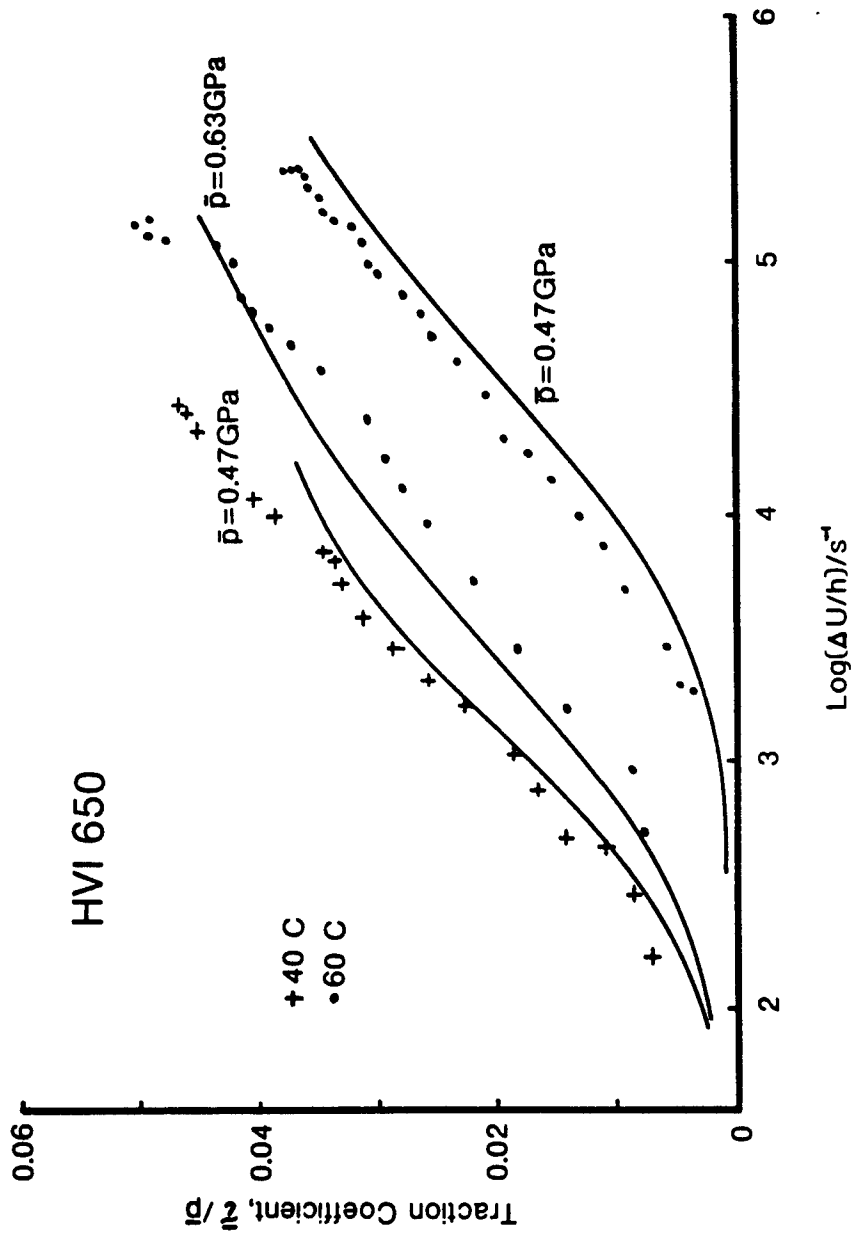
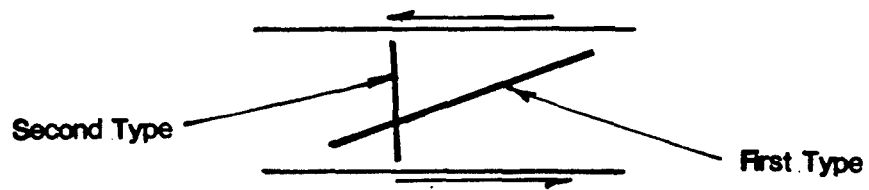


Figure 16. Measured and Predicted Traction Curves for HVI 650.



**Figure 17. Two types of mechanically induced shear bands.**

## 7.1 Birefringence

Flow birefringence has been useful for stress analysis in flowing liquids in a manner analogous with photoelasticity in transparent solids [42]. Molecular orientation under stress gives rise to optical anisotropy - the refractive index,  $n$ , is different in different directions. Birefringence observations can be used to determine the principal normal stress difference,  $\Delta\sigma$ , and the orientation of the principal stress axes if a suitable calibration of the birefringence,  $\Delta n$ , can be obtained. Such a calibration is not possible with the flow cell. However, some generalizations regarding the stress distribution in the flow field may be obtained.

The High-Pressure Flow Visualization Cell was placed between crossed polarizers. White light was filtered to produce a narrow band at 605 nm. The polyphenyl ether, 5P4E, was the model lubricant. Temperature was 23°C and pressure was 241 MPa. The shearing force was increased with time until shear bands were observed. The interference pattern shown in Figure 18 was obtained just before the shear localized. This fringe pattern disappeared at the time the shear bands formed. Similar experiments were performed with the crossed polarizers placed at eight different angles with respect to the shear direction equally spaced over a span of 180° in an attempt to determine the extinction angle. No effect of orientation of the polarizer/analyzer pair was noted on the contrast or geometry of the fringes or shear bands.

Apparently, the high-pressure windows which are sapphire are performing as fractional wave plates to eliminate the extinction angle effect [42] and so it was not possible to obtain the principal stress directions. It is possible to obtain the stress distribution in a qualitative sense. If the stress-optical function is monotonic [43], then the fringe order is a representation of the relative magnitude of the principal normal stress difference (and the principal shear stress).

5P4E  
35 kpsi, 23°C  
# 151 08:37

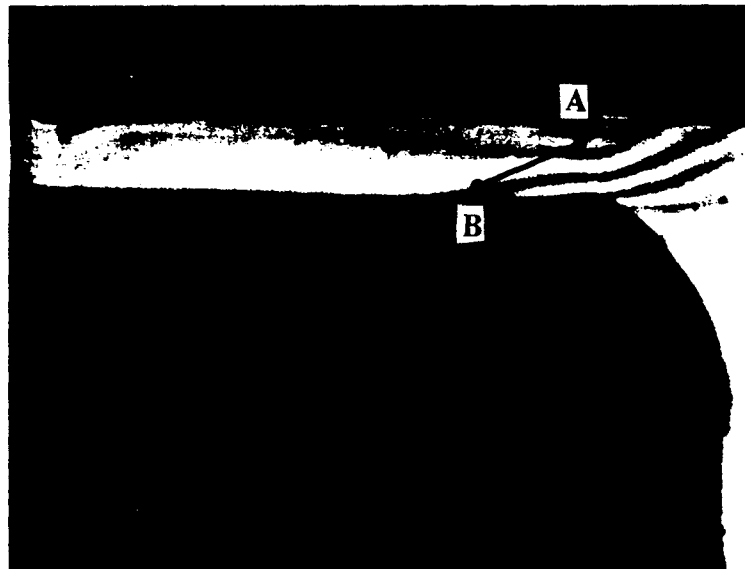


Figure 18. Flow birefringence in 5P4E at 23°C, 241 MPa.

Referring again to Figure 18, the zeroth order fringe occurs in the liquid reservoir far to the right in the figure. The principal shear stress should be a maximum within the highest order fringe in the region marked A. Notice that the shear stress is uniform in the shearing gap at positions farther than about 3 times the film thickness into the gap.

It was previously noted [4] that the first band nucleates at the point A and runs to the point marked B in Figure 18. Two conclusions may be drawn from this observation. 1) The reason for the observation of the first bands near the entrance is that the shear stress is greatest there. 2) A band which nucleates within a region, A, of locally high stress (compared to the average stress within the field) will continue to run through a region of locally lower (than the average) stress. The significance of the latter is important. Once initiated the shear band defines a plane on which slip is more easily accommodated than in the bulk of the material - it becomes a "weak spot" and the slip is arrested only by pinning at the solid boundaries of the film.

## 7.2 Persistence of Shear Bands

When mechanically induced shear bands are studied in solid amorphous polymers, the observations are usually made on sectioned specimens [24] long after the deformation responsible for the bands has ceased. This is possible because the image of the band, which is probably a result of damage or dilatation, persists. In the liquid lubricants this persistence time is shorter. In Figure 19 we have plotted the time for which a shear band was visible in 5P4E after shearing (persistence time) versus the viscosity at test conditions. If we define the mechanical shear relaxation time as the ratio of viscosity,  $\mu$ , to shear modulus,  $G$ , then the straight line plotted in Figure 19 is the mechanical relaxation time for  $G = 1$  GPa. We may define a characteristic time

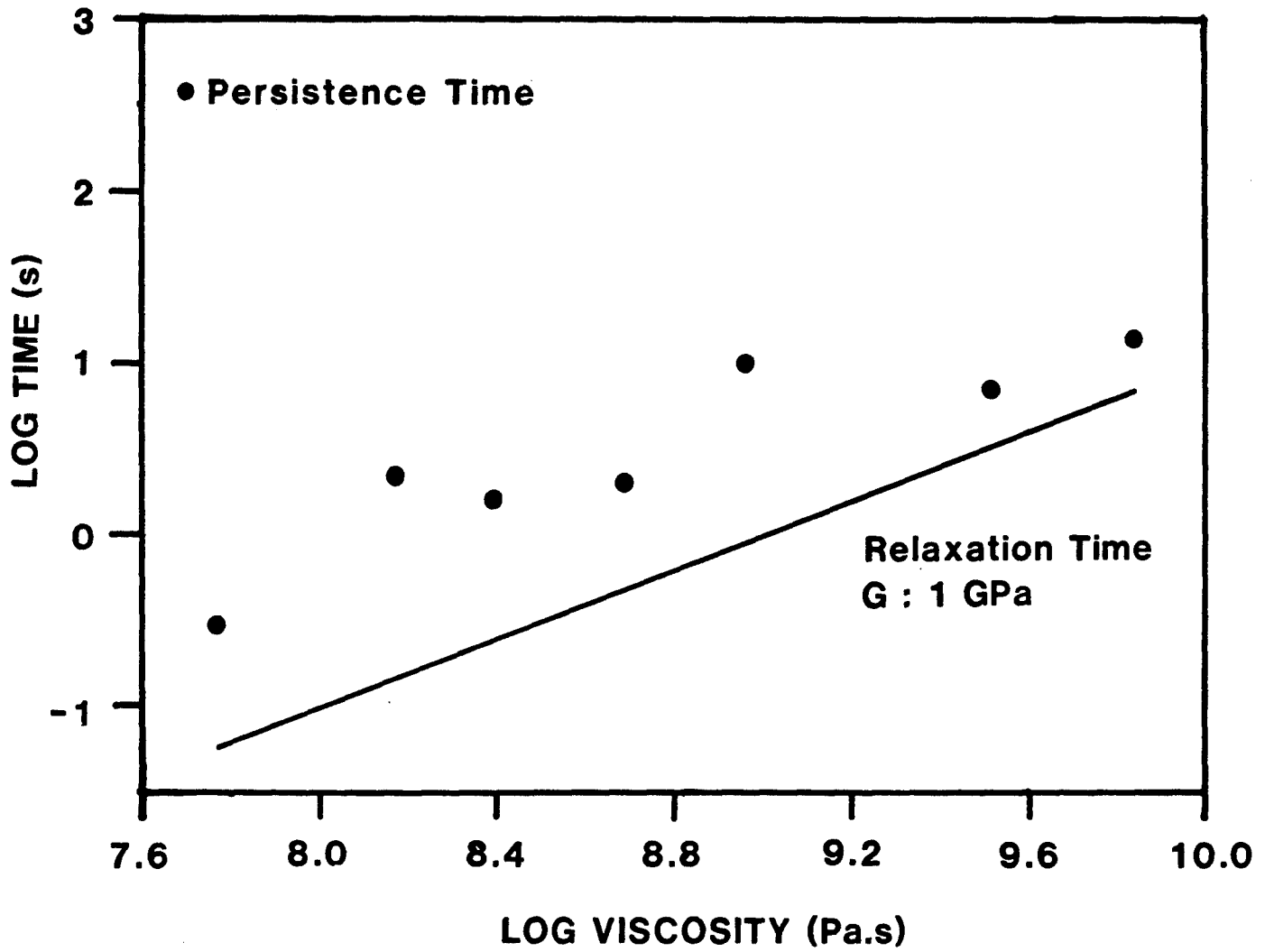


Figure 19. Time for which a shear band is visible.

for thermal diffusion as  $h^2/D$  where  $h$  is the thickness of the band and  $D$  is thermal diffusivity.  $D$  is essentially independent of  $\mu$  and is typically about  $10^{-7}$  m<sup>2</sup>/s for liquid lubricants. If a shear band is at most 2 $\mu$ m thick, then the characteristic time for thermal diffusion is at most 40 $\mu$ s. The correlation of persistence (of the order of seconds) with mechanical relaxation is much better than for thermal diffusion. Clearly the image of the shear band is a result of mechanical damage or dilatation and not temperature.

### 7.3 Dilatation

A related observation concerns the degree of contrast of the shear band images. Among the liquids in which we have observed shear bands is the perfluoropolyalkyl ether, 143AD. In this material the bands appear so faint that it is difficult to reproduce them on a video print. The refractive index,  $n$ , is related to density,  $\rho$ , through the Lorenz-Lorentz equation.

$$\frac{1}{\rho} \frac{n^2 - 1}{n^2 + 2} = \text{constant} \quad (15)$$

From this we can obtain

$$\frac{-dn}{d\varepsilon} = \frac{\rho dn}{d\rho} = \frac{(n^2 - 1)(n^2 + 2)}{6n} \quad (16)$$

where  $\varepsilon$  is the dilatation. The refractive index of 143AD is 1.30 and the refractive index of 5P4E is 1.63. Inserting these values into eqn. (16) we find that the rate of change of  $n$  with respect to  $\varepsilon$  is -0.3 for 143AD and -0.8 for 5P4E. So for the same dilatation the refractive index changes three times less for the perfluoropolyalkyl ether than it does for the polyphenyl ether. Thus the relative degree of contrast in shear band images is consistent with an argument that a persistent dilatation has occurred along the band.

## 7.4 Surface Roughness Effect

It might be argued that the roughness of the solid boundary provides a nucleation site for shear bands. The moving shaft which performs as one (the moving one) of the solid boundaries has two sides - each of which may be utilized in an experiment. One side was left as machined with an rms roughness of 1.0  $\mu\text{m}$ . The other side was polished to a roughness of 0.03  $\mu\text{m}$ . The stationary surface has a roughness of 0.3  $\mu\text{m}$  rms. Both sides of the moving shaft has been utilized. No difference in the character of the bands or the manner in which they developed was noted. We, therefore, cannot associate surface roughness, at least up to 1  $\mu\text{m}$ , with shear localization in liquid films.

## 8. SLIP CRITERION

### 8.1 Analogy to Glassy Polymers

In previous work [4], we have associated mechanically induced shear bands with the rate-independent shear stress which is observed in liquid lubricants under pressure in disc machines and rheometers. As a critical stress which is roughly proportional to pressure is approached, an increasing amount of the deformation in an otherwise rate-dependent matrix is accommodated by intermittent slip along inclined shear planes. When this critical (limiting) stress is reached, any increase of the apparent rate of shear can be accommodated by an increased production of shear bands without changing the stress: the response is rate-independent.

In practice, for glassy polymers, the strain rate sensitivity coefficient  $m = \partial \ln \tau / \partial \ln \dot{\gamma}$ , and be quite low when shear bands are operating. Here,  $\tau$  is shear stress and  $\dot{\gamma}$  is rate of shear. G'Sell [44] reports that  $m = 0.027$  for polycarbonate with shear bands. Such a low rate sensitivity

(6% per decade) would possibly be undetectable in high-pressure rheometers and disc machines; hence the limiting shear stress idealization.

Glassy polymers are known to exhibit a pressure dependent shear strength which at high pressure follows the rule [24]

$$\tau_y = \tau_{y0} + \lambda_y p \quad (17)$$

where  $\lambda_y$  varies from 0.1 to 0.25 and  $p$  is pressure. A similar rule is known to apply to the limiting shear stress of liquid lubricants, although with a lower proportionality constant.

## 8.2 Mohr-Coulomb Criterion

The Mohr-Coulomb criterion predicts that slip will occur along any plane on which the ratio of shear stress,  $\tau_\theta$ , to compressive normal stress,  $-\sigma_\theta$ , attains the magnitude of a material friction coefficient,  $\eta$ . Referring to Figures 20 and 21,  $\tau_\theta$  and  $\sigma_\theta$  may be resolved from the shear stress,  $\tau$ , and normal stresses  $\sigma_x$  and  $\sigma_y$  which are oriented along and perpendicular to the solid boundaries in a plane shear experiment. The mean mechanical pressure,  $p$ , is defined by  $p = -\frac{1}{2}(\sigma_x + \sigma_y)$  and  $\lambda = \tau/p$ .

In general, the normal stresses will not necessarily be equal and we will quantify the first normal stress difference,  $N_1 = \sigma_x - \sigma_y$  by  $\xi = N_1/2p$ . The parameters  $\lambda$  and  $\xi$  are dimensionless.

We may resolve

$$-\sigma_\theta = p + \xi p \cos 2\theta - \tau \sin 2\theta \quad (18)$$

$$\tau_\theta = \tau \cos 2\theta + \xi p \sin 2\theta \quad (19)$$

The slip criterion can be represented graphically on the Mohr's circle plot in Figure 20. The Mohr's circle of stress must fit within the envelope defined by the broken lines. These lines

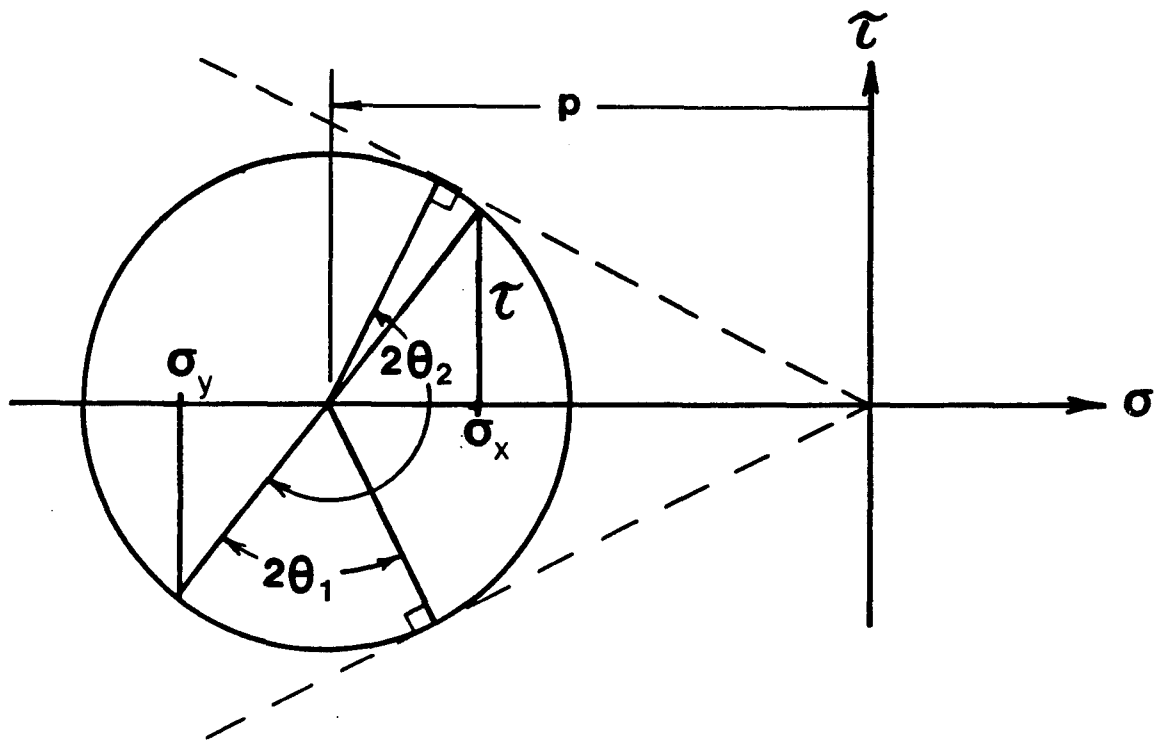


Figure 20. Mohr's circle representation of slip criterion.

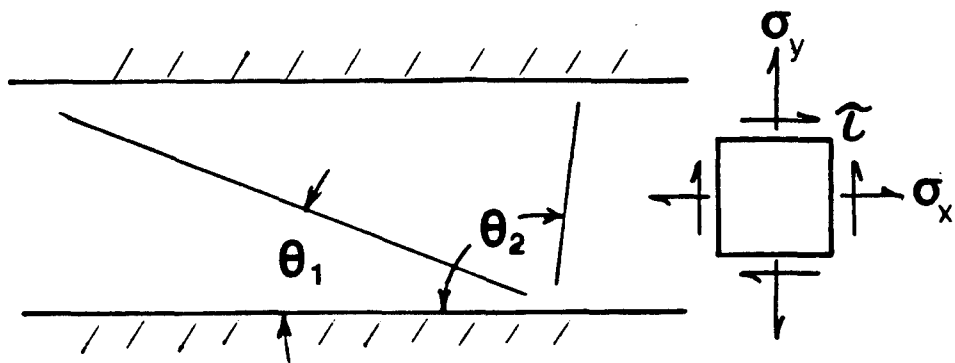


Figure 21. Definitions of angles and stresses.

must curve away from the  $\sigma$  axis near  $p = 0$  to allow a non-zero shear stress there. The included angle of the envelope is twice the material friction coefficient  $\eta$ . Now, slip will occur when the circle of stress increases to tangency with the envelope and the orientation of the band will be such that  $|\tau_\theta / \sigma_\theta|$  is maximized. This is satisfied by the two radii of the circle drawn to the points of tangency. These radii represent the two shear band angles,  $\theta_1$  and  $\theta_2$  in Figure 21.

Analytically, the shear band angles can be found by setting

$$\left. \frac{d}{d\theta} \left( \frac{\tau_\theta}{-\sigma_\theta} \right) \right|_{\theta=\theta_c} = 0 \quad (20)$$

which leads to

$$\lambda^2 + \xi^2 - \lambda \sin 2\theta_c + \xi \cos 2\theta_c = 0 \quad (21)$$

The two solutions for  $\theta_c$  are the shear band angles  $\theta_1$  and  $\theta_2$  for the first and second types respectively. The material friction coefficient is

$$\eta = \frac{\lambda \cos 2\theta_c + \xi \sin 2\theta_c}{1 + \xi \cos 2\theta_c - \lambda \sin 2\theta_c} \quad (22)$$

If the first normal stress difference  $N_1$  were zero, then the two shear band angles would be complimentary angles (sum to  $90^\circ$ ) defined by solutions of  $\theta_c = \frac{1}{2} \sin^{-1} \lambda$ . Clearly the shear band angles in Figure 17 are not complimentary. It will be necessary to invoke the first normal stress difference to reconcile theory with observation.

For example, from Figure 17 for the polyphenyl ether,  $\theta_1 = 19^\circ$  and  $\theta_2 = 103^\circ$ . Then  $\lambda = 0.089$  and  $\xi = 0.056$  are obtained from equation (21). This value of  $\lambda$  is in agreement with the measured [32] limiting shear stress if  $\lambda$  is applied to a linear equation like (17). The first normal stress difference obtained is a little more than the shear stress. This may seem excessive, since

consideration of the normal stress difference has not been necessary to predict bearing load capacity; however, Tanner [45] showed that for typical lubrication flows the fractional increase in load capacity is unaffected by  $N_1$  of the order of  $\tau$ . The experimental measurement of  $N_1$  at high pressure is challenging and has not previously been attempted - possibly because of the expected irrelevance to bearing load capacity. Measurement of  $N_1$  could confirm the applicability of Mohr-Coulomb and might be considered a research priority.

In the example above, the material friction coefficient,  $\eta = 0.106$ . The value of  $\eta$  is simply the difference between  $\pi/2$  and the included angle between the two types of band (in radians). Since this included angle is very nearly  $\pi/2$ , the determination of  $\eta$  (and  $\lambda$ ) from observations of bands is sensitive to the accuracy of the shear band angle measurement.

The first normal stress difference,  $N_1$ , in simple shear was the subject of conjecture and controversy early in the study of high-pressure rheology of lubricants; however there has been no attempt to measure this effect under pressure. Gleissle [46] empirically associated flow instabilities with a critical ratio of 1st normal stress difference to shear stress. He found that for melt fracture in capillaries  $N_1/\tau = 4.6$  and alluded to an unpublished analysis which predicted instability for  $N_1/\tau > 4$ . Abdel-Khalik, et al. [47] present a method of predicting  $N_1$  from measured flow curves. They considered (among others) eqn (11) with  $a = 2$  and  $m = 0$ . Their result is that  $N_1/\tau = 1.26$  for  $\mu\dot{\gamma}/\tau_L = 0.35$  which is somewhat consistent with the appearance of bands at the onset of non-linearity. For  $N_1/\tau = 4.6$ , Gleissle's limit for stable flow in capillaries,  $\mu\dot{\gamma}/\tau_L = 1.2$ . In a purely analytical study [48] of a constitutive law which combines the Maxwell fluid model and a compressible plasticity model we have shown that the shear band orientation as

determined by the method of characteristics is independent of pressure and consistent with the values observed experimentally. (See Appendix)

## 9. RHEOLOGICAL MODELS

In previous work [3] the authors showed from experimental measurements that the Maxwell Model, which sums elastic and viscous strain components, correctly describes the transient liquid response under pressure. The simplest incompressible form of the Maxwell model requires two rheological properties - for example: the limiting elastic shear modulus,  $G$ , and the limiting low shear viscosity,  $\mu$ .

A full rheological model for elastohydrodynamic lubrication was developed from observations of the liquid lubricant response observed in high-pressure rheometers. Here,  $d_{ij}$  is the rate of deformation tensor,  $\tau_{ij}$  is the deviatoric stress tensor and  $\tau_e$  is the von Mises stress. In formulating this equation we adopted the Stokes' Condition - the mean mechanical pressure,  $p$ , being set equal to the thermodynamic pressure,  $p_T$ . However, in writing the full model in Ref [3] we also set the second coefficient of viscosity equal to zero and this is inconsistent with Stokes' Condition. We suggest tentatively that a term be added to the right-hand side of the equation so that the full model now reads

$$d_{ij} = \frac{d}{dt} \left[ \frac{\tau_{ij}}{2G} - \delta_{ij} \frac{p}{3K} \right] + \frac{\tau_{ij}}{2\mu} F(T, p, \tau_e) \quad (23)$$

$$+ \frac{\delta_{ij}}{2\mu} (p_T - p)$$

where  $K$  is now the bulk modulus of the glass and  $p_T$  is that pressure which yields the instantaneous density of the liquid when used in the equilibrium equation of state. Stoke's Condition is now abandoned and compressional viscoelasticity is addressed explicitly. The second coefficient of viscosity is zero which sets the bulk viscosity equal to  $2/3\mu$ . This choice is made so that the short time isothermal compressibility is  $1/K$  and the long time compressibility is obtained from the state equation. The function  $F(T,p, \tau_e)$  is an empirical rate relation.

Equation (23) represents unfinished business in two respects. A first normal stress difference is not explicitly introduced. The use of the Jaumann time derivative in (23) will result in  $N_1/\tau$  of the order of  $\tau/G$  if  $F \equiv 1$  [49]. Thus the magnitude of shear stress,  $\tau$ , must be close to that of the shear modulus,  $G$ , to yield the first normal stress difference required by the Mohr-Coulomb theory and observed shear band angles. This is too great a value of  $\tau$  since  $\tau_L/G$  is approximately  $1/30$ . Secondly, we now know that the non-linear (in  $\tau_e$ ) form of  $F(T,p, \tau_e)$  is at least in part due to shear localization. Constitutive behavior, by definition, excludes the effect of localization. For many simple, low molecular weight base stocks it may be most correct to set  $F \equiv 1$  and apply a slip criterion such as Mohr-Coulomb. Then the non-linear behavior which was introduced previously through  $F$  is a consequence of the distribution of  $\eta$  through the material and the slip velocity.

For simple cases where the flow is steady simple shear, an empirical stress equation such as we have advanced

$$\tau = \tau_L (1 - e^{-\mu\dot{\gamma}/\tau_L}) \quad (24)$$

is sufficient. Here the rate sensitivity coefficient,  $m$ , goes to zero as  $\mu\dot{\gamma}/\tau_L$  becomes large. For solid polymers where shear bands are operating,  $m$  is small but not zero. Also, recent

measurements [32] indicate that the transition from Newtonian to “rate-independent” behavior for high molecular weight lubricants is broader in shear rate than that which is described by equation (24). These deficiencies may be removed by using the Carreau-Yasuda form introduced previously

$$\tau = \mu \dot{\gamma} \left[ 1 + \left( \frac{\mu \dot{\gamma}}{\tau_L} \right)^a \right]^{-(m-1)/a} \quad (11)$$

The dimensionless exponent,  $a$ , controls the breadth of the transition and rate sensitivity coefficient,  $m$ , appears explicitly. Note that equation (11) is equivalent to the Elsharkawy and Hamrock [50] model when  $m = 0$ . For  $m$  very small ( $\sim 0.01$ ) but not zero, equation (11) fits experimental results well while removing the singularity which causes problems in numerical simulations.

## 10. MECHANICAL SHEAR BANDS IN NON-VISCOMETRIC FLOW

### 10.1 Shear Bands in Wedge Flow

Visualization of shear bands has to date been accomplished between parallel plates. The interpretation of the flow field and stress state leading up to localization is the least ambiguous for plane Couette shear. This is not however the general case for lubrication flows. To investigate the generation of shear bands in wedge flow we fabricated a new stationary shaft for the High-Pressure Flow Visualization Cell. The stationary surface (the lower surface of Figure 22) was ground at an angle of  $5^\circ$  with the direction of motion of the moving (upper of Figure 22) surface.



5P4E. 138 MPa, 5°C

**Figure 22. Mechanical Shear Bands between Converging Plates with Sliding. Lower Tilted Surface is Stationary.**

Observation of birefringence during shear through crossed polarizers clearly showed a stress gradient across the film as expected. Shear bands appeared as shown in Figure 22 for 5P4E. These bands are similar to those observed between parallel plates. However, the analysis of the previous section can not be applied because of the non-uniform stress field in the film.

## **10.2 Extra-High-Pressure Flow Visualization Cell**

The simple plane shear configuration is preferable for the interpretation of flow visualization. However, the pressure capability is limited by the friction of shaft seals. A new Extra-High-Pressure Flow Visualization Cell is shown in section view in Figure 23. Two windows are provided - one for illumination as shown and one for viewing. The entire liquid sample is compressed by the motion of the piston and rod to generate the ambient pressure of up to 1 GPa. A hydraulic actuator pushes against the rod. Pressure measurement is obtained from the force on the rod and a simple hysteresis calibration of seal friction. A pin (1.2 mm diameter) is attached to the piston so that after some compression of the liquid, a squeeze film is formed between the pin and the anvil. The ambient pressure just before squeeze can only be adjusted by varying the initial liquid volume. The illumination window is tilted so that due to refraction light will approach the gap between the pin and anvil at a glancing angle.

## **10.3 Shear Band Observations in Squeeze Film**

When a mineral oil (N1 from [18, 37]) is pressurized to 1.0 GPa at room temperature and then squeezed between the pin and anvil, shear bands develop near the edge of the gap as shown at the top of Figure 24. The dashed white lines complete the outlines of the pin and the anvil

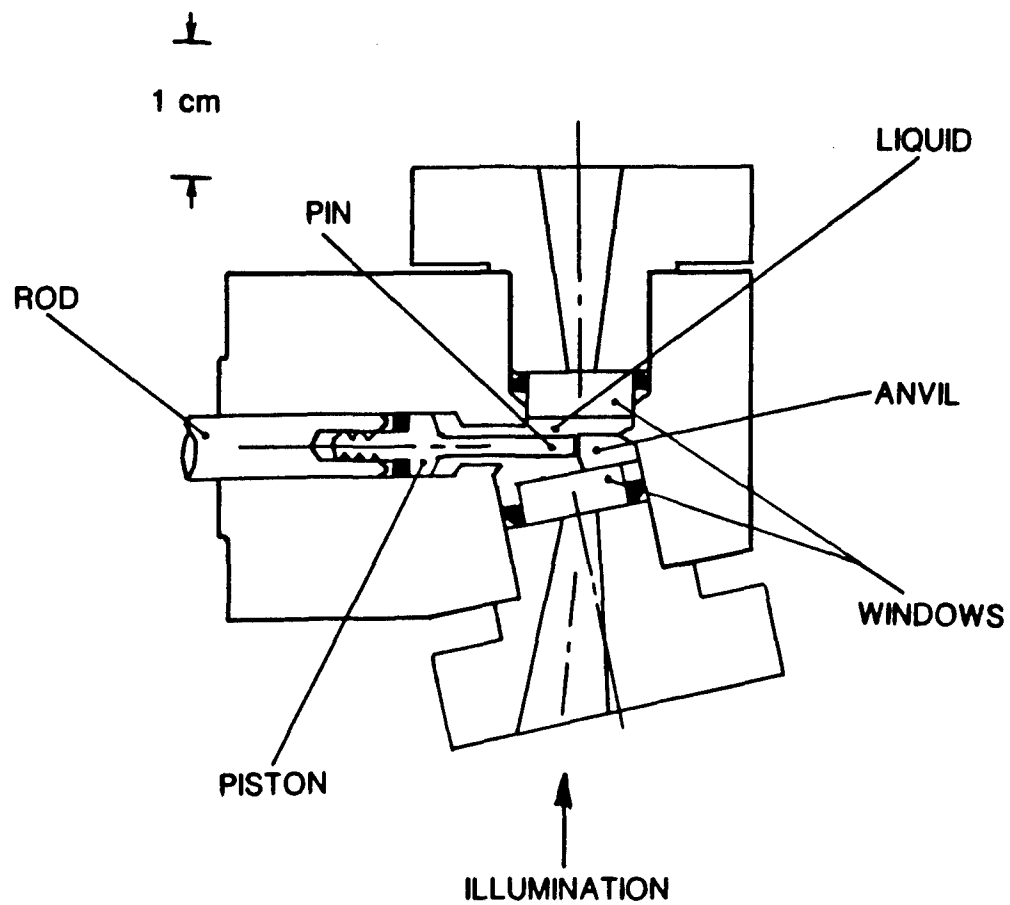


Figure 23. Extra-High-Pressure Flow Visualization Cell.

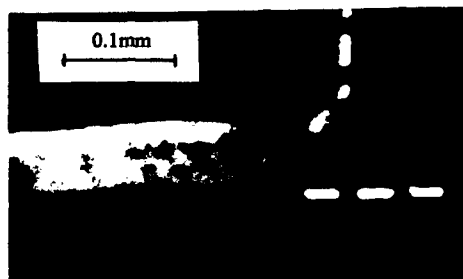
below the pin. The axis of the pin is vertical and to the left in the upper picture. For comparison, shear bands in solid polymethylmethacrylate sectioned from a specimen deformed in plane-strain compression are shown in the bottom of Figure 24 (taken from [24]). The similarity in appearance and orientation is striking. The glass transition pressure at room temperature is 0.6 GPa for N1 so the comments of Section 4 regarding hydrostatic pressure apply. The reason that the bands are not at  $90^\circ$  to one another (as are the principal shear directions) for both the N1 and the polymer has been attributed [24] to dilatation or the pressure dependence of yield stress. The slip planes are turned in a direction of reduced compressive normal stress for which slip is more favorable. Shear bands were also observed in HVI 650 at 0.8 GPa in the present device. These results are relevant to squeeze film lubrication and plate impact and diamond anvil experiments.

## **11. ADIABATIC SHEAR BANDS**

In previous sections we have discussed mechanical shear bands. A very different type of shear localization is the subject of this section. We present the experimental observation and numerical simulation of a thermally driven localization similar to the “adiabatic shear bands” found during high rate deformation of metals [51]. We have adopted the term “adiabatic” from the usage in plasticity literature, although the term is not strictly correct.

### **11.1 Background**

In 1967, Plint [52] recognized that the inhomogeneous shear in an elastohydrodynamic film which exists due to viscous heating might localize at or near the mid-plane where the



MINERAL OIL in 1GPa Ambient



PMMA POLYMER in 1atm Ambient

**Figure 24. Shear Bands in Mineral Oil Squeezed between Pin and Anvil (Top) and Shear Bands in Solid Polymer in Compression (Bottom from [24]).**

temperature is greatest. If the shear stress,  $\tau$ , is uniform across the film, the viscous dissipation will be approximately exponential with temperature. The lubricating film is generally a poor thermal conductor. Therefore, as the temperature,  $T$ , rises locally the dissipation which generates the temperature field rises rapidly with the local rate of shear,  $\dot{\gamma}$ , and conditions favor an unstable temperature profile.

The parameter which characterizes the thermal behavior of liquid films in plane Couette shear is the dimensionless Brinkman number (also known as Griffith or Nahme number)

$$B_r = \frac{\beta \tau^2 h^2}{\mu_0 k} \quad (25)$$

where  $h$  is the thickness of the film,  $\mu_0$  is the initial viscosity at  $T = T_0$ ,  $k$  is the thermal conductivity of the liquid and  $\beta$  is the temperature-viscosity coefficient.

It has been long recognized in the rheology literature that a low value of  $B_r$  is a necessary condition to avoid the influence of viscous heating in continuous shear viscosity measurement [53]. However, the significance of the Brinkman number is not well recognized in tribology. The Brinkman number appears as the coefficient of the dissipation term in the dimensionless energy equations [12, 45]. A steady state solution to the energy equation exists for  $B_r < 3.51$  when the temperature-viscosity function is exponential and for  $B_r < \pi^2$  when the viscosity varies linearly with temperature [31]. Experimental investigations of lubricant constitutive behavior for EHD conditions which may be regarded as isothermal are performed at  $B_r < .3$  in high pressure rheometers [30, 32] and disc machines [36]. Thermal localization phenomenon are expected to manifest at large ( $> 3.51$ ) values of  $B_r$ .

## 11.2 Experiment

The High-Pressure Flow Visualization Cell has been described in detail elsewhere [4]. This device is shown schematically in Figure 25. The liquid lubricant sample is sheared in the gap between a flat on a moving shaft and the end of a stationary shaft. The gap is illuminated and viewed in a direction perpendicular to the direction of motion and parallel to the plane of the bounding surfaces. The moving shaft is pushed/pulled by a gas actuated piston and this shaft must pass through high-pressure closure seals. Motion is not continuous reciprocation, but unidirectional for a given run.

For a shear rheological measurement during which rheological properties vary with time, one would choose to design the experiment following one of two idealizations [45]: 1. rate (of strain) control where the relative velocity is kept constant, or 2. force (stress) control where the average shear stress is imposed as constant. Whereas, it is known that rate control will not yield thermal runaway [45], we intend to show that in a stress-controlled experiment localization can indeed take place. The device shown (a constant actuating gas pressure applied to the piston) would be ideal for force controlled experiments; however, there exists some friction in the high-pressure seals, which is known to have a viscous component.

The liquid lubricant chosen for this study is the five-ring polyphenyl ether, 5P4E for which there is probably the most high pressure property data available. The thermal properties,  $k=0.15$  W/m°C and  $\rho C=1.85$  MJ/m<sup>3</sup> °C, of Richmond, et al. [54] and the rheological properties of Yasutomi, et al. [18] were used. Refractive index was measured in a high pressure refractometer described by Bair [13]. In addition, the properties of this material have a great sensitivity to

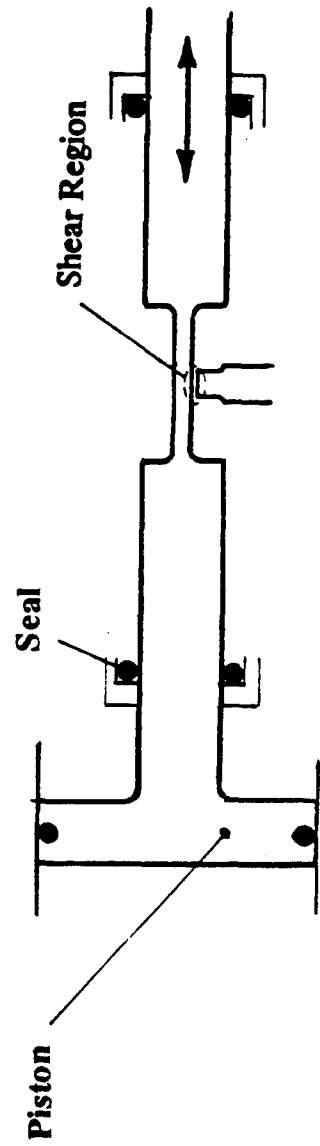
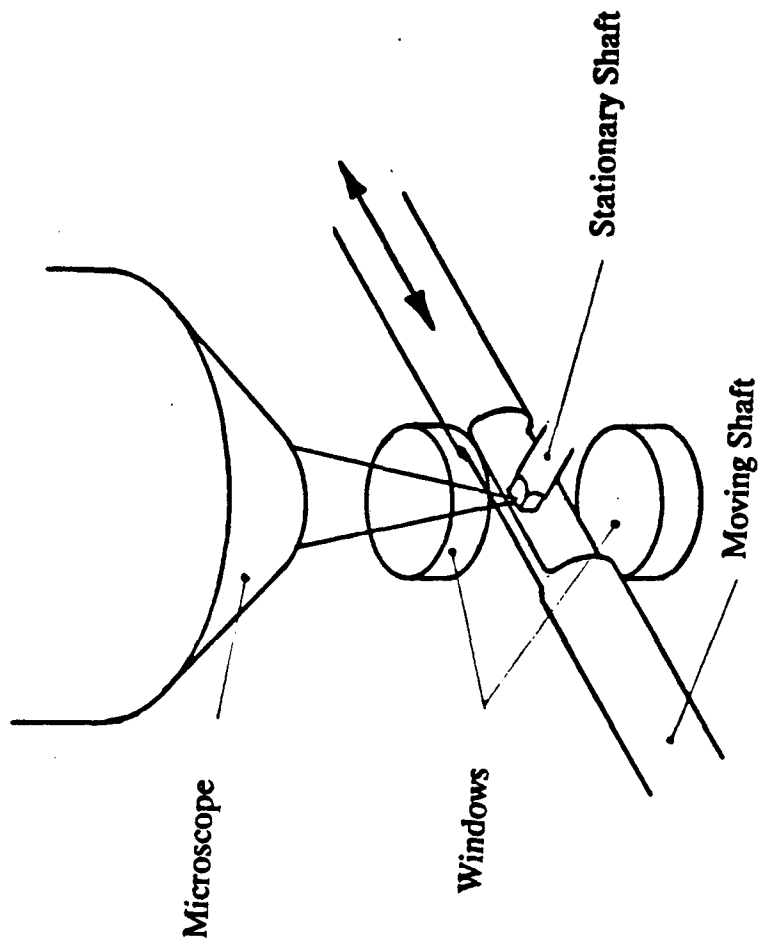


Figure 25. Flow Visualization Configuration. (Illumination Through Lower Window.)

pressure so that, at relatively low pressure, behavior is observed which is representative of many materials at much greater pressure.

Regulated compressed nitrogen gas was applied to the left side of the piston in Figure 25 with sufficient pressure (3 MPa) to develop an initial velocity of 0.75 mm/s. The sample pressure was 172 MPa and the initial temperature 22°C yielding a viscosity  $\mu_0 = 3 \text{ MPa}\cdot\text{s}$  and  $\beta = 0.6^\circ\text{C}^{-1}$ . Although the piston force was constant, the force contributed by the seals increased with sliding velocity so that the average stress applied at the shearing gap decreased with velocity (and time). A standard (30 frames/second) video camera recorded the video prints shown in time sequence in Figure 26. The lower black object is the stationary boundary and the upper is the moving (left to right) boundary. The gap or clearance is  $150 \mu\text{m}$ , and  $\tau$  is obtained from the product of initial viscosity and the initial rate of shear, to give  $B_r = 6.75$ . The central one-third of the length (in the flow direction) is captured in each print.

The velocity history is shown by the points in Figure 27 - obtained by differentiating the signal from an LVDT on the moving shaft. Past 210 ms the velocity exceeded the measurement capability.

A striking feature in the sequence of images in Figure 26 is the abrupt appearance of a dark band within the liquid film at 260 ms. In the previous frame at 230 ms the band is absent. However the interior of the film has begun to darken. In less than 30 ms a dark band has appeared. This feature faded and disappeared within 10s after the interruption of shear. We show in the next section that the dark band is consistent with the appearance of a hot liquid layer surrounded by cooler liquid. Light transmitted through the film should be refracted from a hot region to cool regions. Effectively, two cool, viscous liquid films are sliding against a hot low



TIME

230 ms



260 ms



330 ms

5P4E, 22°C INITIAL TEMP, 172 MPa

Figure 26. Visualization of an Adiabatic Shear Band. Time is Elapsed from Start of Shear.

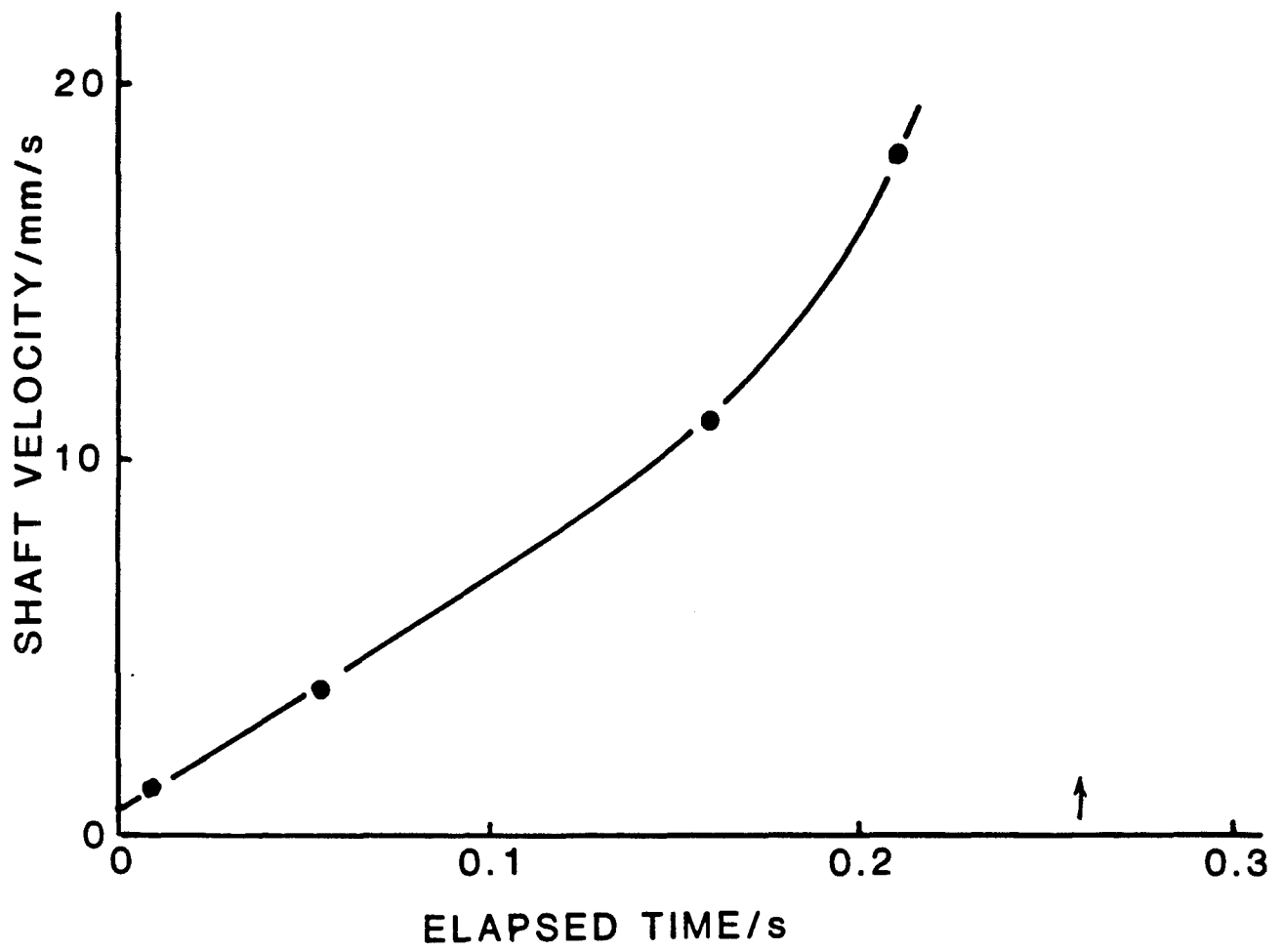


Figure 27. Velocity History.

viscosity film. The curvature of the band is apparently due to cool liquid being drawn into the shear gap by the moving shaft at the upper left of the prints in Figure 26. That the band which suddenly appears represents shear localization will be shown by the analysis which follows.

### 11.3 Thermal Analysis of Plane Couette Shear Under Stress-Controlled Conditions

The statement of the conservation of energy translates into the following commonly known as the energy equation

$$\rho c_p \frac{DT}{Dt} = (kT_{,j})_j + \phi, \quad (26)$$

where the left member of the above equation represents the energy transport by convection with  $D/Dt$  representing the material derivative and  $\rho c_p$ , the volume heat capacity. The first term on the right denotes the energy transfer by conduction followed by the viscous dissipation term which is  $\phi = \tau \dot{\gamma}$ .

For the geometry under consideration, the energy equation reduces to

$$\rho c_p \frac{\partial T}{\partial t} = k \frac{\partial^2 T}{\partial y^2} + \phi, \quad (27)$$

where  $y$  is the coordinate normal to the direction of motion in the direction of the film thickness.

If the Newtonian assumption is adopted, the viscous dissipation term becomes  $\phi = \frac{\tau^2}{\mu}$ ,

where the viscosity,  $\mu$ , varies exponentially with temperature (for small  $T - T_0$ ) prescribed as

$$\mu = \mu_0 e^{-\beta(T-T_0)}. \quad (28)$$

The dimensionless form of the equation (27) for a stress-controlled experiment takes on the form given below

$$\frac{1}{F_o} \frac{\partial \bar{T}}{\partial \bar{t}} = \frac{\partial^2 \bar{T}}{\partial \bar{y}^2} + B_r e^{\bar{T}}, \quad (29)$$

where  $F_o$  is the dimensionless Fourier number defined as

$$F_o = \frac{k}{\rho c_p} \frac{t_{ob}}{h^2}$$

and

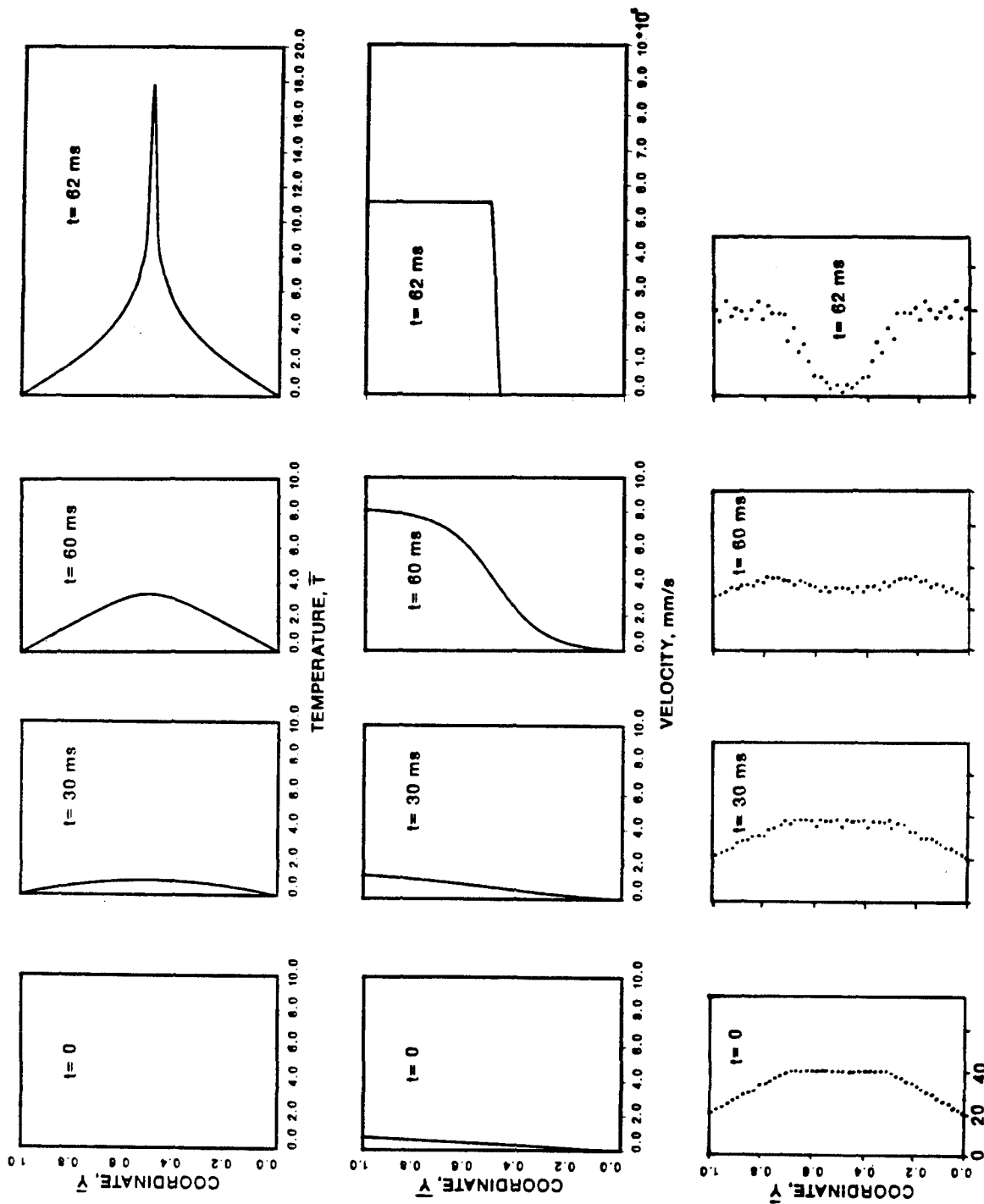
$$\bar{T} = (T - T_o)\beta, \quad \bar{t} = \frac{t}{t_{ob}}, \quad \bar{y} = \frac{y}{h}.$$

In defining the Fourier number above, the parameter  $t_{ob}$  represents an observation time.

Equation (29) was treated numerically using a marching technique by Dr. Michael Khonsari at University of Pittsburgh. The initial and boundary conditions are maintained at  $\bar{T} = 0$ . The time history of the temperature distribution across the film is presented in Figure 28 for  $B_r = 6.75$ . As shown, temperature rapidly rises in the center of the film at about 0.06s and becomes unbounded when  $t > 0.062s$ . The existence of hot center temperature surrounded by cooler liquid is indicative of the onset of localization. This is also apparent in the velocity profile at  $t = 0.062s$  shown in Figure 28.

#### 11.4 Optical Ray Tracing

It seems reasonable that the last temperature profile of Figure 28 would result in the appearance of a dark band at the midplane. However, a calculation is in order, to show that the dark band accompanies localization and that the band will not appear earlier. The previous thermal analysis yielded temperatures at fifty equally spaced grid points within the liquid film. We assume that the temperature is uniform within strata centered at these points. Sources of light are



RELATIVE LIGHT TRANSMISSION (COUNTS PER GRID POINT)

Figure 28. Analytical Results.

placed at each grid point across the film at one edge of the liquid film where illumination enters. Forty rays originate from each source, equally distributed over an angular interval of  $\pm 0.05$  radian from the centerline of the stratum. Where a ray intersects the boundary between strata, Snell's Law is applied. Contact with a solid boundary surface absorbs a ray.

The refractive index,  $n_0$ , of the liquid at the test pressure and initial temperature,  $T_0$ , was measured in a high-pressure refractometer. The Lorenz-Lorentz equation can be manipulated to yield an expression for the refractive index,  $n$ , at other temperatures through the liquid density,  $\rho$ . The Lorenz-Lorentz equation [55] reads

$$\frac{n^2 - 1}{n^2 + 2} \cdot \frac{1}{\rho} = \text{constant} \quad (15)$$

The thermal expansivity of the liquid lubricant was supplied by the manufacturer and corrected for elevated pressure from the results of Yasutomi, et al. [18].

The number of rays exiting the film gap within a stratum is considered a measure of the relative light transmission at the grid point associated with that stratum. These values are plotted in Figure 28. It is clear that the dark band for which there is relatively little light transmission is not present at 60 ms but is fully developed at 62 ms and although it is a direct consequence of the temperature profile the band is associated with the extreme localization of shear as indicated by the velocity profile of Figure 28.

## 11.5 Discussion

Clearly, the dark band observed in the flow visualization experiment is due to a thin hot layer of liquid sandwiched between two cooler layers. This hot layer represents a region where the shear deformation is localized. The greatest part of the relative velocity is accommodated

with a small fraction (~5%) of the film thickness. Notably, the localization occurs at shorter times than observed in experiments. We believe that this is due in most part to the inability of the experimental technique to achieve true stress control stemming from viscous seal friction which increases with sliding velocity and decreases with time of sliding or temperature.

The one-dimensional analysis presented here forces symmetry about the center of the film. The experimental geometry is finite in length in the flow direction with an inlet to the left in Figure 26. The adiabatic shear band near the entrance is therefore displaced toward the hotter stationary boundary at the bottom of each print in Figure 26 by the cooler liquid convected into the gap by the upper moving boundary. This accounts for the curvature of the band pictured in Figure 26.

Lubricant resident times in EHD are typically about 1 ms or much less. In this simulation, localization occurs at longer times - on the order of 100 ms. However, in the dimensionless energy equation (30), time is scaled by  $h^2\rho C_p/k$ . The film thickness,  $h$ , is at least 100 times thinner for a lubricated contact. Hence, the localization time would be of the order of 10  $\mu$ s which is in the realm of EHD.

## 12. OBSERVATIONS IN AN OPERATING EHD CONTACT

If light is scattered by reflection from a mechanical shear band, there should be a preferred scattering direction within the lubricant film which depends upon the direction of shear. The orientation of the second type of band is little changed by the direction of shear and we would expect that the way in which light interacts with this type should be little affected by the shear direction. In the following discussion, then, only the first type of mechanical shear band is considered.

An optical EHD simulator was employed in this work and is described in Ref [13]. The contact consisted of a 25.4 mm radius sapphire disc running over a 7.6 mm radius steel roller. The roller had a crown radius to give the contact an ellipticity of 3. The disc was loaded by an 89 N weight giving a contact size of 672 x 224  $\mu\text{m}$  and an average pressure of 760 MPa. The polyphenyl ether, 5P4E, was used as a lubricant giving a minimum film thickness of approximately 1.5 $\mu\text{m}$  at room temperature.

The original idea was to illuminate the contact with a laser from directly above, through a piece of card with a hole in it, and observe the pattern reflected onto the underside of the card. It was hoped that light would be reflected from the shear bands, expected to be inclined at about 19° to the horizontal, producing a pattern which changed sides when the shearing direction was reversed. This was not observed. Further examination of the optics of the system reveals why. It transpires that any light which may have been reflected from the shear bands regardless of the direction of shear will strike the upper surface of the disc at an incident angle greater than the critical one for that interface, so the light will be totally internally reflected, and could only escape from the disc edges. The refractive index of sapphire is 1.766. The refractive index of the lubricant was measured with a high-pressure refractometer at pressures to 300 MPa and extrapolated to 760 MPa. The value obtained is 1.722.

A solution to this problem is to illuminate the contact from an angle (Figure 29). An incident angle of about 34° will be refracted so as to strike a shear band produced by negative sliding velocity approximately normally, and hence be reflected back into the laser. Consequently an angle slightly different was used during the experiments. It was hoped that this would allow the observation of light reflected back toward the source in one direction of shearing as illustrated

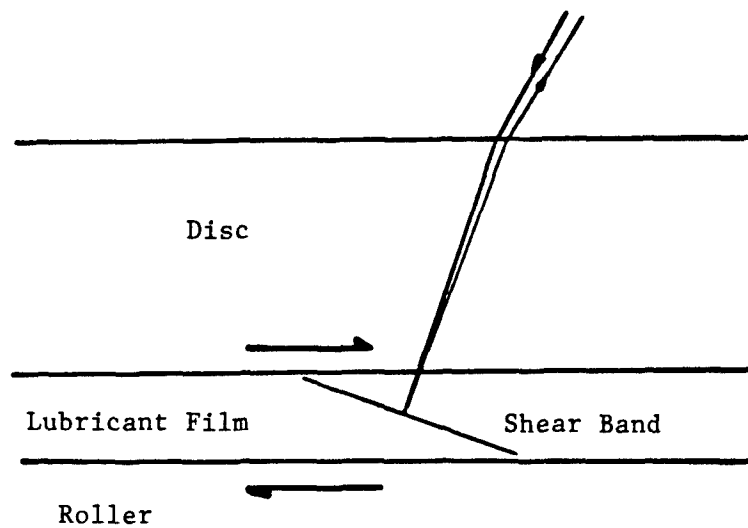


**Figure 29.** Schematic of light path striking a shear band with negative sliding velocity.

in Figure 29. Unfortunately, any light that may have been reflected was either too diffuse or coincided with a different brighter reflection. However, it was noticed that the intensity of light escaping from the edge of the disc (see Fig. 30) varied with the direction of rotation and hence shearing. See Table 5. tests A through D. This effect could be caused by shear bands, as explained above or may have been due to reflections from the inlet or outlet regions of the film, as the laser has a  $480\mu\text{m}$  diameter beam some light will strike in front of and behind the contact patch. The inlet meniscus is far enough away to be of no concern. However, the outlet region is much closer to the contact patch. The lubricant film cavitates just beyond the contact and most of the film is thought to adhere to the surfaces. If this is the case it will have little effect on the direction of reflected light.

To illustrate that this is the case, the slide-to-roll ratio was set negative. That is, rotation in the same direction as before results in shear in the opposite one hence changing the inclination of the shear band. The higher intensity light was now observed in the opposite direction of rotation to before (i.e. with the outlet meniscus on the opposite side of the contact). See test F - Table 5. The slide-to-roll ratio was also set to zero and no change in intensity was observed when the direction of rotation was reversed (test E). In order to quantify this change in intensity a photovoltaic cell was masked, so that only light from the disc could enter, and placed near the disc edge. The output from the photovoltaic cell is only an indication of the relative intensity for rotation in opposite directions for each absolute value of slide-to-roll ratio, because it proved to be very sensitive to ambient lighting conditions and proximity to the disc edge, which unfortunately changed each time the absolute value of slide-to-roll ratio was changed. The results

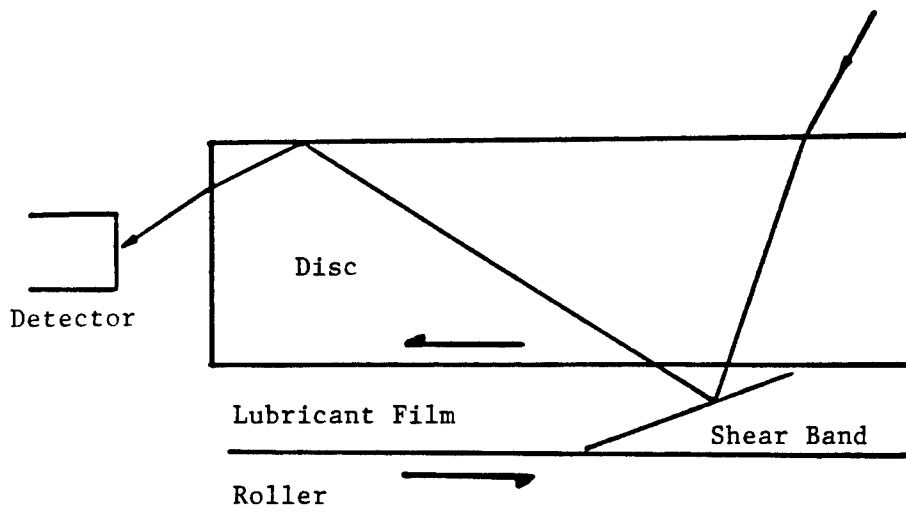


**Figure 30. Schematic of light path striking a shear band with positive sliding velocity.**

are listed in Table 5 where light intensity at the edge of the sapphire disc is represented by the photovoltaic output in mV.

These results show that the change in observed intensity is not dependent on the direction of rotation (i.e. meniscus position) but on the direction of shearing. The fact that the intensity change can be seen for both directions of rotation helps to eliminate the possibility that the phenomena may be caused by the geometry of the contact changing, or the position and shape of the inlet and outlet regions changing as the direction is reversed. While this does not conclusively prove that mechanical shear bands exist in operating contacts (change in birefringence of sapphire with stress is a possible effect), it does show that there is some mechanism at work within the lubricant which is dependent on the direction of shearing and effects the optical character of the lubricant film.

**Table 5. Light Intensities for Various Contact Positions**

<b>Test</b>	<b>Rolling Velocity (m/s)</b>	<b>Sliding Velocity (m/s)</b>	<b>Slide-to Roll Ratio</b>	<b>Intensity of Light at Disc Edge (mV)</b>	<b>Change in Intensity (mV)</b>
A	0.228	0.022	0.096	51	-8
	-0.228	-0.022	0.096	43	
B	0.233	0.013	0.056	48	-13
	-0.233	-0.013	0.056	35	
C	0.235	0.008	0.034	54	-17
	-0.235	-0.008	0.034	37	
D	0.237	0.005	0.021	40	-1
	-0.237	-0.005	0.021	39	
E	0.239	0.000	0.000	47	0
	-0.239	0.000	0.000	47	
F	0.245	-0.012	-0.049	52	+7
	-0.245	0.012	-0.049	59	

## REFERENCES

1. J.F. Dill, P.W. Drake and T.A. Litovitz, "The Study of Viscoelastic Properties of Lubricants Using High-Pressure Optical Techniques," ASLE Trans., 18, 3, (1975) 202-210.
2. A.J. Barlow, G. Harrison, J.B. Irving, M.G. Kim, J. Lamb and W.C. Pursley, "The Effect of Pressure on the Viscoelastic Properties of Liquids," Proc. Roy. Soc. London A. 327, (1972) 403-412.
3. S. Bair and W.O. Winer, "The High-Pressure, High-Shear Stress Rheology of Liquid Lubricants," Trans. ASME, J. of Tribology, 114, 1, (1992) 1-13.
4. S. Bair, F. Qureshi and W.O. Winer, "Observations of Shear Localization in Liquid Lubricants Under Pressure," Trans. ASME, J. of Tribology, 115, 3, (1993) 507-514.
5. A. Eastwood and G. Harrison, "Non-Newtonian Viscosity at High Stresses," Proc. VIII Intern. Congress Rheology, (1980) 199.
6. S. Clyens, C.R. Evans and K.L. Johnson, "Measurement of the Viscosity of Supercooled Liquids at High Shear Rates with a Hopkinson Bar," Proc. R. Soc. Lond. A381, (1982) 195-214.
7. J. Jakobsen and W.O. Winer, "High Shear Stress Behavior of Some Representative Lubricants," Trans. ASME, JOLT 97, 3, (1975) 479-484.
8. J.D. Novak and W.O. Winer, "Some Measurements High Pressure Lubricant Rheology," Trans. ASME, JOLT 90, 3 (1968) 580-591.
9. R.B. Bird, R.C. Armstrong and O. Hassager, Dynamics of Polymeric Liquids, Vol. 1, John Wiley & Sons (1987).
10. J.K. Appeldoorn, E.H. Okrent and W. Phillippoff, "Viscosity and Elasticity at High Pressures and High Shear Rates," Proc. Am. Pet. Int. 42, III, (1962) 169.
11. W. Phillippoff, "Viscoelasticity of Polymer Solutions at High Pressures and Ultrasonic Frequencies," J. Appl. Phys. 34, 5, (1963) 1509.
12. H.H. Winter, "Viscous Dissipation in Flowing Molten Polymers," Advances in Heat Transfer, 13, (1977) 2.17.
13. S. Bair, "An Experimental Verification of the Reciprocal Asymptotic Isoviscous Pressure," STLE, Trib. Trans. 36, 2, (1993) 154-155.

14. P.W. Bridgman, "Viscosities to 30,000 kg/cm<sup>2</sup>," Proc. Am. Acad. Arts Sci., 77, (1949) 117-128.
15. J.D. Barnett and C.D. Bosco, "Viscosity Measurements on Liquids to Pressures of 60 kbar," J. Appl. Phys., 40, 8, (1969) 3148.
16. H.E. King, E. Herbolzheimer and R.L. Cook, "The Diamond-anvil Cell as a High-Pressure Viscometer," J. Appl. Phys., 71, 5, (1992) 2078-2080.
17. H.S. Hsiao, S.K. Sharma and B.J. Hamrock, "Pressure-Temperature-Viscosity and EHD Characteristics of Two Perfluoropolyalkylether Fluids," SAE SP-936, (1992) 237-239.
18. S. Yasutomi, S. Bair, S. and W.O. Winer, "An Application of a Free Volume Model to Lubricant Rheology," Trans. ASME, Journal of Tribology, 106, 2, (1984) 304-312.
19. D.R. Wilson, "Exploratory Development on Advanced Fluids and Lubricants in Extreme Environments by Mechanical Characterization," Tech Rpt. Wright-Patterson AFB, AFML-TR-70-32 III, (1972) 101.
20. P. Bezot, C. Hesse-Bezot, D. Berthe, G. Dalmaz and P. Vergne, "Viscoelastic Parameters of 5P4E as a Function of Pressure and Temperature by Light Scattering Technique," Trans. ASME Journal of Lubrication Technology, 108, 4, (1986) 579-583.
21. J.F. Hutton, "Re-assessment of Rheological Properties of LVI 260," Trans. ASME, Journal of Lubrication Technology, 106, (1985) 537.
22. K.T. Ramesh and R.J. Clifton, "Finite Deformation Analysis of Pressure-Shear Plate Impact Experiments on an Elastohydrodynamic Lubricant," Trans. ASME J. Appl. Mech., 59, (1992) 754-761.
23. S. Bair and W.O. Winer, "A Rheological Basis for Concentrated Contact Friction," Proc. Leeds-Lyon Symp. (1993).
24. P.B. Bowden, "The Yield Behavior of Glassy Polymers," The Physics of Glassy Polymers, R. N. Haward, Ed., John Wiley & Sons, (1973) 279-339.
25. P.W. Bridgman, The Physics of High Pressure, Dover, N.Y. (1970).
26. C.W. Burham, J.R. Holloway and N.F. Davis, "Thermodynamic Properties of Water to 1,000°C and 10,000 Bar," Geo. Soc. of Amer. Special Paper No. 132 (1969).
27. B.J. Hamrock, B.O. Jacobson and S. Bergstrom, "Measurement of the Density of Base Fluids at Pressures to 2.2 GPa," ASLE Trans. 30, 2, (1987) 196-202.
28. K.T. Ramesh, "The Short-Time Compressibility of EHD Lubricants," ASME Journal of

- Tribology, 113, (1991) 361-371.
29. A. Dyson, *Interdisciplinary Approach to Liquid Lubricant Technology*, Ed. by P. M. Ku, NASA, (1972) 303.
  30. S. Bair and W.O. Winer, "The High Shear Stress Rheology of Liquid Lubricants at Pressures of 2 to 200 MPa," *ASME J. of Tribology*, 112, 2, (1990) 246-252.
  31. H.H. Winter, "The Unsteady Temperature Field in Plane Couette Flow," *Int. J. Heat Mass Transfer*, 14, (1971) 1203-1212.
  32. S. Bair and W.O. Winer, "A New High-Pressure, High-Shear Stress Viscometer and Results for Lubricants," *Trib. Trans.* 36, 3 (1993).
  33. E.O. Doebelin, *Measurement Systems: Application and Design*, McGraw-Hill, New York (1966).
  34. S. Bair, "The High-Pressure Rheology of a Soap-Thickened Grease," *STLE Trib. Trans.* 93-TC-4D-1 (1993).
  35. P. Bezot, C. Hesse-Bezot, G. Dalmaz, P. Taravel, P. Vergne and D. Berthe, "A Study of Traction in EHL: Experimental and Simulated Curves for a Silicone Fluid," *Wear* 123, (1988) 13-31.
  36. C.R. Evans and K.L. Johnson, "The Rheological Properties of EHD Lubricants," *Proc. Instn. Mech. Engrs.* 200, No. C5 (1986).
  37. S. Bair and W.O. Winer, "Some Observations in High-Pressure Rheology of Lubricants," *ASME Journal of Lubrication Technology*, 104, 3, (1982) 382-386.
  38. M. Muraki, "Molecular Structure of Synthetic Hydrocarbon Oils and Their Rheological Properties Governing Traction Characteristics," *Trib. International* 20, 6, (1987) 352.
  39. P.L. Wong, S. Lingard and A. Cameron, "The High Pressure Impact Microviscometer," *STLE Trib. Trans.* 35, 3, (1992) 500-508.
  40. C.R. Evans, "Measurement and Mapping of the Rheological Properties of EHD Lubricants," *Ph.D. Thesis*, Cambridge (1983).
  41. S. Bair, W. O. Winer, and K. W. Distin, "Experimental Investigations into Shear Localization in Operating Concentrated Contact," *Proc. 19th Leeds-Lyon Symposium* (1992).
  42. John Harris, *Rheology and Non-Newtonian Flow*, Longman Group, London, (1973), 63-34.

43. H. Janeschitz-Kriegl, *Polymer Melt Rheology and Flow Birefringence*, Springer, Verlag, Berlin (1984) 118.
44. C. G'Sell, "Plastic Deformation of Glassy Polymers: Constitutive Equations and Macromolecular Mechanisms," in *Strength of Metals and Alloys*, Pergamon Press, Oxford (1986) 1955.
45. R. I. Tanner, *Engineering Rheology*, Clarendon Press, Oxford, (1985) 237.
46. W. Gleissle, "Stresses in Polymer Melts at the Beginning of Flow Instabilities in Cylindrical Capillaries," *Rheol. Acta* 21, (1982) 484-487.
47. S. I. Abdel-Khalik, O. Hassager and R. B. Bird, "Prediction of Melt Elasticity from Viscosity Data," *Poly. Engr. Sci.* 14, 12, (1974) 861.
48. Y. K. Lee, J. Ghosh, S. Bair and W. O. Winer, "Shear Band Analysis for Lubricants Based on a Viscoelastic Plasticity Model," *Appl. Mech. Rev.* 47, Part 2 (1994) 5209-5220.
49. J. F. Hutton, "Theory of Rheology," *Interdisciplinary Approach to Liquid Lubricant Technology*, Edited by P. M. Ku, NASA, (1972), 206-207.
50. A. A. Elsharkawy and B. J. Hamrock, "Subsurface Stresses in Micro-EHL Line Contacts," *Trans. ASME, Journal of Tribology*, 113, 3, (1991) 647.
51. Y. Bai and B. Dodd, *Adiabatic Shear Localization*, Pergamon Press Oxford (1992) 1.
52. M. A. Plint, "Traction in Elastohydrodynamic Contacts," *Proc. Instn. Mech. Entrs.*, 182, Pt. 1, No. 14 (1967).
53. K. Walters, *Rheometry*, John Wiley & Sons, New York, (1975) 80-81.
54. J. Richmond, O. Nilsson, and O. Sandberg, "Thermal Properties of Some Lubricants under Pressure," *J. Appl. Phys.*, 56, 7 (1984) 2066-2067.
55. T. C. Poulter, C. Ritchey, and C. Benz, "The Effect of Pressure on the Index of Refraction of Paraffin Oil and Glycerine," *Phys. Review*, Vol. 41 (1932) 366-367.

**APPENDIX**

# Shear band analysis for lubricants based on a viscoelastic plasticity model

YK Lee, J Ghosh, S Bair, and WO Winer

*George W Woodruff School of Mechanical Engineering  
Georgia Institute of Technology, Atlanta GA 30332-0405*

Shear banding is an outstanding problem in lubricant rheology where a thin film of lubricant is under high pressure and high shear stress. To study such a phenomenon, a viscoelastic-plastic model is proposed. It is postulated that shear bands appear when the character of the field equations changes from elliptic to hyperbolic. The model is derived based on a rate formulation which combines a Maxwell fluid model and a compressible rate-independent plasticity model. The model gives the constitutive relation of a compressible viscoelastic-plastic fluid for which the assumption of Stokes condition becomes unnecessary. It also accounts for the elastic coupling effect of both the viscous and the rate-independent behavior of a lubricant. It provides a novel feature that the development of shear bands can be tracked rather than being determined after they are fully developed. Hence, the process of shear banding may be articulated. The analysis focuses on identifying necessary and sufficient conditions which, if achieved in a deformation, would produce a change in character of the governing field equations. Through the use of Drucker-Prager criterion as the component that governs the rate-independent behavior of a lubricant, the analysis gives results that are in accord with experimental observations. Parametric results are given graphically.

## CONTENTS

INTRODUCTION .....	S209
VISCOELASTIC PLASTICITY MODEL .....	S210
Additive decomposition .....	S210
Viscoelastic formulation .....	S210
General viscoelastic plastic formulation .....	S211
Example for the flow potential $\phi$ .....	S214
EQUILIBRIUM REQUIREMENT .....	S214
SHEAR BAND ANALYSIS .....	S214
Velocity field equations .....	S214
Characteristic analysis .....	S215
RESULTS AND DISCUSSION .....	S216
Critical values of $\bar{N}$ , $\Gamma^*$ , and $2\mu_{eq}^p$ .....	S216
Orientation of shear bands .....	S217
ACKNOWLEDGEMENT .....	S219
REFERENCES .....	S219

high pressure and shear stress, a lubricant may exhibit a nonlinear stress strain-rate behavior, whereas the same lubricant usually follows a linear Newtonian response below a critical shear stress (Bair and Winer, 1992). The deviation from the linear response marks a characteristic change of the lubricant. It begins to behave like a viscous solid because there exists a limiting value of shear stress at which the response becomes strain-rate independent. Bair and Winer (1992) suggested a nonlinear Maxwell model, with shear modulus taken into the time derivative, which included the effect of pressure on viscous-plastic transition. In a more recent work, Bair et al.(1993) reported the observation of short-lived shear bands in a lubricant. It was observed that the first shear bands appear at the onset of nonlinear behavior marked on a typical stress strain-rate curve. An increase in the shear stress above this point is accompanied with a proliferation of shear bands. The inclination of the shear bands appears to be independent of the pressure and the shear rate. Bair and Winer (1993) also showed that shear band angles can be predicted by using the Mohr-Coulomb criterion. The orientation of shear bands after the localization has occurred could be obtained from the yield trajectory by using a proper planer stress transformation. However, there still exists a need for conditions that could predict the onset of shear banding.

## INTRODUCTION

The search for a general rheological constitutive equation for liquid lubricant at high pressures has been a research focus for some time. It has been observed that under a

In this study, a viscoelastic plasticity model is derived based on a rate formulation which combines a Maxwell fluid model and a compressible plasticity model. The model accounts for the elastic coupling effect of both the viscous and the rate-independent behavior of lubricants. With this model, the necessary and sufficient condition for the onset of shear banding is presented following the standard procedure developed by Lee (1989, 1992), in which shear banding is regarded as a geometric instability, and the onset of such an instability is defined at the instant when the character of the governing field equations ceases to be elliptic.

In what follows, we first provide a framework for the rate formulation of viscoelastic plasticity. This framework can be used to simulate the combined rate-dependent and rate-independent deformation behavior in either liquid or solid polymers while analysis can adopt various approaches to plastic dissipation potential, we choose the Drucker-Prager (1952) criterion to account for the pressure-dependent deformation behavior that a lubricant may exhibit. This criterion is chosen because it is mathematically simple and yet physically plausible for liquid medium which cannot sustain any tension. It must be emphasized that the choice of such a plastic dissipation potential does not restrict in any manner the development of the procedure for shear band analysis. It simply provides a means to include the effects of hydrostatic pressure that is important to the problem at hand. Of course, the ultimate justification of using a specific plastic dissipation potential and its domain of validity depend on the ability of the resulting model to predict experimental observations.

## VISCOELASTIC PLASTICITY MODEL

### Additive decomposition

One of the common assumptions in various inelasticity theories is the decomposition of strain into an elastic and an inelastic part, although details of decomposition may vary from one material to another, depending on the behavior that needs to be emphasized. To describe the flow behavior of lubricants and to account for both rate-dependent and rate-independent behavior at high pressure, we assume that the total rate of deformation tensor  $\dot{\epsilon}_{ij} = (v_{i,j} + v_{j,i})/2$  for a given velocity field  $v_i$  can be decomposed into a viscoelastic component  $\dot{\epsilon}_{ij}^{\nu e}$  and a rate-independent plastic component  $\dot{\epsilon}_{ij}^p$

$$\dot{\epsilon}_{ij} = \dot{\epsilon}_{ij}^{\nu e} + \dot{\epsilon}_{ij}^p. \quad (1)$$

Note that we will use " , " before a subscript to denote partial derivatives throughout the paper. In what follows, we first derive an expression for  $\dot{\epsilon}_{ij}^{\nu e}$  based on thermodynamic potentials and then for  $\dot{\epsilon}_{ij}^p$  based on a rate-independent dissipation potential using the normality flow rule.

### Viscoelastic formulation

Various models could be used to model the response of viscoelastic liquids (Lemaitre and Chaboche, 1990). In this investigation, we adopt a Maxwell fluid model for its simplicity and yet its accountability in explaining the experimentally observable relaxation of stress (Bair and Winer, 1993). It is assumed that the total viscoelastic strain is the sum of an elastic and anelastic part, so that

$$\epsilon_{ij}^{\nu e} = \epsilon_{ij}^e + \epsilon_{ij}^{an}. \quad (2)$$

The elastic component of the strain is given by

$$\epsilon_{ij}^e = \rho \frac{\partial \psi^*}{\partial \sigma_{ij}} \quad (3)$$

and the anelastic component in a rate form by

$$\dot{\epsilon}_{ij}^{an} = \frac{\partial \varphi^*}{\partial \sigma_{ij}}, \quad (4)$$

where  $\psi^*$  and  $\varphi^*$  are the thermodynamic potential and the dual dissipation potential, respectively. Both potentials are functions of the stress state.

For a linear theory, the same thermodynamic potential can be used as for the isotropic linear elasticity. We thus write

$$\psi^* = \frac{1}{2\rho} \left[ \left( \frac{1+\nu}{E} \right) \text{Tr}(\sigma^2) - \frac{\nu}{E} (\text{Tr}(\sigma))^2 \right], \quad (5)$$

where  $\rho$  is the mass density of the material,  $\nu$  the Poisson's ratio,  $E$  the elastic modulus, and  $\sigma$  the stress tensor. Similarly, the dual dissipation potential  $\varphi^*$  is defined by a positive definite quadratic form which includes two new coefficients  $\tau_1$  and  $\tau_2$  and is given by

$$\varphi^* = \frac{1}{2} \left[ \left( \frac{1+\nu}{E\tau_1} \right) \text{Tr}(\sigma^2) - \frac{\nu}{E\tau_2} (\text{Tr}(\sigma))^2 \right]. \quad (6)$$

The coefficients  $\tau_1$  and  $\tau_2$  are characteristic of the viscosity and they may be determined by shear and uniaxial compression tests. The viscoelastic rate of strain can then be determined by combining Eqs (2)-(6). The result is given by

$$\begin{aligned} \dot{\epsilon}_{ij}^{\nu e} = & \left[ \left( \frac{1+\nu}{E} \right) \dot{\sigma}_{ij} - \frac{\nu}{E} \dot{\sigma}_{kk} \delta_{ij} \right] \\ & + \left[ \left( \frac{1+\nu}{E\tau_1} \right) \sigma_{ij} - \frac{\nu}{E\tau_2} \sigma_{kk} \delta_{ij} \right], \end{aligned} \quad (7)$$

where  $\delta_{ij}$  is the Kronecker delta. The expression in the first bracket is the elastic component. The one in the second bracket takes into account the effects of viscosity which result in a time dependent response of a viscoelastic medium. Hence Eq (7) can be cast into the standard form

$$\dot{\epsilon}_{ij}^{\nu e} = S_{ijkl} \dot{\sigma}_{kl} + R_{ijkl} \sigma_{kl}, \quad (8)$$

where  $S_{ijkl}$  is the elastic compliance tensor and  $R_{ijkl}$  the viscous creeping tensor. Inverting Eq (8), and then expressing the results in terms of Lamé's constants  $\lambda$  and  $\mu$ , we have

$$\dot{\sigma}_{ij} = \left[ 2\mu \dot{\epsilon}_{ij}^{\nu e} + \lambda \delta_{ij} \dot{\epsilon}_{kk}^{\nu e} \right] - \left[ \frac{\sigma_{ij}}{\tau_1} + \frac{\lambda}{2\mu} \left( \frac{1}{\tau_1} - \frac{1}{\tau_2} \right) \delta_{ij} \sigma_{kk} \right], \quad (9)$$

or, in short

$$\dot{\sigma}_{ij} = C_{ijkl}^e \dot{\epsilon}_{kl}^{\nu e} - A_{ijkl} \sigma_{kl}, \quad (10)$$

where the component of the viscoelastic modulus

$$C_{ijkl}^e = \mu(\delta_{ik}\delta_{jl} + \delta_{il}\delta_{jk}) + \lambda(\delta_{ij}\delta_{kl}) \quad (11)$$

and the components of the viscous relaxation tensor

$$A_{ijkl} = \mu'(\delta_{ik}\delta_{jl} + \delta_{il}\delta_{jk}) + \lambda'(\delta_{ij}\delta_{kl}) \quad (12)$$

with

$$\mu = \frac{E}{2(1+\nu)} \quad ; \quad \lambda = \frac{E\nu}{(1+\nu)(1-2\nu)} \quad (13)$$

and

$$\mu' = \frac{1}{2\tau_1} \quad ; \quad \lambda' = \frac{\nu}{1-2\nu} \left[ \frac{1}{\tau_1} - \frac{1}{\tau_2} \right]. \quad (14)$$

It can be seen that the expression in first bracket of Eq (9) is of a form identical to the generalized Hooke's law for an isotropic medium, except that the components are of the viscoelastic rate of deformation tensor instead of being the elastic components of the total deformation rate tensor. The expression in the second bracket accounts for the time-dependent viscous effects such as relaxation and creep that depends on the instantaneous state of stress in the material. The physical interpretation of Eq (9) is as follows: The increment of the stress at any instant of time depends on an instantaneous Hookean response of the viscoelastic strain increment. The instantaneous stress increment includes all rate and time dependent effects, and during the increment, the viscous relaxation and other time dependent behavior of material occurred in the previous stress state is removed.

*Creep and relaxation responses*

The application of Eq (7) to a plane shear test gives

$$\dot{\epsilon}_{12}^{\nu e} = \frac{1+\nu}{E} \dot{\sigma}_{12} + \frac{1+\nu}{E\tau_1} \sigma_{12}. \quad (15)$$

In response to relaxation test  $\dot{\epsilon}_{12}^{\nu e} = 0$ , the integration of Eq (15) leads to

$$\sigma_{12} = \sigma_{12}^* \exp\left(-\frac{t}{\tau_1}\right), \quad (16)$$

where  $\sigma_{12}^*$  is the instantaneous shear stress at time  $t = 0$ . Thus  $\tau_1$  can be physically interpreted as the relaxation

time in a plane shear test and can be determined from Eq (16).

As indicated by Eq (1), the total rate of deformation is the sum of the viscoelastic part and the rate-independent part. The volumetric creep and relaxation behavior of a lubricant under a hydrostatic compression can be studied by examining the following rate equation

$$\dot{\epsilon}_{kk}^{\nu e} = \frac{1-2\nu}{E} \dot{\sigma}_{kk} + \left( \frac{1+\nu}{E\tau_1} - \frac{3\nu}{E\tau_2} \right) \sigma_{kk}. \quad (17)$$

At  $t = 0$ ,

$$\epsilon_{kk}^{\nu e}(0) = \frac{1-2\nu}{E} \sigma_{kk}(0) \quad (18)$$

is the initial condition, which expresses an instantaneous elasticity. Through some algebraic manipulation, the creep function under a step load function  $\sigma_{kk}(t) = 1(t)$  can be found by solving Eq (17), and the result is given by

$$\epsilon_{kk}^{\nu e}(t) = A + [A\delta(t) + B]t \quad (19)$$

where  $A = (1-2\nu)/E$ ,  $B = (1+\nu)/E\tau_1 - 3\nu/E\tau_2$ , and  $\delta(t)$  indicates the Dirac-delta function, which is defined as a function with singularity at  $t = 0$  and  $\delta(t) = 0$  for  $t < 0$ , and  $t > 0$ . The relaxation behavior is described by the relaxation function  $\sigma_{kk}(t)$  which renders the deformation prescribed by  $\epsilon_{kk}^{\nu e}(t) = 1(t)$ . This relaxation function can be found by solving Eq (17) again. The result gives

$$\sigma_{kk}(t) = \frac{1}{A} \exp\left(-\frac{B}{A}t\right) + \frac{1}{B} \delta(t) \quad (20)$$

The quantity  $-A/B$  can be interpreted as the relaxation time, a characteristic of stress relaxation. If the relaxation parameter  $\tau_1$  is known, the parameter  $\tau_2$  can be determined using the above equation.

Note that the creep function and the relaxation function are characteristic only of the viscoelastic properties of the lubricant under test. These two properties are defined in terms of the deviation of pressure from a reference pressure.

**General viscoelastic plastic formulation**

Noting the relation in Eq (1), We rewrite Eq (10) as

$$\dot{\sigma}_{ij} = C_{ijkl}^e (\dot{\epsilon}_{kl} - \dot{\epsilon}_{kl}^p) - A_{ijkl} \sigma_{kl}. \quad (21)$$

This equation represents a general viscoelastic plastic flow relation with a coupled rate-dependent and rate-independent behavior. It is clear that at any instant of time we can calculate the stress rate for a given rate of deformation and stress state, provided that the rate-independent plastic component of the strain rate  $\dot{\epsilon}_{ij}^p$  is known. This can be determined once the form of a suitable rate-independent plastic potential  $\phi(\sigma_{ij})$  is adopted. The derivation can follow that in a rate-independent plasticity theory.



in rate-independent plastic strain that cannot relax with time. Therefore, we can define a viscoelastoplastic modulus  $C_{ijkl}$  given by Eq (32) which provides an apparent stress rate dependent on a Hookean response. This apparent stress rate has to be corrected for effective viscous relaxation and creep, by subtracting the stress rate resulting from the above mentioned effects, dependent on the stress state at the instant the increment of deformation is applied. Thus  $V_{ijkl}$  in Eq (33) is an effective viscoelastic relaxation tensor which applies to the current stress state and provides the effective time dependent effects.

**Symmetry property**

The above formulation is based on the additive decomposition of the rate of deformation tensor as indicated in Eq (1). Such an assumption leads to a quasilinear relationship between  $\dot{\sigma}_{ij}$  and  $\dot{\epsilon}_{ij}$ . Generally speaking, this linearity has been found to be true for thermodynamic systems sufficiently close to equilibrium. Of course the ultimate justification of this property relies on the ability of the representing equations to predict experimental observations. For deformation to be path independent in the small,  $C_{ijkl}$  must be symmetric (Lee, 1993). This symmetry property always exists because both  $C_{ijkl}^e$  and  $C_{ijkl}^I$  are symmetric. To have a symmetric stress-strain response, however, we also require that the coefficient of stress in Eq (31) be symmetric as well. This can be made by imposing a symmetric condition on  $A_{ijkl}^I$ . Thus, we require that

$$\tilde{\phi}_{ab}\tilde{\phi}_{cd}\delta_{ai}\delta_{bj}\delta_{ck}\delta_{dl} = \tilde{\phi}_{ab}\tilde{\phi}_{cd}\delta_{ak}\delta_{bl}\delta_{ci}\delta_{dj}. \quad (38)$$

Substituting  $\tilde{\phi}_{ab}$  and  $\tilde{\phi}_{cd}$  from Eqs (36) and (37), we obtain

$$\left(\frac{\lambda}{2\mu} - \frac{\lambda'}{2\mu'}\right) [\phi_{ii}\delta_{ij}\phi_{kl} - \phi_{ii}\delta_{kl}\phi_{ij}] = 0. \quad (39)$$

Since the terms in the bracket cannot be zero should any deformation occur, we can only require that

$$\left(\frac{\lambda}{2\mu} - \frac{\lambda'}{2\mu'}\right) = 0. \quad (40)$$

Substituting from Eqs (13) and (14), we conclude that either  $\tau_1 = 0$  or  $1/\tau_2 = 0$ .

We recall that  $\tau_1$  represents the characteristic relaxation time for a shear deformation; it cannot vanish because lubricants usually exhibit a marked rate-dependent behavior in shear. Thus the only logical choice is that  $1/\tau_2$  must vanish. As a result of this condition and the discussion on the relaxation constants in a previous section, the complete relaxation behavior of lubricant is described by a single relaxation parameter  $\tau_1$ . Note, however, that we will continue to have different characteristic time for the two deformation modes, namely shear deformation and hydrostatic compression. From the symmetry requirements, we find from Eqs (36) and (37) that

$$\tilde{\phi}_{ij} = \hat{\phi}_{ij}. \quad (41)$$

**Physical interpretation of  $\Gamma$**

Alternatively, we can solve  $\dot{\Lambda}$  by combining Eqs (24), (25) and (26); the result is

$$\dot{\Lambda} = \beta\dot{\phi} \quad (42)$$

where the inverse

$$\frac{1}{\beta} = \frac{\partial\chi}{\partial W^p} \sigma_{ij}\phi_{ij} \quad (43)$$

Since  $\phi(\sigma_{ij})$  is a scalar measure of the effect of the stress tensor on the material, we infer that  $\phi(\sigma_{ij})$  is a flow surface which distinguishes the nonlinear rate-independent viscous behavior (which is termed plastic before) from the rate-dependent one. We can represent this surface by an equivalent stress,  $\sigma_{eq}$ . Correspondingly, there is some equivalent plastic strain, whose increment produces a rate change in the rate-independent plastic strain energy associated with the material. Hence, from Eq (24) it is clear that

$$\sigma_{eq}\dot{\epsilon}_{eq}^p = \sigma_{ij}\beta\dot{\phi}\phi_{ij} \quad (44)$$

Noting that  $\dot{\phi} = \dot{\sigma}_{eq}$ , we write

$$\frac{1}{\beta} = (2\mu_{eq}^p/\sigma_{eq}) \sigma_{ij}\phi_{ij}, \quad (45)$$

where the instantaneous plastic tangential modulus,  $2\mu_{eq}^p \equiv \dot{\sigma}_{eq}/\dot{\epsilon}_{eq}^p$ , represents the slope along the equivalent-stress equivalent-plastic strain curve of a material. This modulus represents the hardening character of the lubricant. Using Eqs (11), (36) and (43), we obtain from Eq (29) the expression for  $\Gamma$ ,

$$\Gamma = \frac{1}{\beta} + 2\mu\phi_{ij}\tilde{\phi}_{ij} \quad (46)$$

Similar to  $\beta$  physically,  $\Gamma$  represents the effect of the material specific hardening response to the instantaneous state of stress in the material.

With the above results and through some manipulations, one can show that coefficients  $C_{ijkl}$  and  $V_{ijkl}$  in Eq (31) reduce to

$$C_{ijkl} = \mu(\delta_{ik}\delta_{jl} + \delta_{il}\delta_{jk}) + \lambda\delta_{ij}\delta_{kl} - \frac{2\mu\tilde{\phi}_{ab}\tilde{\phi}_{cd}\delta_{ai}\delta_{bj}\delta_{ck}\delta_{dl}}{1/\beta^* + \phi_{mn}\tilde{\phi}_{rs}\delta_{mr}\delta_{ns}} \quad (47)$$

and

$$V_{ijkl} = \mu'(\delta_{ik}\delta_{jl} + \delta_{il}\delta_{jk}) + \lambda'\delta_{ij}\delta_{kl} - \frac{2\mu'\tilde{\phi}_{ab}\tilde{\phi}_{cd}\delta_{ai}\delta_{bj}\delta_{ck}\delta_{dl}}{1/\beta^* + \phi_{mn}\tilde{\phi}_{rs}\delta_{mr}\delta_{ns}}, \quad (48)$$

respectively, where  $\beta^* = 2\mu\beta$ .

In the past there has been an inconclusive discussion relating to the validity of Stokes condition, and its outcome on the modeling behavior of Newtonian fluids. It is clear, from the viscoelastic plastic formulation, that there is no need to invoke the Stokes condition in order to deal with the constitutive modeling of lubricants.

**Example for the flow potential  $\phi$**

So far we have proposed a general formulation for the viscoelastic plasticity of lubricants without having discussed a specific form for the rate-independent plastic flow potential. Bowden and Jukes (1972) reported the yield behavior of lubricant and liquid polymers; their results indicated that yielding is pressure dependent. They suggested the use of a modified von Mises criterion to describe such a behavior for polymers. Their criterion, in fact, is termed as the Drucker-Prager criterion (1952). It is often used in soil mechanics, for which soil is usually treated as a medium that cannot support a tension force, a characteristic exhibited by all liquids as well. In our analysis, we have adopted the same criterion, but we write it in an alternative form in terms of a mean pressure  $P$

$$\phi(\sigma_{ij}) = \sqrt{J_2} + \alpha P, \tag{49}$$

where  $J_2$  is the second invariant of the stress deviator tensor  $S_{ij}$ , and  $P$  is positive for compression. For a rigid incompressible plasticity model,  $\alpha$  is bounded by  $\pm\sqrt{3}/2$ . When  $\alpha$  is zero, Eq (49) reduces to the von Mises criterion.

Clearly, the Drucker-Prager criterion provides for a linear increase in the shear yield stress with the mean hydrostatic pressure  $P$ . This type of linear variation of the yield stress with pressure, has been found to be obeyed by amorphous glassy polymers (Bowden,1973). The dimensionless constant of proportionality  $\alpha$  is a material property. Its value has to be determined by fitting experimental results. It can be shown from Eq (49) that

$$\phi_{ij} \equiv \frac{\partial\phi}{\partial\sigma_{ij}} = \frac{1}{2\sqrt{J_2}} S_{ij} - \frac{\alpha}{3} \delta_{ij}. \tag{50}$$

**EQUILIBRIUM REQUIREMENT**

A suitable frame invariant stress rate must be used with the constitutive relation presented in the previous sections. The selection of a frame-indifference stress rate is by no means conclusive. To provide a frame-indifference flow rule we replace the stress rate  $\dot{\sigma}_{ij}$  in Eq (31) by the Jaumann stress rate  $\hat{\sigma}_{ij}$ . The relation between these two stress rates is given by

$$\hat{\sigma}_{ij} = \dot{\sigma}_{ij} + \sigma_{im}\dot{\omega}_{mj} - \sigma_{jm}\dot{\omega}_{im} \tag{51}$$

where  $\dot{\omega}_{ij}$  is the spin tensor and  $\dot{\omega}_{ij} \equiv (v_{i,j} - v_{j,i})/2$ .

Since deformation is considered as a rate problem, the requirements of mechanical equilibrium must be applied not only to the instantaneous state of stress, but also to their rate change. The derivation of stress rate equations of equilibrium can be found elsewhere, e.g., see the work by Lee (1988). The requirement states that

$$\dot{\sigma}_{ij,j} - \sigma_{ki,j}v_{j,k} = 0. \tag{52}$$

This equation gives the complete description for the equilibrium state of the material. It governs the stress field irrespective of the magnitude of deformation, and material structure. Satisfaction of equation (52) not only implies total stress equilibrium, but also assures that, given an equilibrated stress field, equilibrium is maintained in the presence of time dependent loading. Note that the convective rate of change of stress  $\sigma_{ki,j}v_{j,k}$  in Eq (52) vanishes only in the case of homogeneous deformation, and thus  $\dot{\sigma}_{ij,j}$  alone may not represent the material derivative of the total stress equilibrium.

**SHEAR BAND ANALYSIS**

**Velocity field equations**

The method of characteristics has proven to be a fruitful means of representing the shear bands in plastic flow problems. Since the characteristics of the partial differential equation of hyperbolic type may indicate paths upon which discontinuities will propagate, it is logical to assume that these characteristics represent shear bands. This concept has been used by Prandtl, Nadai, and other investigators in studying slip lines in plastically deformed bodies. The approach to be presented here is a standard procedure for shear band analysis, at least in the context of elastoplasticity (Lee, 1989, 1992).

In what follows, we consider a plane-strain deformation in rectangular cartesian coordinates, and the plane normal to the z-axis, so that the independent space variables are x, and y,  $\partial/\partial z$  being a null operator. The non-zero deformation rate and spin components are  $\dot{\epsilon}_{xx}$ ,  $\dot{\epsilon}_{yy}$ ,  $\dot{\epsilon}_{xy}$ , and  $\dot{\omega}_{xy}$ . Thus, in terms of velocity components, the equilibrium equations (52) reduce to

$$\begin{aligned} \dot{\sigma}_{xx,x} + \dot{\sigma}_{xy,y} - \sigma_{xx,x}v_{x,x} - \sigma_{xx,y}v_{y,x} \\ - \sigma_{xy,x}v_{x,y} - \sigma_{xy,y}v_{y,y} = 0 \end{aligned} \tag{53}$$

$$\begin{aligned} \dot{\sigma}_{xy,x} + \dot{\sigma}_{yy,y} - \sigma_{xx,x}v_{x,x} - \sigma_{xy,y}v_{y,x} \\ - \sigma_{yy,x}v_{x,y} - \sigma_{yy,y}v_{y,y} = 0. \end{aligned} \tag{54}$$

The constitutive relationship can be written in a matrix form for plane strain deformation as

$$\begin{Bmatrix} \hat{\sigma}_{xx} \\ \hat{\sigma}_{yy} \\ \hat{\sigma}_{xy} \\ \hat{\sigma}_{zx} \end{Bmatrix} = \begin{bmatrix} b_{11} & b_{12} & b_{13} \\ b_{21} & b_{22} & b_{23} \\ b_{31} & b_{32} & b_{33} \\ b_{41} & b_{42} & b_{43} \end{bmatrix} \begin{Bmatrix} v_{x,x} \\ v_{y,y} \\ (v_{x,y} + v_{y,x}) \end{Bmatrix}$$

$$- \begin{bmatrix} a_{11} & a_{12} & a_{13} & a_{14} \\ a_{21} & a_{22} & a_{23} & a_{24} \\ a_{31} & a_{32} & a_{33} & a_{34} \\ a_{41} & a_{42} & a_{43} & a_{44} \end{bmatrix} \begin{Bmatrix} \sigma_{xx} \\ \sigma_{yy} \\ \sigma_{xy} \\ \sigma_{zz} \end{Bmatrix} \quad (55)$$

Denoting the shear stress by  $T$ , i.e.,  $T = \sigma_{xy}$  and the first normal stress difference by  $2N$ , i.e.,  $N = (\sigma_{xx} - \sigma_{yy})/2$ , and then combining the equilibrium equation (53), the constitutive equation (55) in terms of the Cauchy stress rate by using Eq (51), we obtain

$$\begin{aligned} & b_{11}v_{x,xx} + [b_{13} + b_{31} + T]v_{x,xy} + [b_{33} - N]v_{x,yy} \\ & + [b_{13} - T]v_{y,xx} + [b_{12} + b_{33} + N]v_{y,xy} + b_{32}v_{y,yy} \\ & \quad + [b_{11,x} + b_{31,y} - \sigma_{xx,x}]v_{x,x} \\ & \quad + [b_{12,x} + b_{32,y} - \sigma_{xy,y}]v_{y,y} \\ & + [b_{13,x} + b_{33,y} - (\sigma_{xx,y} - \sigma_{xy,x})/2](v_{x,y} + v_{y,x}) \\ & \quad - [a_{11,x} + a_{31,y}]\sigma_{xx} - [a_{12,x} + a_{32,y}]\sigma_{yy} \\ & \quad - [a_{13,x} + a_{33,y}]\sigma_{xy} - [a_{14,x} + a_{34,y}]\sigma_{zz} \\ & - a_{11}\sigma_{xx,x} - a_{31}\sigma_{xx,y} - a_{12}\sigma_{yy,x} - a_{32}\sigma_{yy,y} \\ & - a_{13}\sigma_{xy,x} - a_{33}\sigma_{xy,y} - a_{14}\sigma_{zz,x} - a_{34}\sigma_{zz,y} \\ & = 0. \end{aligned} \quad (56)$$

Similarly, the combination of Eqs (51), (54) and (55) gives

$$\begin{aligned} & b_{31}v_{x,xx} + [b_{33} + b_{21} - N]v_{x,xy} + [b_{23} - T]v_{x,yy} \\ & + [b_{33} + N]v_{y,xx} + [b_{32} + b_{23} + T]v_{y,xy} + b_{22}v_{y,yy} \\ & \quad + [b_{31,x} + b_{21,y} - \sigma_{xy,y}]v_{x,x} \\ & \quad + [b_{32,x} + b_{22,y} - \sigma_{yy,y}]v_{x,y} \\ & + [b_{33,x} + b_{23,y} - \frac{1}{2}(\sigma_{yy,x} - \sigma_{xy,y})](v_{x,y} + v_{y,x}) \\ & \quad - [a_{31,x} + a_{21,y}]\sigma_{xx} - [a_{32,x} + a_{22,y}]\sigma_{yy} \\ & \quad - [a_{33,x} + a_{23,y}]\sigma_{xy} - [a_{34,x} + a_{24,y}]\sigma_{zz} \\ & - a_{31}\sigma_{xx,x} - a_{21}\sigma_{xx,y} - a_{32}\sigma_{yy,x} - a_{22}\sigma_{yy,y} \\ & - a_{33}\sigma_{xy,x} - a_{23}\sigma_{xy,y} - a_{34}\sigma_{zz,x} - a_{24}\sigma_{zz,y} \\ & = 0. \end{aligned} \quad (57)$$

Equations (56) and (57) are the velocity equilibrium equations of the deformation, and govern the instantaneous spatial dependence of the velocity field. Thereby they provide a quasi-linear model for the entire deformation process.

### Characteristic analysis

We now examine the conditions under which the velocity equilibrium equations (56) and (57) may be integrated on characteristic surfaces.

Defining new variables  $u_i$ , such that

$$u_1 = v_{x,x}, \quad u_2 = v_{x,y}, \quad u_3 = v_{y,x}, \quad u_4 = v_{y,y}. \quad (58)$$

Equations (56) and (57) may now be expressed in terms of the new variables  $u_i$ , and the result can be cast into a canonical form

$$P_{ij} \frac{\partial u_j}{\partial x} + Q_{ij} \frac{\partial u_j}{\partial y} = R_i, \quad (i, j = 1, 2, 3, 4). \quad (59)$$

We may posit that there are linear combinations of Eq (59) such that the result is a common directional derivative of  $u_i$ . That is, the expression

$$\nu_i \left[ P_{ij} \frac{\partial u_j}{\partial x} + Q_{ij} \frac{\partial u_j}{\partial y} \right] = \nu_i R_i. \quad (60)$$

is *directional*, where  $\nu_i$  is the direction of the directional derivative. This derivative is along a set of curves  $\vartheta(x, y, u_i) = \text{constant}$ , so that the directions are normal to the gradient of  $\vartheta$ . Thus we write

$$\nu_i P_{ij} \vartheta_{,x} + \nu_i Q_{ij} \vartheta_{,y} = 0. \quad (61)$$

Denoting the slope of the characteristic curves by  $\Delta$ , thus

$$\Delta = - \frac{\vartheta_{,x}}{\vartheta_{,y}}, \quad (62)$$

and Eq (61) becomes

$$[Q_{ij} - \Delta P_{ij}] \nu_i = 0. \quad (63)$$

For  $\nu_i$  to have a non-trivial solution, the determinant of the coefficients of  $\nu_i$  must vanish. Hence,

$$\det|Q_{ij} - \Delta P_{ij}| = 0. \quad (64)$$

Noting that coefficients  $a_{ij}$ , and  $b_{ij}$  are symmetric we deduce from Eq (64) a quartic equation in  $\Delta$  and the result is

$$\begin{aligned} & \Delta^4 [b_{13}(b_{13} - T) - b_{11}(b_{33} + N)] \\ & \quad + \Delta^3 [2(b_{11}b_{23} - b_{12}b_{13}) \\ & \quad + (b_{11} + b_{12} + 2b_{33})T + 2b_{13}N] \\ & + \Delta^2 [b_{12}(b_{12} - 2b_{33}) - b_{11}b_{22} - 2b_{13}b_{23} - 3(b_{13} + b_{23})T] \\ & \quad + \Delta [2(b_{13}b_{22} - b_{12}b_{23}) \\ & \quad + (b_{22} + b_{12} + 2b_{33})T - 2b_{23}N] \\ & + [b_{23}(b_{32} - T) - b_{22}(b_{33} - N)] \\ & = 0. \end{aligned} \quad (65)$$

Denoting the principal components of the quantities  $\sigma_{ij}$ ,  $\phi_{ij}$ , and  $\tilde{\phi}_{ij}$  by a single subscript, i.e.,  $\sigma_1, \dots, \phi_1, \dots$ ,

etc., we obtain the coefficients  $b_{ij}$  in terms of principal coordinates; the result gives

$$\begin{aligned} b_{11} &= \frac{2\mu}{(1-2\nu)\Gamma^*} \left[ (1-\nu)\Gamma^* - (1-2\nu)\bar{\phi}_1^2 \right] \\ b_{22} &= \frac{2\mu}{(1-2\nu)\Gamma^*} \left[ (1-\nu)\Gamma^* - (1-2\nu)\bar{\phi}_2^2 \right] \\ b_{33} &= \mu \\ b_{12} &= \frac{2\mu}{(1-2\nu)\Gamma^*} \left[ \nu\Gamma^* - (1-2\nu)\bar{\phi}_1\bar{\phi}_2 \right] \\ b_{41} &= \frac{2\mu}{(1-2\nu)\Gamma^*} \left[ \nu\Gamma^* - (1-2\nu)\bar{\phi}_3\bar{\phi}_1 \right] \\ b_{42} &= \frac{2\mu}{(1-2\nu)\Gamma^*} \left[ \nu\Gamma^* - (1-2\nu)\bar{\phi}_3\bar{\phi}_2 \right] \\ b_{13} &= 0 \\ b_{23} &= 0 \\ b_{43} &= 0 \end{aligned} \quad (66)$$

where

$$\Gamma^* = \frac{1}{\beta^*} + \phi_1\bar{\phi}_1 + \phi_2\bar{\phi}_2 + \phi_3\bar{\phi}_3. \quad (67)$$

Expressing in terms of principal quantities and replacing  $N$  by  $\bar{N}$  which is defined as  $\bar{N} = N/\mu$ , we recast Eq (65) in the form

$$a(1+\bar{N})\Delta^4 + 2b\Delta^2 + c(1-\bar{N}) = 0 \quad (68)$$

with

$$\begin{aligned} a &= (1-\nu)\Gamma^* - (1-2\nu)\bar{\phi}_1^2 \\ b &= (1-\nu)\Gamma^* + \bar{\phi}_1\bar{\phi}_2 - (1-\nu)(\bar{\phi}_1^2 + \bar{\phi}_2^2) \\ c &= (1-\nu)\Gamma^* - (1-2\nu)\bar{\phi}_2^2. \end{aligned} \quad (69)$$

For  $\bar{N} < 1$ , the necessary and sufficient condition for the onset of shear banding is that

$$(i) \quad |\bar{N}| = [(ac - b^2)/ac]^{1/2}$$

and

$$(ii) \quad b < 0 \quad (70)$$

hold simultaneously. The slopes, i.e., the characteristic directions of shear bands, can then be found by solving Eq (68). The result gives

$$\Delta = \pm \left[ \frac{-b}{a(1+\bar{N})} \right]^{1/2}. \quad (71)$$

## RESULTS AND DISCUSSION

### Critical values of $\bar{N}$ , $\Gamma^*$ , and $2\mu_{eq}^p$

Inserting Eq (69) into Eq (70) leads to

$$|\bar{N}| = \left\{ (\bar{\phi}_1 - \bar{\phi}_2)^2 \left[ \frac{\Gamma^*}{1-\nu} - (\bar{\phi}_1 + \bar{\phi}_2)^2 + \frac{2}{1-\nu}\bar{\phi}_1\bar{\phi}_2 \right] \right\}^{1/2}.$$

$$\left\{ \left[ \Gamma^{*2} - \frac{1-2\nu}{1-\nu}\Gamma^* (\bar{\phi}_1^2 + \bar{\phi}_2^2) + \frac{(1-2\nu)^2}{(1-\nu)^2}\bar{\phi}_1^2\bar{\phi}_2^2 \right] \right\}^{1/2}. \quad (72)$$

This gives the critical value of  $\bar{N}$  at which shear banding becomes possible. However, one should note that this condition alone is not sufficient. The inequality represented by the second condition in Eq (70) must also hold for shear bands to occur. Alternatively, this condition can be checked by calculating  $\Delta$  directly because coefficient  $a$  is always positive for a nonzero stress state, and the values of  $\Delta$  are real if  $b < 0$ .

For a given value of  $\bar{N}$ , the corresponding critical value of  $\Gamma^*$  can be found by solving Eq (72). The result gives

$$\begin{aligned} \Gamma_{cr}^* &= \frac{1}{2} \left[ \frac{1-2\nu}{1-\nu} (\bar{\phi}_1^2 + \bar{\phi}_2^2) + \frac{(\bar{\phi}_1 - \bar{\phi}_2)^2}{(1-\nu)\bar{N}^2} \right] \\ &\pm \frac{1}{2} \left\{ \left[ \frac{1-2\nu}{1-\nu} (\bar{\phi}_1^2 + \bar{\phi}_2^2) + \frac{(\bar{\phi}_1 - \bar{\phi}_2)^2}{(1-\nu)\bar{N}^2} \right]^2 \right. \\ &\quad \left. - 4 \left[ \left( \frac{1-2\nu}{1-\nu} \right)^2 \bar{\phi}_1^2\bar{\phi}_2^2 \right. \right. \\ &\quad \left. \left. + \frac{(\bar{\phi}_1 - \bar{\phi}_2)^2}{\bar{N}^2} \left( (\bar{\phi}_1 + \bar{\phi}_2)^2 - \frac{2\bar{\phi}_1\bar{\phi}_2}{(1-\nu)} \right) \right] \right\}^{1/2}. \end{aligned} \quad (73)$$

Corresponding to  $\Gamma_{cr}^*$ , we can determine the critical value of  $\beta_{cr}^*$  from Eqs (46) for an instantaneous stress state. Corresponding to  $\beta_{cr}^*$ , there exists a critical plastic tangential modulus of the lubricant,  $\mu_{eq}^p|_{cr}$ , below which shear bands may not occur. Since  $\beta_{cr}^*$  is also a function of stresses which, in turn, will determine the inequality in Eq (70). Thus, the critical plastic tangential modulus for the onset of shear banding is not a constant. It is stress and thus problem dependent.

The critical plastic tangential modulus can be obtained by eliminating  $\beta^*$  from Eqs (45) and (67). The result gives

$$2\mu_{eq}^p|_{cr} = 2\mu\sigma_{eq} \left[ \frac{\Gamma_{cr}^* - (\phi_1\bar{\phi}_1 + \phi_2\bar{\phi}_2 + \phi_3\bar{\phi}_3)}{\sigma_1\phi_1 + \sigma_2\phi_2 + \sigma_3\phi_3} \right]. \quad (74)$$

At this juncture, an additional comment about  $\beta$  is necessary. It is clear from Eq (30) that for a purely viscoelastic deformation  $\beta$  tends to zero. If  $\beta$  becomes  $\infty$ , on the other hand, the deformation has no apparent hardening, i.e.,  $2\mu_{eq}^p$  becomes zero in Eq (45). There is a possibility that shear banding may occur at a softening stage, i.e., when  $\beta < 0$ . In other words, shear banding may occur at any value of  $\beta$ . Thus, to predict the onset of shear banding, it is necessary to include the evolution of the loading

Table 1: Effect of  $\alpha$  on shear band angles  $\theta_1$  and  $\theta_2$  measured from the flow direction.

$\alpha$	$\theta_1$	$\theta_2$
-0.080	18.08	103.94
-0.090	18.32	103.69
-0.100	18.57	103.45
-0.110	18.81	103.21
-0.118	19.00	102.99
-0.120	19.05	102.97
-0.130	19.29	102.73
-0.140	19.52	102.50
-0.150	19.75	102.27
-0.160	19.98	102.04

path as a part of the analysis because plastic deformation is path dependent, and the analysis would require numerical simulation. This is beyond the scope of the current paper, and will be addressed in a later paper.

**Orientation of shear bands**

The characteristic directions of shear bands, in general, are given by Eq (71) from which the orientation of shear bands  $\Theta$  with respect to the directions of principal stresses can be found by

$$\Theta = \pm \tan^{-1} \Delta. \tag{75}$$

In order to compare the analytic predictions with the experimental results provided by Bair et al. (1993), an appropriate coordinate transformation must be applied to obtain the shear band angles,  $\theta_1$  and  $\theta_2$ , which are measured from the solid surface, i.e., the flow direction, in their high pressure flow visualization cell.

It was mentioned earlier that the value for  $\alpha$  used in the Drucker-Prager plastic dissipation potential is a material property, and needs to be determined from experiments. To determine  $\alpha$  without knowing the precise loading history, we assume that  $1/\beta = 0$  because  $\beta_{cr}$  is in the order of  $(\sigma_{2g}/\mu)^2$  (Lee, 1989). We also note that for most engineering materials, if not for all,  $\bar{N}$  is relative small when compared with unity, thus  $1 + \bar{N} \approx 1$ . The above two assumptions together with Eqs (50), (67), (69), and (71) are used to determine the orientation of shear bands for different values of  $\alpha$ . Using 0.4 for  $\nu$  and 0.5 for the transverse stress ratio  $k$  which is defined as  $\sigma_3/(\sigma_1 + \sigma_2)$ , we tabulate the results in Table 1. It is to be expected that  $\alpha$  would have an effect on the orientation of shear bands. However, as shown in Table 1 the effect is modest; for the range of  $\alpha$  which has physical significance and which covers a class of polymers (Bowden, 1973), the effect of  $\alpha$  is less observable. Note that  $\alpha$  is negative in the sense that the shear component of  $\phi$  increases as the pressure increases when  $\phi$  is taken as the loading function and the flow rule is associative. This is consistent

with experimental observations that shear strength of a lubricant increases as pressure increases. These values of  $\alpha$  lie within the range of values predicted by Drucker and Prager (1952). For polyethyl ether 5P4E, Bair et al. (1993) reported shear band angles of  $\theta_1 = 19^\circ$  and  $\theta_2 = 103^\circ$ . As shown in Table 1, their result is matched by the case for which  $\alpha = -0.118$ . Therefore, we use this value for all subsequent calculations. It should be noted, however, that more experimental data may be required

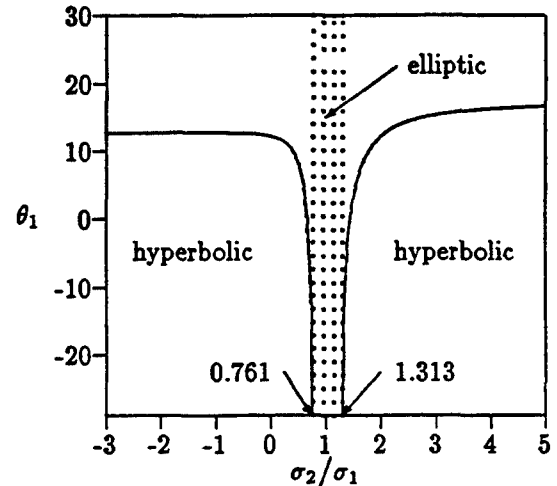


FIG. 2-(a)

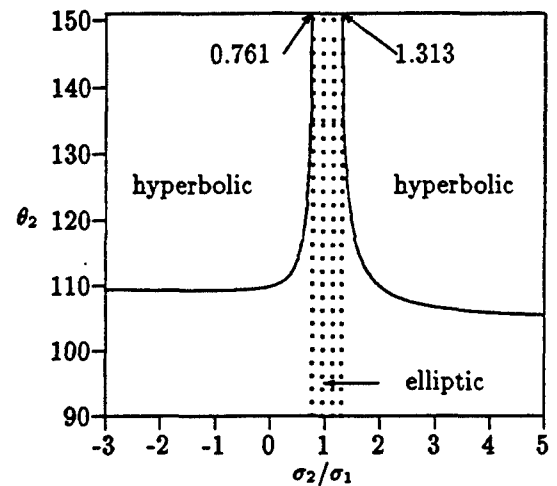


FIG. 2-(b)

FIG. 2 Orientation of shear bands at  $\nu = k = 0.4$ .

to corroborate the value of  $\alpha$ .

Figure 2 shows shear band angle  $\theta_1$  as a function of the ratio of two in-plane principal stresses,  $\sigma_2/\sigma_1$ , which is an invariant. This result is plotted for Poisson's ratio  $\nu=0.4$  and for the transverse stress ratio  $k = 0.4$ . When the ratio  $\sigma_2/\sigma_1$  takes on values such that it is in between 0.761 and 1.313 as shown by the dotted area, the field equations are elliptic and hence no shear bands will occur.

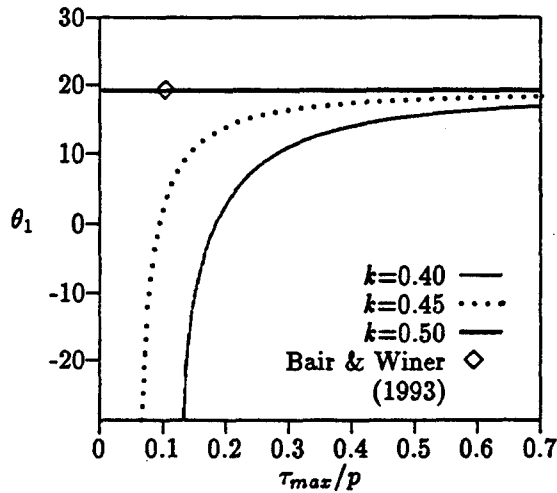


FIG. 3-(a)

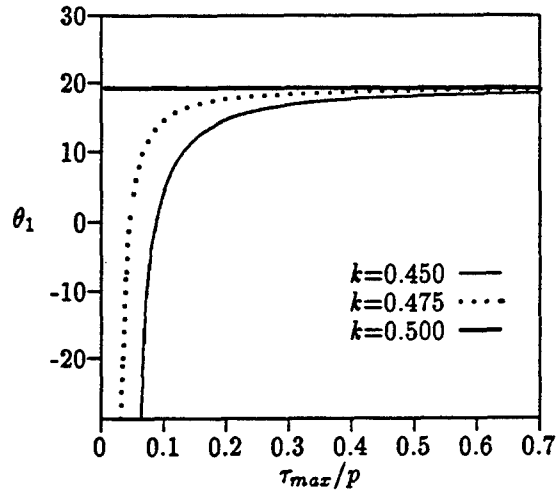


FIG. 4-(a)

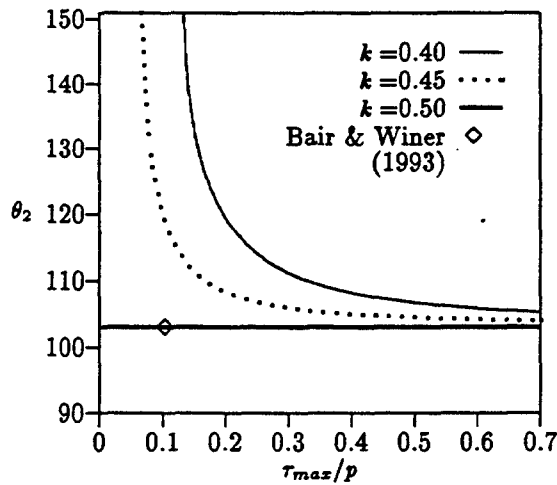


FIG. 3-(b)

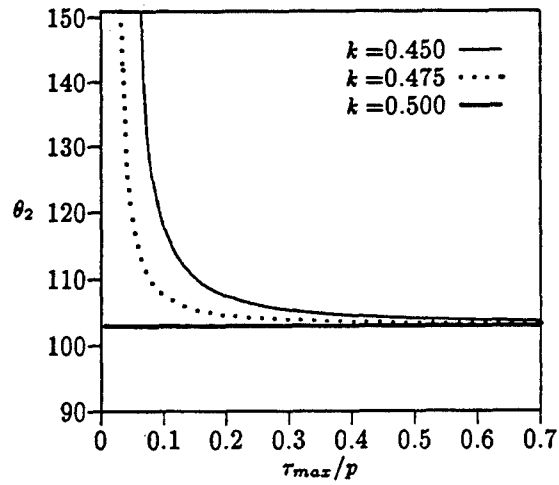


FIG. 4-(b)

FIG. 3 Orientation of shear bands at  $\nu = 0.4$ .

FIG. 4 Orientation of shear bands at  $\nu = 0.45$ .

In general, shear bands are unlikely to occur when the loading state is dominated by its hydrostatic component. Outside the shaded region, i.e., either  $\sigma_2/\sigma_1 < 0.761$  or  $\sigma_2/\sigma_1 > 1.313$ , the field equations become hyperbolic and thus line or characteristic solutions exist and shear banding becomes possible. This result is repeated in Fig. 3 for a further comparison with the other two cases which have different values of  $k$ .

For a liquid lubricant, the loading state excludes the possibility of hydrostatic tension, thus we present in the following the study of shear banding for  $\sigma_2/\sigma_1 \geq 1$  that corresponds to  $\tau_{max}/P \geq 0$ , where  $\tau_{max} = (\sigma_1 - \sigma_2)/2$  is the maximum shear stress and is non-negative. Note that  $\tau_{max}/P$  is also an invariant and is non-negative. Figures 3 to 5 show the orientation of shear bands under different loading states for which the Poisson's ratio  $\nu$  are 0.4, 0.45, and 0.499, respectively. For each case, the results are shown for different values of  $k$  which is bounded by  $\nu$  and 0.5 in a plane strain deformation. The results are shown

as a function of  $\tau_{max}/P$ . As an example, by comparing the data for  $k = 0.45$  between Fig. 3 and Fig. 4, we find little effect of  $\nu$  on the changing orientation of shear bands, at least for the scale shown. By examining the results at a specific value of  $\tau_{max}/P$ , we in fact know that there is a slight increase in  $\theta_1$  and a slight decrease in  $\theta_2$  as  $\nu$  is increased. For  $\tau_{max}/P = 0.105$ , at which the shear band angles were measured by Bair and Winer (1993), and with  $\nu = 0.4$ , it can be observed from Fig. 3 that shear banding is not possible at  $k = 0.4$ , whereas shear bands occur at  $\theta_1 = 19^\circ$  and  $\theta_2 = 103^\circ$  for  $k = 0.5$ . The effect of increasing transverse stress ratio on the orientation of shear bands follows the same trend as that of  $\nu$ ; however, the changes in orientation are far more pronounced. This observation of the effects of Poisson's ratio and the transverse stress ratio on shear banding is consistent with that reported by Lee (1989) in the context of elastoplasticity. The magnitude of  $k$ , in general, varies during the course of deformation. As the deformation becomes more and more incompressible in nature, the

magnitude of  $k$  tends to its limit at 0.5. For a nearly incompressible medium, the inclination of the shear bands appears to be independent of the pressure. This can be seen from Fig. 5, and the result is consistent with the observation made by Bair et al. (1993). From Figs 3 to 5, in addition, it can be seen that the angle of shear bands appears to reach a limiting value as the deformation tends towards an increasingly incompressible behavior. To be more specific, this angle is between  $19^\circ$  and  $19.25^\circ$  for  $\theta_1$  and between  $102.77^\circ$  and  $103^\circ$  for  $\theta_2$ , depending on the magnitude of the Poisson's ratio  $\nu$ .

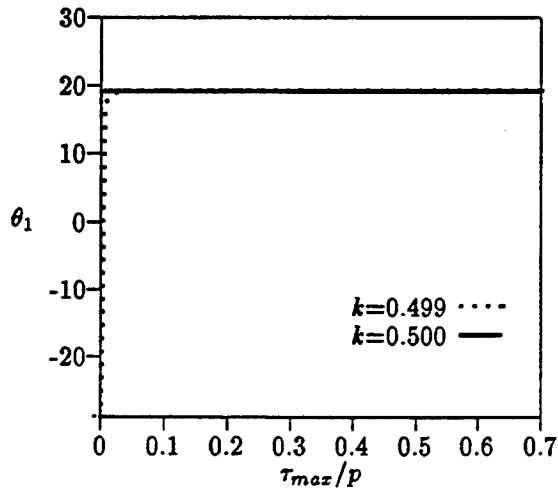


FIG. 5-(a)

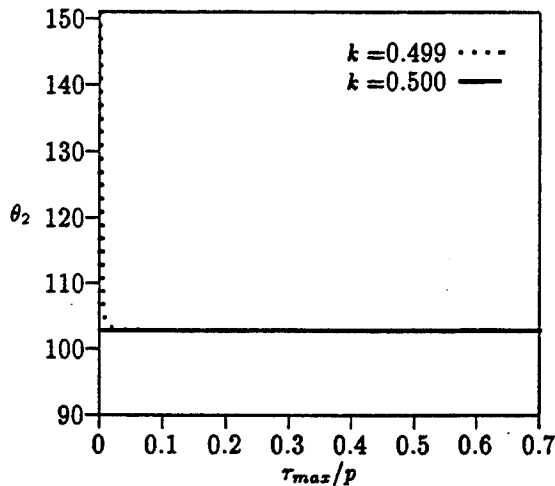


FIG. 5-(b)

FIG.5 Orientation of shear bands at  $\nu = 0.499$ .

Another observation is that with an increasing transverse stress ratio, i.e., as the deformation becomes increasingly incompressible in nature, the regime of ellipticity or the range of stress ratio for which the field equations are elliptic becomes smaller. Eventually at the stress ratio of unity, a hydrostatic state of stress results, and no shear bands can be observed.

## CONCLUDING REMARKS

We give in this paper a constitutive model for viscous materials which have both rate-dependent and rate-independent deformation behavior under a static condition. Based on this model, the analysis also focuses on identifying conditions which, if achieved in a deformation, would produce a change of type in the controlling field equations. The underlying hypothesis is that shear bands will appear when the character of the field equations changes from elliptic to hyperbolic. The results are qualitatively in accord with experimental observations. This approach to shear banding problem is by now standard and is applicable to both solid and liquid media, at least within the framework of the particular decomposition hypothesis proposed in this study. It should be noted that there is by no means unanimity on the proper decomposition of viscoelastic and rate-independent strain or of the proper relation between stress and strain rates. Different relation would give results that may be different in some respects. In addition, since the evolution of the stress path is unknown in advance, one should note that the figures in the last section can only be used qualitatively without solving an actual deformation problem. Thus one should also note that all parts of the diagrams may not be actually accessible. It is not known whether the increased and decreased angles for bands within a very narrow window of stress ratios would be predicted for any realizable deformation history. Nevertheless, the experimental data on the fully developed shear bands does give credence to the theory in a qualitative sense. Thus the next focus of research should be a numerical implementation of the model in order to bring out the full features of the theory.

## ACKNOWLEDGEMENT

The authors would like to acknowledge the support of a Grant from the Office of the Naval Research, tribology program.

## REFERENCES

- Bair S, Qureshi F, and Winer WO, Observation of Shear Localization in a liquid Lubricant under Pressure. *ASME Journal of Tribology*, 115, 3, 507-514, 1993.
- Bair S and Winer WO, The High Pressure High Shear Stress Rheology of Liquid Lubricants. *ASME Journal of Tribology*, 114, 1, 1-13, 1992.
- Bair S and Winer WO, A Rheological Basis for Concentrated Contact Friction. Proceedings of 1993 Leeds-Lyon Symposium on Tribology.
- Bowden PB, The Yield Behavior of Glassy Polymers. in *The Physics of Glassy Polymers*. (ed: R. N. Haward), Chapter 5, Wiley, New York, 1973.
- Bowden PB and Jukes JA, Plastic Flow of Isotropic Polymers. *J Material Science*, 7, 52-63, 1972.
- Drucker DC, Stress-Strain-Time Relations and Irreversible Thermodynamics. in *Second-Order Effects in Elasticity, Plasticity and Fluid Dynamics*, M Reiner and D Abir (ed), The Macmillan Co., New York, 1964, 331-351.

- Drucker DC and Prager W, Soil Mechanics and Plastic Analysis or Limit Design. *Quart Appl Math* 10, 2, 157-165, 1952.
- Lemaitre J and Chaboche J-L, *Mechanics of Solid Materials*. Cambridge UP, Cambridge, UK, 1990.
- Lee YK, A Finite Elastoplastic flow theory for Porous Media. *Int J Plasticity*, 4, 301-316, 1988.
- Lee YK, Conditions for Shear Banding and Material Instability in Finite Elastoplasticity Deformation. *Int J Plasticity*, 5, 197-226, 1989.
- Lee YK, Shear Banding and Material Instability in Finitely Deformed Compressible Materials: An Example in Thin Sheet. *Int J Plasticity*, 8, 543-565, 1992.
- Lee YK, A Unified Framework for Compressible Plasticity. Fourth International Symposium on Plasticity and Its Applications, Baltimore, MD, July 19-23, 1993; *Int J Plasticity*, to appear.
- Prager W, Recent Developments in the Mathematical Theory of Plasticity. *J Appl Phys*, 20, 3, 235-241, 1949.